UNIVERSITAT POLITÈCNICA DE VALÈNCIA

School of Aerospace Engineering and Industrial Design

Numerical study of the effect of decreasing the operational pressure on NASA-R37 axial compressor

End of Degree Project

Bachelor's Degree in Aerospace Engineering

AUTHOR: Ariño Monsec, Iñigo

Tutor: Navarro García, Roberto

ACADEMIC YEAR: 2023/2024

Universitat Politècnica de València

Escuela Técnica Superior de Ingeniería Aeroespacial y Diseño Industrial

Aerospace Engineering Bacherlor's Degree

Final degree project

Numerical study of the effect of decreasing the operational pressure on NASA-R37 axial compressor

Author: Íñigo Ariño Monsec
Tutor: Roberto Navarro García

July 4^{st} 2024

Abstract

This document details the study of the decrease in the operational pressure using NASA's ROTOR-37 model, a 3D axial compressor with a detailed geometry. Computational Fluid Dynamics (CFD) simulations on the ROTOR-37 model are used to study the transition in operational pressure, from 100 kPa to 4 kPa. Four cases are studied, 100 kPa, 40 kPa, 10 kPa and 4 kPa, to ensure a smooth transition and study the effect of the operational pressure decrease among certain values. The numerical models and convergence methods used are described for all the cases. The different patterns, effects and differences that appear in the distinct cases are compared as the operating pressure in the compressor decreases, while maintaining the corrected mass flow rate constant in all the cases. The objective is to analyze the changes in performance that an axial compressor would experience under low operational pressure environments, which would be the case if such compressor were used for Hyperloop transportation systems. The findings offer valuable insights on the low pressure behavior for axial compressors. The presence of laminar boundary layers for low pressures of operation produces lower performances in the compressor. Therefore, the compressor requires to be optimized for low pressures uses.

KEYWORDS: CFD; axial compressor; 3D; operating pressure; ROTOR 37; Hyperloop; pressure decrease;

Resumen

Este documento detalla el estudio de la disminución de la presión de operación utilizando el modelo ROTOR-37 de la NASA, un compresor axial 3D con geometría detallada. Se utilizan simulaciones de Dinámica de Fluidos Computacional (CFD) para estudiar la transición en la presión de operación, desde 100 kPa hasta 4 kPa. Se analizan cuatro casos: 100 kPa, 40 kPa, 10 kPa y 4 kPa, para asegurar una transición suave y estudiar el efecto de la disminución de presión de operación. Se describen los modelos numéricos y métodos de convergencia utilizados para todos los casos. Se comparan los diferentes patrones, efectos y diferencias que aparecen a medida que disminuye la presión de operación en el compresor, manteniendo constante el flujo másico corregido en todos los casos. El objetivo es analizar los cambios en el rendimiento que experimentaría un compresor axial en entornos de baja presión de operación, como sería el caso si se usara dicho compresor en sistemas de transporte Hyperloop. Los hallazgos ofrecen valiosos conocimientos sobre el comportamiento de compresores axiales a baja presión. La presencia de capas límite laminares para bajas presiones de funcionamiento produce menores rendimientos en el compresor. Por lo tanto, el compresor debe optimizarse para su uso en bajas presiones.

PALABRAS CLAVE: CFD; compresor axial; 3D; presión de operación; ROTOR 37; Hyperloop; disminución de presión;

Resum

Aquest document detalla l'estudi de la disminució de la pressió d'operació utilitzant el model ROTOR-37 de la NASA, un compressor axial 3D amb geometria detallada. S'utilitzen simulacions de Dinàmica de Fluids Computacional (CFD) per a estudiar la transició en la pressió d'operació, des de 100 kPa fins a 4 kPa. S'analitzen quatre casos: 100 kPa, 40 kPa, 10 kPa i 4 kPa, per a assegurar una transició suau i estudiar l'efecte de la disminució de la pressió d'operació. Es descriuen els models numèrics i mètodes de convergència utilitzats per a tots els casos. Es comparen els diferents patrons, efectes i diferències que apareixen a mesura que disminueix la pressió d'operació en el compressor, mantenint constant el flux màssic corregit en tots els casos. L'objectiu és analitzar el canvi en el rendiment que experimentaria un compressor axial en entorns de baixa pressió d'operació, com seria el cas si s'utilitzara aquest compressor en sistemes de transport Hyperloop. Les troballes ofereixen valuosos coneixements sobre el comportament de compressors axials a baixa pressió. La presència de capes límit laminars per a baixes pressions de funcionament produïx menors rendiments en el compressor. Per tant, el compressor ha d'optimitzar-se per al seu ús en baixes pressions.

PARAULES CLAU: CFD; compressor axial; 3D; pressió d'operació; ROTOR 37; Hyperloop; disminució de pressió;

Nomenclature

The next list describes several symbols that will be later used within the body of the document:

Acronyms

BR Bypass Ratio

CFD Computer Fluid Dynamics

KL Kantrowitz Limit

LE Leading Edge

MCA Multiple Circular Arc

PhD Doctor of Philosophy

pkm Passenger per Kilometer

$RANS$ Reynolds-Averaged Navier Stokes

TE Trailing Edge

Subscripts

in referred to the inlet

out referred to the outlet

Symbols

α Angle of Incidence

β Flow angle

η Rotor efficiency

γ Ratio of specific heats

λ Stagger angle

μ Dynamic viscosity

π_c Pressure ratio of the compressor

τ_w Wall shear stress

c Airfoil mean chord

C_f Skin friction coefficient

C_p Pressure coefficient

P *or* P_t Total Pressure

P_{op} Operational Pressure

P_{ref} Reference Pressure

P_s Static Pressure

R Gas constant for air

Re_c Reynolds Number referred to the mean chord

T *or* T_t Total Temperature

T_{ref} Reference Temperature

T_s Static Temperature

U Air Velocity

Acknowledgments

The development of this project wouldn't have been feasible without the guidance and tutoring of Roberto Navarro and Borja Pallas. I feel really grateful to have the opportunity to work next to them and I'm pleased with all the insight that they have bring me.

A special mention to my parents, Cristina and Toño who have constantly support and guide me along this four years on my studies, and also to my girlfriend Alicia who has helped me daily with my issues.

Overall, thanks to all the supportive and resilient friends, classmates, professors... who have contributed on my education.

All the achievement and projects wouldn't have been possible without the involvement and encouragement of this people. Therefore I demonstrate my gratitude for all of them, and wish the best in their future goals.

Contents

List of Figures

List of Tables

1 Introduction

1.1 Motivation

Climate change poses one of the most serious challenges that humanity is facing. The inherent nature of the human race to keep pushing our limits and developing new technology often collide with the preservation of our planet. The massive quantities of pollution generated by human activities are affecting globally the composition of our atmosphere and therefore threatening the natural equilibrium of life in Earth. CO_2 arises as on of the most important pollutants of the air, it's greenhouse effect heats up the Earth, altering natural habitats and ceasing the life of some of the species. This greenhouse gas is produced daily in our modern life, and has become a priority to reduce it, searching for greener technologies through new developments.

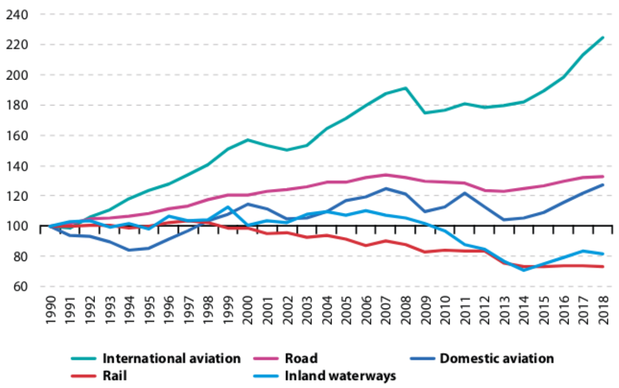

Figure 1.1.1: Energy consumption histogram [1]

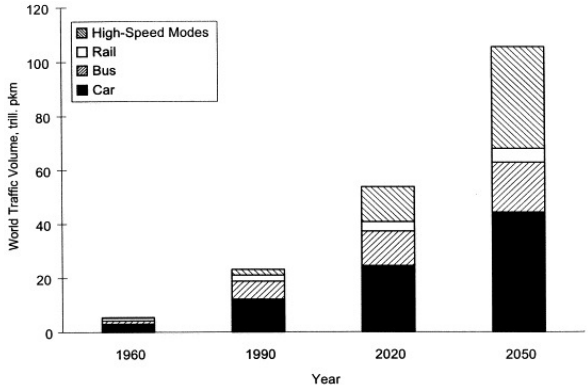

Figure 1.1.2: Forecast of transport pkm [2]

30.5% of the EU production of CO_2 is emitted by the transport industry [1], which supposes around 200 millions of tones of CO_2 [3]. Due to the big carbon footprint left by this sector, important efforts have been done to implement new technologies which reduce emissions on the transport modes. Some means such as the rail sector have been able to reduce their energy consumption and therefore their pollutant emissions, whereas others such as the international and domestic aviation show a devastating upward trend, Figure 1.1.1.

This upward tendency on the aviation sector is related with the increasing overall demand on transportation, and specially of high-speed modes. High-speed modes of transport will increase up to 40% of the world market share by 2050 as forecasted in Figure 1.1.2, almost becoming one of the most used means. This upcoming scenario predicts an exponential increase in pollution, arising the need for a sustainable and fast mean of transport able to support the future demand. A mean capable to compete with the volume, speed and price of planes. Therefore, high speed trains could become a great and green alternative to aviation due to new technological advancements which provide improved speeds and lower consumption.

1.2 Background

The implementation of high-speed rail systems started in Japan in 1964, between the cities of Osaka and Tokyo as a solution to the need of a mean of transport capable of carrying a great volume of passengers in short times [4]. The evolution of this mean of transport has been characterized by the fierce competence with the airplane industry. At the current state of the art of this technology the lower speed of the trains but higher comfort makes it a fair competitor against airplane transport up to 1,000 km (620 miles) travels [4]. Nevertheless, the great investment on infrastructures needed for high-speed trains outweighs the low CO_2 emissions per pkm and other advantages of this mean, boosting the use of airplanes worldwide.

To enhance the usage of high-speed train systems this mean of transport have been put onto examinations, searching for innovations to boost comfort and speed, from a long time. Following this effort, Robert Goddard, appealed as the father of the liquid rocket motor, wrote an article in 1909 entitled 'The Limit of Rapid Transit', where he described improvements in a high-speed rail system. On the article Goddard introduced the use of levitating pods and a vacuum-sealed tube to achieve a viable connection between Boston and New York in only 12 minutes [5].

As a materialization of Goddard concepts, Hyperloop appeared in 2013 at the hand of the multimillionaire Elon Musk. This idea was not totally new for the time, but appeared as the first real application mixing the use of a vacuum tube framework to reduce the aerodynamic drag and a levitation system which reduces the mechanical friction to obtain an improved cruise speed with respect to conventional high-speed trains. Despite the immaturity of the idea, other companies jumped into the race for development giving rise to companies such as Zeleros [5].

Zeleros is a Spanish company based in Valencia, which main purpose is to impulse new and clean means of transport, including the development of Hyperloop systems [6]. Zeleros concept of Hyperloop present big similarities to the idea presented in Hyperloop Alpha, the model includes an axial compressor and levitation system which will be delved into later in the document.

Regardless of the huge technological efforts from the companies, the reality of the Hyperloop project feasibility remained unknown. NASA article [7] delves into the feasibility of the project, analyzing the commercial potential, environmental impact, safety considerations and their competence against other well established means of transport. Concluding that this high speed mean of transport "can be optimized to meet market demand without prohibitive costs to the operator". The usage of a closed capsule system requires much bigger investment compared to open systems such as the conventional high-speed train. Nevertheless, the great improvement in the aerodynamic performance outweighs the investment needed per kilometer of rail, thanks to the great achievable velocities.

Elon Musk through Tesla corporation, gave form to the concept of Hyperloop through the article Hyperloop Alpha [8], where the feasibility of this transport system for a line connecting Los Angeles and San Francisco is investigated. The proposed design includes air bearings skis for levitation with an integrated suspension, a compressor fan powered by on-board batteries to reduce the blockage and bleed air to the bearings and a linear electric motor to accelerate the pod. This last element locates on the tube the stator of the motor (weight saving) and the rotor on the pod. The disposition of the capsule seats and the previous mentioned elements are shown in Figure 1.2.1.

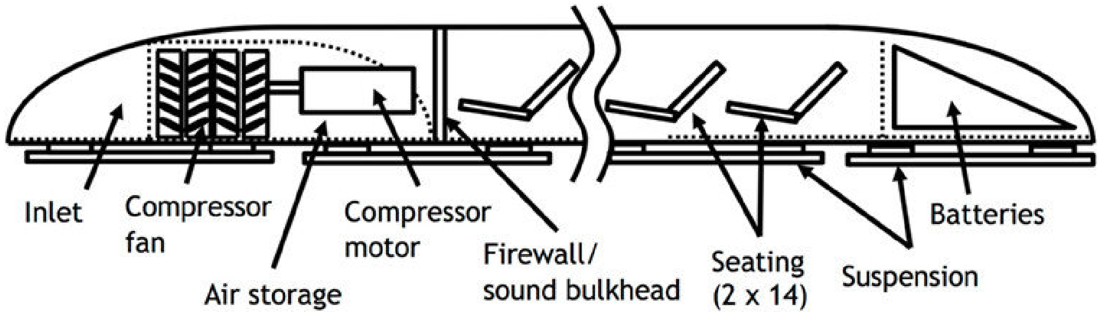

Figure 1.2.1: Design distribution of a Hyperloop [8]

For a comfortable and safe travel the Hyperloop system will operate at high subsonic speeds, avoiding blockage and excessive drag. The tube pressure will be decreased to a value where the drag is minimal but pumps are able to work in case of leakage, maintaining the system operability despite of the air spills. The capsule and tube frontal areas and dimensions are designed to reduce blockage, as well as the front axial compressor. The article Hyperloop Alpha size the aerodynamic and geometrical of the system, a summary of this figures appear on Table 1.2.1.

Aerodynamic properties		Geometrical properties	
Cruise velocity, $[kph]$	1220	Capsule width, $[m]$	1.35
Cruise Mach number, $[-]$	0.99	Capsule height, $[m]$	1.1
Tube pressure, $[Pa]$	100	Capsule frontal area, $[m^2]$	1.4
Capsule Drag, $[N]$	320	Capsule diameter, $[m]$	2.23
Bearing Drag, $[N]$	140	Tube frontal area, $[m^2]$	3.91
Fan power, $[kW]$	350	Capsule weight, $[kg]$	3100
Compression ratio, $[-]$	20	Batteries weight, $[kg]$	1500

Table 1.2.1: Hyperloop summary of characteristic figures [8]

The flow inside the tube is perturbed by the pod high velocity, causing the acceleration of the air around the pod, which is forced to pass between the narrow section left between the pod and the tube (see Figure 1.2.2). For a given section of the tube and the pod there will consequently exist a maximum velocity limit for which the flow around the pod becomes choke. As sonic conditions are achieved no more mass flow can be transferred between the pod and the tube, resulting in a flow blockage for higher Mach numbers. This limit due to the sonic condition is known as the Kantrowitz Limit (KL) and relates the blockage ratio (BR) with the pod Mach number (M) Equation 1, defining the blockage ratio as $BR = A_{pod}/A_{tube}$ (A_{pod} is the pod cross-section area and A_{tube} is the tube cross-section area) [9].

$$BR = 1 - M \left(\frac{1 + \frac{\gamma-1}{2}}{1 + \frac{\gamma-1}{2} M^2} \right)^{\frac{\gamma+1}{2(\gamma-1)}} \tag{1}$$

Therefore above the KL, blockage of the flow will be produced, and part of the flow will be restricted to pass, the pod will start behaving like a piston and adverse increase of the pressure will be produce in the front of the vehicle, whereas the pressure will decrease at the tail of it. This effect leads to serious increase in the drag forces experienced in the pod, restricting the maximum speed achieved by the pod and boosting the energy consumption.

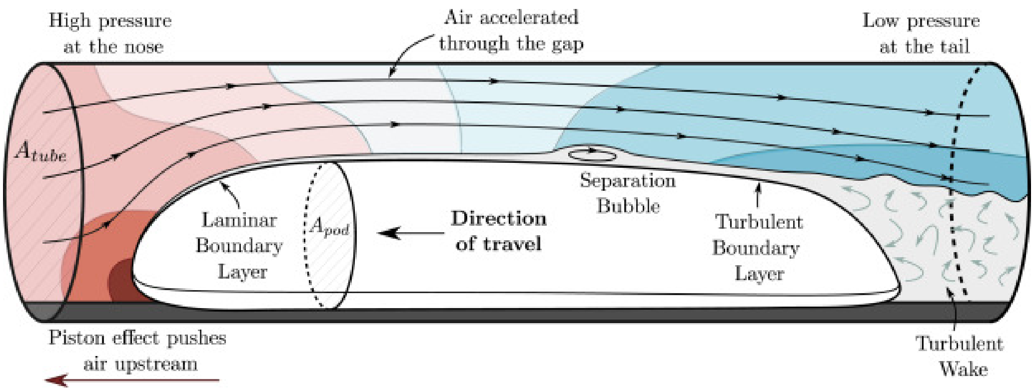

Figure 1.2.2: Aerodynamics of a Hyperloop [10]

In order to diminish the amount of blockage, decreasing the drag, the BR should be minimal, to reduce the acceleration through the gap and the piston effect depicted in Figure 1.2.2. Nevertheless, this is not an option, since it will exponentially increase the cost of rail per kilometer, boosting the infrastructure cost for the project. A real alternative is to add an axial compressor in the front of the vehicle, this compressor will remove the pressure increase upstream of the vehicle improving the aerodynamic performance and decreasing the blockage effects [8]. The compressed air will be bypassed to the rear part of the pod, where a nozzle will expand the gases to mitigate the wake drag.

Including a compressor was already part of the preliminary design introduced in the article Hyperloop Alpha. Nevertheless, there hasn't been a real will to investigate the compressor behavior under the conditions imposed in the tube, and few studies have addressed this question.

In of the latest studies, Lluesma-Rodríguez et al. [11] investigated the feasibility and performance of a Hyperloop system, focusing on the use of an axial compressor for propulsion and drag reduction within a low-pressure framework. The study employs Computational Fluid Dynamics (CFD) simulations to analyze the effect of the axial compressor on the blockage, and therefore, also in the power consumption. The article concludes the effectiveness of the aerodynamic compressor in reducing drag and enhancing propulsion efficiency, leading to 70% energy reduction under a 0.5 BR. The introduction of a compressor allows the system to operate in tunnels with blockage ratios even 2.8 times higher. The research inaugurates the effort to study the advantages of axial compressors in this system.

Whereas Bizzozero et al. [9], follow the same line of study, completing CFD simulations to explore the aerodynamic performance of a Hyperloop pod fitted with a compressor to mitigate the KL. According to the article, the performance of the compressor boosted for conditions above the KL, achieving a maximum power reduction of 47.5%.

Both models for simplification purposes used axial compressor simplified models, establishing a pressure ratio without including the axial compressor inside the CFD model. Therefore, the necessity of studying the behavior of the axial compressor within the low-pressure tube conditions arises. Becoming CFD a great tool to investigate the effects under the given conditions of operation, without the need of expensive experimental setup.

1.3 Objectives

The aim of this project is to study the performance of an axial compressor under the mentioned low-pressure conditions achieved in the tube, quite below the atmospheric one. Computational Fluid Dynamics (CFD) simulations are used to investigate the effects of the operation pressure reduction within a specific geometry, NASA ROTOR-37, experimentally tested by NASA [12]. This compressor is chosen due to the availability of geometric and experimental data provided by NASA.

Although only the experiment have been conduced under atmospheric pressure of operation, this point serve as a validated starting point. Four cases with decreasing pressures of operation are compared, under the same corrected mass flow, targeting the study of the compressor performance under different pressure points. The document includes the techniques used to achieve initialization and convergence over the required corrected mass flow.

Also as a capital objective, the results and flow patterns are compared to a real Hyperloop axial compressor CFD for similar pressures of operation. Aiming the validation of the flow patterns found under a real Hyperloop geometry proposed by Zeleros and studied in previous analyses. To sum up, the project aims to main objectives:

- Validate the CFD results of an axial compressor geometry with the experimental results obtained for the NASA R-37 compressor.
- Study the performance trend of an axial compressor with a NASA R-37 geometry, when decreasing the pressure of operation. This pressure decline will be smoothly studied through four points, reaching up to the pressure of a Hyperloop tube framework.
- Compare and validate the tendencies in performance of the NASA R-37 compressor with a real Hyperloop model studied by Galindo et al. in [13], when decreasing the pressure of operation and therefore the Reynolds number.

1.4 Methodology

Due to the lack of experimental facilities of Zeleros to test this type of compressor under the low-pressure conditions, computational fluid dynamics simulations becomes the most feasible approach to study the given objectives. Therefore, for the project development the program SIEMENS STAR CCM+ 2310 is used, a globally used software, employed in axial compressor simulations under an infinite variety of boundary conditions.

Based on the literature review the and the nature of the problem, a different approach to the conventional used in compressors studies was used. Instead of varying the operational rotational speed, changes in the operational pressure will be implemented. This pressure will be decreed until candidate operational pressures of a real Hyperloop tube system are achieved [13].

This CFD study is divided into four cases with decreasing pressures of operation to ensure a smooth study to see gradually the effects and be able to compare it to the Hyperloop case presented by Galindo et al. [13]. The four cases will have the same corrected mass flow rate, whereas their respective pressure of operation will be of 100 kPa, 40 kPa, 10 kPa and 4 kPa.

The CFD configuration will basically consist of unstructured mesh with wake refinement of around 1.5 million cells [14]. The geometry of the compressor is divided axisymmetrically so that only one blade (from 36) is analyzed, reducing the computational domain and effort. Two periodical conditions are set on the lateral walls to accomplish the symmetry respect to the rotor axis.

Regarding the simulation models as previously mentioned they will be: gas, 3D, axisymmetric... A steady model is used to further simplify the calculation efforts. Whereas the turbulence is simulated with a K-Omega turbulence model through Reynolds-Averaged Navier Stokes (RANS) equations. A Gamma-ReTheta Transition model is also employed in CFD simulation. Finally coupled equations are used to solve the cases due to the huge density gradients that appear in the shock-waves.

1.5 Outline

The document will be divided into three main parts: Memory, Budget and SDGs.

The Memory consist of 5 chapters, where the pressure of operation effects on the compressor performance results and conclusions are included. At the same time each chapter is subdivided on its correspondent sections. The first chapter includes the introduction, presenting the background and motivation for the topic of the study, methodology and main objectives followed in this work.

The second and third chapter correspond to the theoretical base needed to preform the analysis of the compressor performance. The second chapter will address the principles of axial compressors, delving into the characteristics of the used geometry (NASA R-37) and the fundamentals of compressors operating regimes. Whereas the third chapter will include the configuration used in the CFD models (mesh, boundary conditions, models selection...) and initialization and convergence techniques.

The fourth chapter the results obtained in the CFD simulations are exposed. The differences among the models and possible calculations errors are included in this chapter. Finally, the fifth chapter includes the conclusions, embracing the ideas obtained from the analysis, as well as the limitations that the computing methods have.

Furthermore, the project includes a series of different annexes, which will contain supplementary information of: the results (Appendix A), the Sustainable Development Goals (Appendix B), the parametrization of the domain (Appendix C), the overall and separated cost estimation of the project (Appendix D) and the legal and programming conditions, used in the CFD simulations (Appendix E).

2 Background

To decrease the pressure at the front of the pod a compressor is needed. In this section the basics of compressors, the selection of a proper one for a Hyperloop study application and the chosen rotor geometry for the project are explained.

2.1 Basics of axial compressors

A compressor is defined as a mechanical device used to increase the pressure of a compressible mean by reducing its volume or velocity. It operates on the principle of thermodynamics, where energy is added to a gas to compress it. In Hyperloop applications the become an essential part to decrease the drag, while bleeding pressurized air for levitation purposes. The most general classification divides this machines into two:

- Positive displacement compressors: their operation consist on trapping a fixed amount of gas and then mechanically reducing its volume to increase its pressure, through a mechanism. At the same time they are subdivided into:
  - Reciprocating compressors: are a type of positive displacement compressor where gas is compressed by a piston back and forth movement inside a cylinder.
  - Rotary compressors: are a type of positive displacement compressor that use rotating elements to compress gas, such as a screw or vane mechanism.
- Dynamic compressors: increase the pressure of fluid by transmitting velocity (kinetic energy), which is then converted into pressure energy. At the same time they are subdivided into:
  - Centrifugal compressors: are a type of dynamic compressor that use a rotating impeller to impart radial velocity to a fluid, which is transformed into pressure in the diffuser.
  - Axial compressors: are a type of dynamic compressor where the rotor blades accelerates the flow and the stator blades transform the kinetic energy into pressure.

For this project only dynamic compressors are feasible for transport applications, since the can handle high flow rates, produce continuous operation and their efficiency in converting kinetic energy into pressure is superior to the other compressor type. Inside dynamic compressors, centrifugal achieve greater pressure ratios but cannot sustain big mass flows. Therefore, the most feasible option to compress the air in from of the pod is to implement an axial compressor. It's easier integration and high mass flows handling, makes the axial compressor the focus of this work.

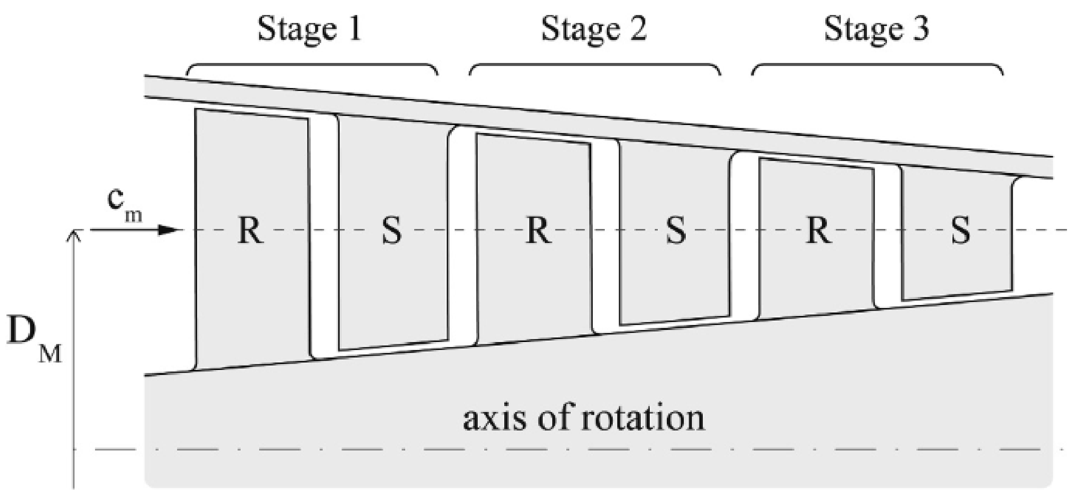

Figure 2.1.1: Compressor scheme [15]

In an axial compressor the gas will always move axially, parallel to the axis of rotation. The fluid will be compressed by a series of stages, which consist of one rotor that rotates transmitting high relative velocities to the flow and a stator that is fixed to the hub and decelerates the flow converting kinetic energy into pressure. A compressor is formed by many stages, see Figure 2.1.1, to achieve a constant pressure raise without excessive flow detachment or stall. Depending on the total pressure ratio needed for the application more or less stages will be implemented. The raise on pressure is thermodinamically related with the raise of temperature, which is a problem in Hyperloop applications. Therefore, the flow needs to be refrigerated before being used in cabin bleeding.

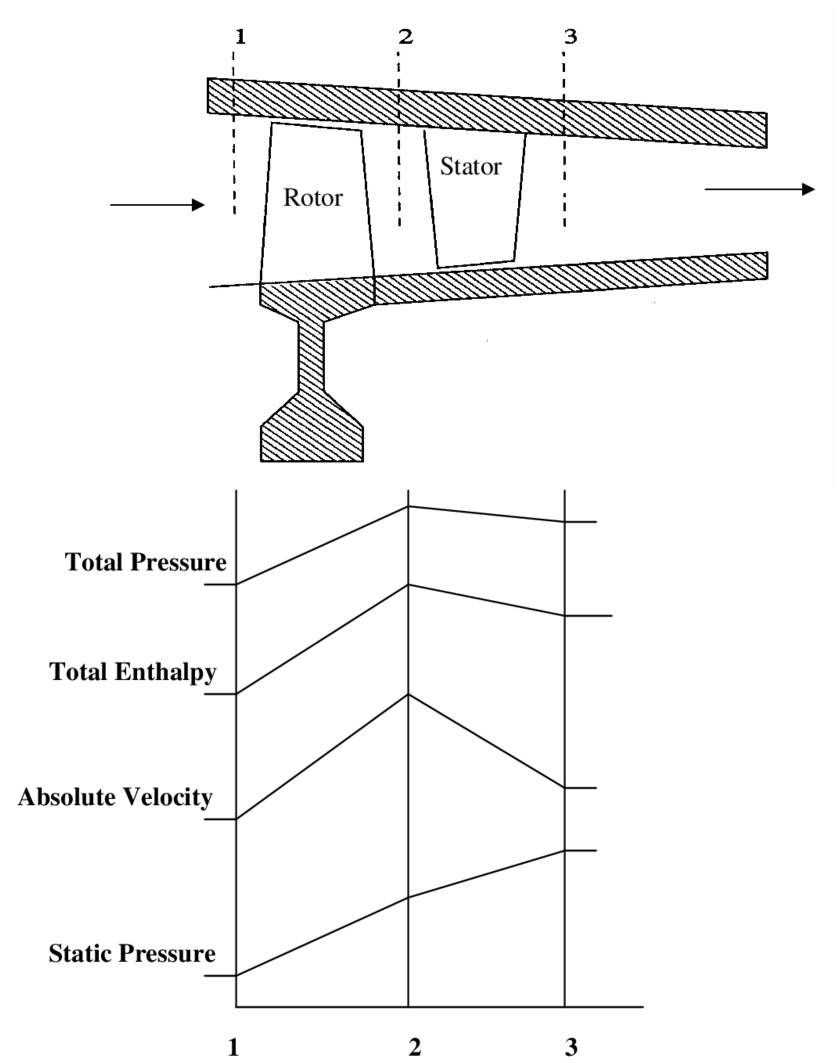

Figure 2.1.2: Evolution of thermodynamic variables across the rotor and the stator [16]

Figure 2.1.2 depicts how the thermodynamic variables evolve during one stage of the compressor. Total pressure and enthalpy will increase in the rotor. This is due to the increase in absolute velocity generated on the rotor, which causes higher dynamic pressures. In the stator the static pressure and enthalpy will slightly decrease. The stator decreases the absolute velocity, diminishing the dynamic pressure. The static pressure will grow similarly in both the rotor and the stator. Is important to note that the rotor in a compressor stage always precedes the stator.

This section will focus in the future on rotor basics since they are more important for the CFD analysis. However, it is important to know the background and overall performance of compressors in first instance.

2.1.1 Compressor map

One of the most representative figures when talking about compressors are compressor maps. This graphical representations are used in turbo-machinery, to describe the performance characteristics of a compressor. Particularly Figure 2.1.3 shows a compressor map for an axial compressor.

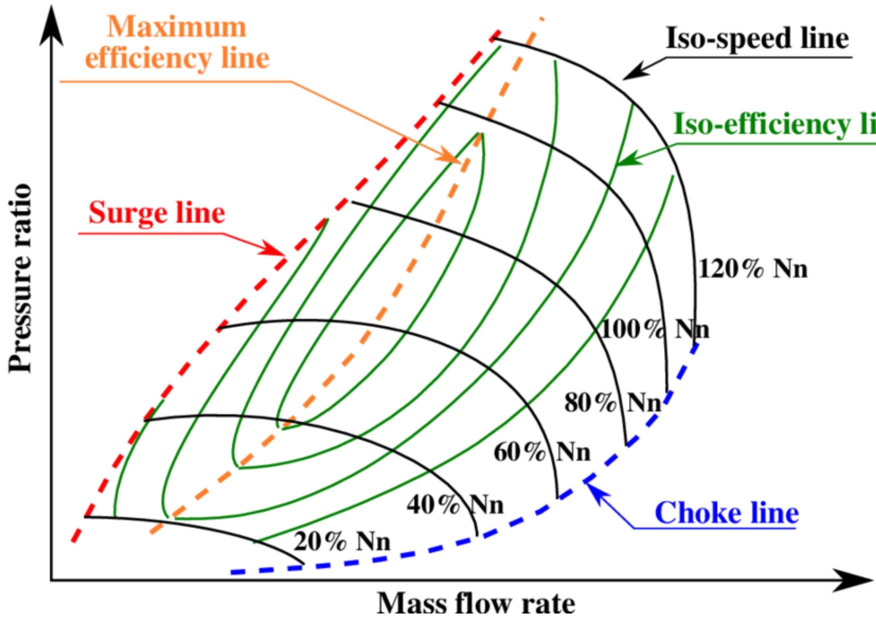

Figure 2.1.3: Performance characteristic map for an axial compressor [17]

The performance compressor map shows the performance of an axial compressor when varying the mass flow rate and the pressure ratio (Equation 20). The graph illustrate a series of iso-efficiency lines that form islands that enclose all the operation points with a higher efficiency to a certain value. The operational regime is characterized by the speed lines, for which the rotor carries the same rotational velocity. This line show a maximum efficiency for a certain mass flow, which is depicted by the maximum efficiency line. On the other hand, there are two limits of operation, where surge or choke are produce. Surge or stall is produced by an excessive incidence angle and therefore a huge work load on the blade. This effect directly leads to a complete loss of the compressor performance and sudden decline on the pressure ratio. Near the surge line, the pressure ratio will almost remain constant despite decreasing the flow rate. Choke will be caused by sonic conditions at the throat of the passage between the blades, therefore no more mass flow will be admitted to pass. Near the choke line despite decreasing the pressure ratio abruptly there isn't an increase in the mass flow rate.

At this moment is worthy to define two coefficients, important in turbo-machinery flow analysis. The flow coefficient, ϕ, and the work coefficient, φ, are defined in Equation 2 and Equation 3. Where U equals the rotational velocity at a certain span.

$$\phi = \frac{V_x}{U} \tag{2}$$

$$\varphi = \frac{\Delta h_0}{U^2} = \frac{V_{\theta 2} - V_{\theta 1}}{U} = \frac{V_x \cdot (\tan\alpha_2 - \tan\alpha_1)}{U} = \phi \cdot (\tan\alpha_2 - \tan\alpha_1) \tag{3}$$

The flow coefficient is parameter that determines the efficiency at which the rotating shaft transfer energy into the fluid. Whereas, the flow coefficient determines the amount of work done on the fluid by the rotor.

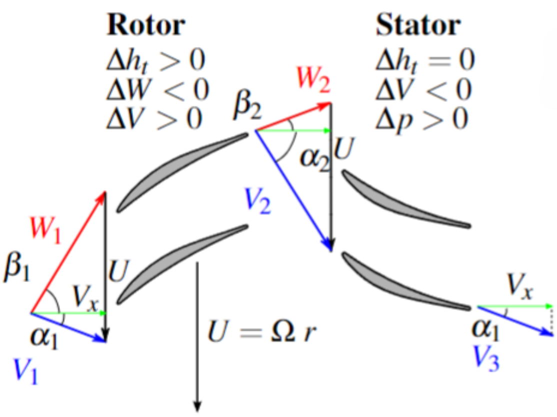

Figure 2.1.4: Velocity triangles for axial compressor stage [17]

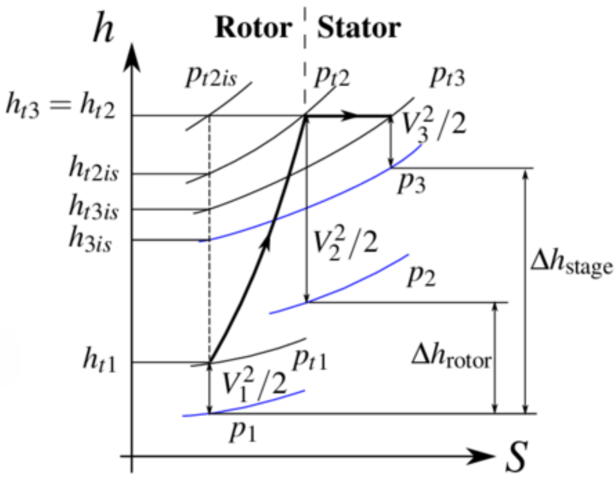

Figure 2.1.5: Enthalpy diagram for a typical compressor stage [17]

Figure 2.1.4 illustrates the effects on the absolute velocity, represented by the angle α and the relative velocity, represented by the angle β. As stated, the rotor will turn the flow away from axial, meaning that the absolute velocity increases, α increases. On the stator, the flow is turned towards axial, meaning that the relative velocity increases, β increases. The axial velocity, V_x, can be considered constant along the stage. Note that the flow is not completely axial at the entrance of the stage, unlike in the CFD case.

Figure 2.1.5 shows the enthalpy-entropy diagram for an axial compressor. The absolute enthalpy variation between the rotor and stage, which is traduced into the work done in each step, is the same (reaction degree of 0.5). Whereas the relative enthalpy will be the constant among the stator, since no work is done on the flow (the stator is fixed). The absolute enthalpy variation across the stage is measured as the difference in kinetic energy between the inlet and the outlet. Note that due to frictional losses the relative pressure on the rotor and absolute pressure on the stator decrease.

2.2 Flow patterns on a transonic compressor blade

Prior to the CFD analysis, the main characteristics of the flow will be commented. Is important to characterize the flow patterns inside the rotor of the compressor. Therefore, in this section all the flow interactions with a blade from the compressor will be studied. First of all, secondary flows will be addressed, then other flow patterns around the blade, will be explained, including shock waves under the different flow regimes.

2.2.1 Flow patterns

This subsection addresses the generalities of the flow contour around the blade. Specially, the flow patterns around different mass flow conditions are studied, and bring a grateful insight for the future analysis.

As seen in Figure 2.1.3, there are three main regions on a iso-speed line (stall, operating point and choke). Figure 2.2.1 shows the disposition of the shock waves for different mass flow conditions, from near stall to choke conditions, for a constant wheel speed. As a generality for all the conditions, in transonic rotors an oblique shock wave will be placed upstream of the leading edge, due to the high wheel speeds. For low mass flow rates, near stall operating condition, the shock wave will become normal to the incoming flow flow and will be displaced upstream of the leading edge. Under this conditions the shock wave will reassemble more to a bow shock.

As the mass flow rate grows up to the chocking operating conditions, the shock wave principle will collapse with the leading edge. Moreover, the shock wave will be straight and the passage flow will be accelerated up to Mach 1. Therefore a normal shock wave will appear at the passage throat. Finally is worthy commenting that the design operating condition will reassemble to the choking condition. The shock wave will be straight and it's principle will collapse with the leading edge. However, the passage flow will not be supersonic and therefore no shock wave will appear on the throat.

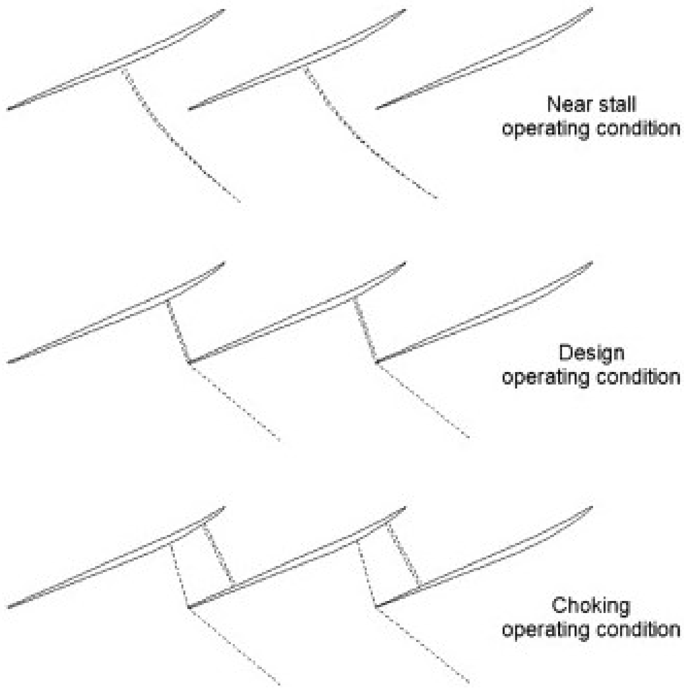

Figure 2.2.1: Shock wave configuration inside a transonic compressor rotor [18]

2.2.2 Secondary flows

Secondary flows are defined as the flow of particles in a different direction to the free stream. In this section the different vortexes generated by this effects will be exposed and discussed.

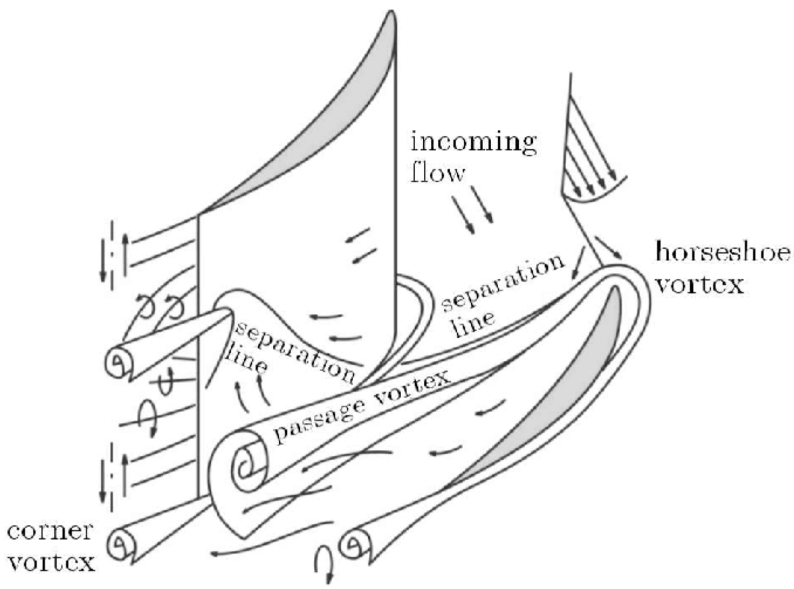

Figure 2.2.2: General view of the secondary flow structures on a blade [19]

First of all, Figure 2.2.2 shows a general image where all the secondary flow effects around the blade are depicted. It is important to note the three main vortexes which will be further discussed in detail are: the passage vortex, the horseshoe vortex and the tip clearance vortex. Moreover, there are three minor effects presented on the image. The first of them is the concentrated shed vortex and is generated by the separation at mid-span of the flow in the suction face. The second one is the trailing edge vortex, generated by the difference of radial velocities between the suction and pressure side. Finally the effect to the corner vortex, due to a minor interaction between the hub and the extrados.

Horseshoe vortex and corner separation

The upstream boundary layer to the blade, will interact with the boundary layer generated by the body, increasing therefore in thickness specially on the corner of the junction. At this point, where the trailing edge intersect the hub, the pressure gradients will produce a 3D flow separation. Except for very low Reynolds numbers, associated to laminar flow nature, the flow will show high-intensity unsteady structures of the flow within the turbulent boundary layer. This vortex will be affected by the intensity of adverse pressure gradient on the suction side.

Regarding horseshoe vortexes, the presence of an obstacle and it's blockage on the flow causes the boundary layer to form this kind of vortexes. The stagnation point at the leading edge becomes the separation of the two lines of the vortex, towards the pressure and suction faces of the blade, traveling downstream. On the suction side the adverse pressure gradient will cause the separation of the flow.

In the particular rotor framework, the blade will be thinner, whereas the adverse pressure ratio on the blades will be higher. Therefore, the importance of the horseshoe vortex will be smaller than the one of the corner separation vortex. Especially for low Reynolds numbers the corner separation will cause a bigger wake for the lower span regions.

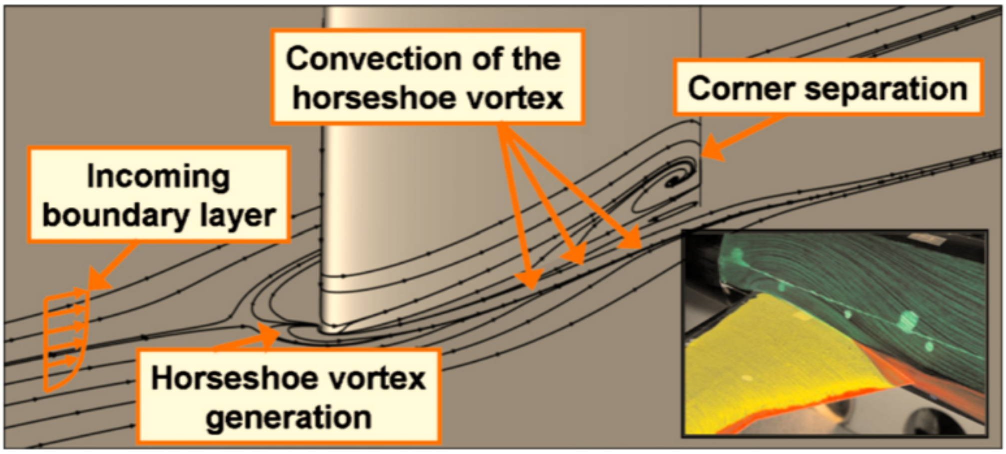

Figure 2.2.3: Horseshoe vortex visualization [17]

Passage vortex

The passage vortex or the cross flow is depicted in Figure 2.2.4. This effect consist on the span-wise rotation of the flow due to frictional effects.

The flow is considered as totally axial, with a non-uniform velocity profile as a result of the boundary layer formation in the hub. The fluid in the boundary layer (particle A) will have a lower axial velocity (V_A) than the fluid in the free stream outside this viscous layer (particle B), which will have a higher axial velocity (V_B). It is assumed the same pressure field in the span wise direction across the passage. The particle B will follow the blade shape, as the centrifugal force is balanced with the transverse pressure gradient force. Whereas, particle A, as it has a lower momentum, it will need to have a smaller radius of curvature to achieve the same centrifugal force to compensate the transverse pressure gradient force [17]. As a result the curvature near the hub will be smaller, leading to a cross-passage motion and lower total pressure near the corner between the suction side and the wall. Consequently, the re-circulation pattern shown in Figure 2.2.4 will occur inside the passage.

$$\frac{V^2}{r} = \frac{1}{\rho}\frac{\partial p}{\partial r} \tag{4}$$

The equilibrium equation can be written in a cylindrical reference frame (r,θ,x), in the radial direction as Equation 4. Relates the above the above particle momentum with the pressure gradient.

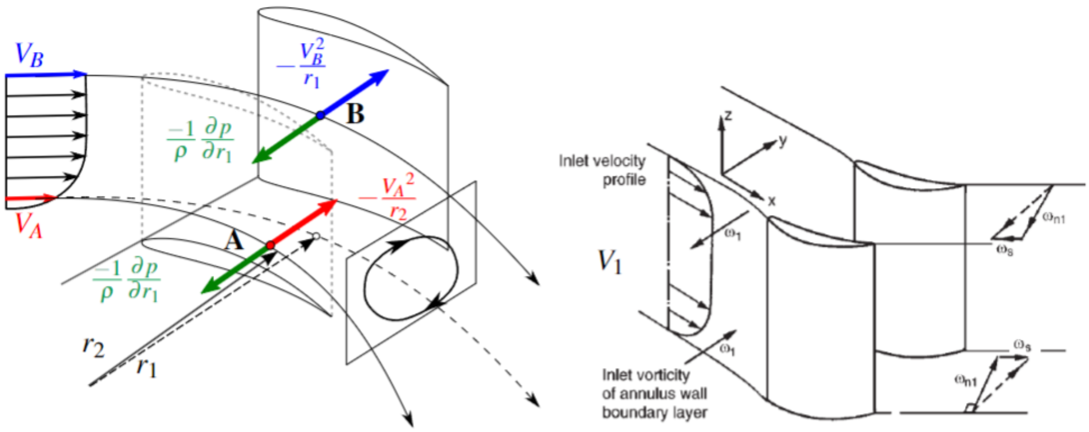

Figure 2.2.4: Passage vortex visualization [17]

Tip leakage vortex

Finally Figure 2.2.5 shows the last relevant secondary effect, the tip clearance vortex. Tip leakage consist on the flow movement from the pressure to suction side of the blade. As it is logical, the flow will move towards the lower pressure zones, generating the leakage vortex. Moreover other effects can be seen, a separation bubble (b1) is shown on the blade tip, accompanied usually there is a second recirculation zone (b2) on the shroud. The leakage vortex will depend on the distance between the blade end and the shroud and also on the flow Reynolds number (nature of the boundary layers).

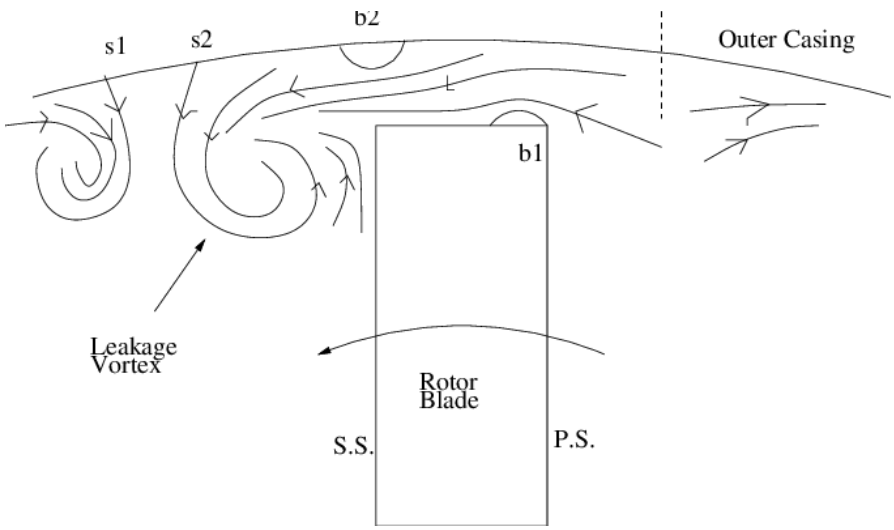

Figure 2.2.5: Tip leakage vortex [20]

2.3 NASA Rotor 37

NASA ROTOR-37 has been the chosen geometry for this analysis, for two main purposes. The experimental results conduced by NASA, bring a great insight into the analysis and serve as a validate tool for the ambient pressure case. Moreover, the facility to obtain an accurate CAD model to the reality makes more feasible this analysis.

2.3.1 Blade cascade geometry

First of all, this section will inquire in the blade cascade geometry basics, to bring an important insight previous to the geometry analysis. The blade cascade consist of a 2D iso-span representation of the blades. The circumferential section at a certain radius is displayed, aiming a 2D and perpendicular representation which help understanding the geometry. On this section some of the most relevant parameters and nomenclature used on defining the shape of the blade at a certain span are used.

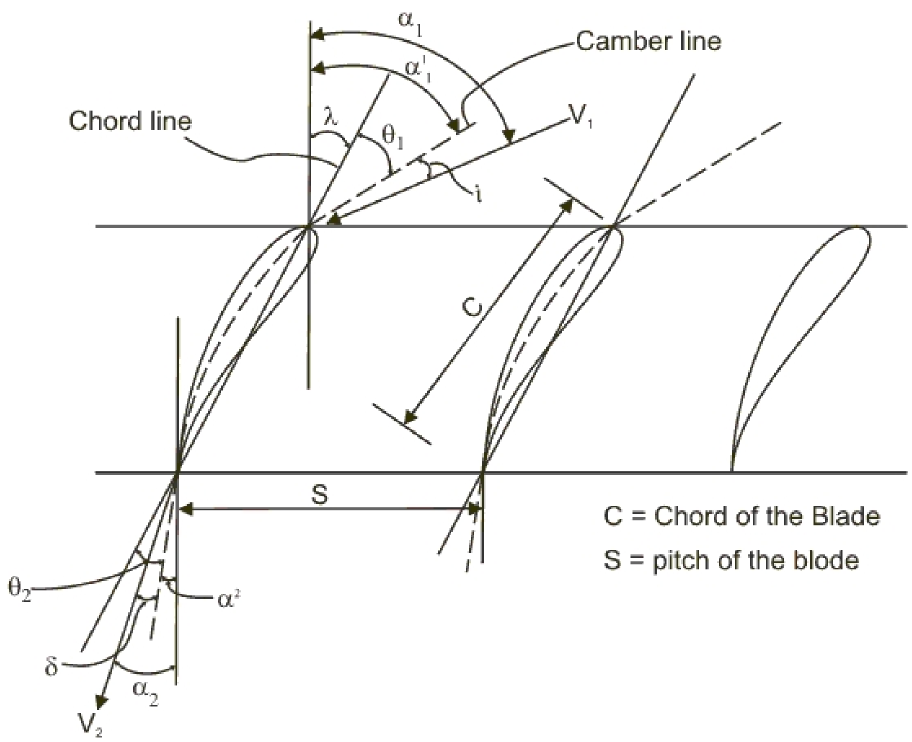

Figure 2.3.1: Blade cascade nomenclature for shape definition of the blade at a certain span [21]

Figure 2.3.1 shows the nomenclature on the blade cascade configuration for a compressor stage. The chord of the airfoil is defined as C, and corresponds to the distance between the leading and trailing edge. The pitch of the blade corresponds to the circumferential distance between the trailing edges of two consecutive blades. This parameters define the solidity (σ), as seen in Equation 5. The solidity will determine if the passage is width or narrow, affecting to the flow patterns across it.

$$Solidity = \sigma = \frac{C}{S} \tag{5}$$

On the figure the camber line is defined as the dashed line and is asymmetric between the two surfaces of the blade. This line defines the metal angle α' in the image, which equals to β, across this work. The chord line is depicted as a solid line, and passes through the trailing and leading edges. This line defines the stagger angle (λ), which determines the twist of the blade with respect axial direction. The camber angle (θ) will be defined as the angle between the camber mean line and the chord line at the trailing edge.

The velocity angle with respect to the axial direction will be defined as the angle of attack (α). Furthermore, the inlet velocity angle with respect to the mean camber line at the leading edge defines the incidence angle, see Equation 6. The deviation angle corresponds to the he outlet velocity angle with respect to the mean camber line at the trailing edge, see Equation 7.

$$Incidence = i = \alpha_1 - \beta_1 \tag{6}$$

$$Deviation = \delta = \alpha_2 - \beta_2 \tag{7}$$

2.3.2 NASA Rotor 37 performance

NASA Rotor 37 is a widely studied transonic axial compressor rotor, which enhanced the understanding of high-speed axial compressor performance. Reid and Moore conducted experimental research on it [12]. Despite the age of the study, the performance levels and the geometry of this rotor reassemble to the most advanced one, having serve as a cornerstone in the study of axial compressors.

The compressor consists of a 36 multiple-circular-arc (MCA) blades. The geometric parameters consist on: a inlet hub-tip radius ratio of 0.7, a blade aspect ratio of 1.19, a solidity of 1.29 and a tip clearance of 0.0356 cm. The low solidity determines that the transonic rotor, is design to avoid blockage, maintaining a high mass flow rate, while achieving a lower pressure ratio. In fact the performance parameters are: a total pressure ratio of 2.106, a total temperature ratio of 1.27, an adiabatic efficiency of 0.877, a rotor head rise coefficient of 0.333, a flow coefficient of 0.453 and a mass flow rate of 20.188 kg/s.

The experiments are performed under a wheel speed of 17188.7 rpm which correspond to a supersonic tip speed of 454.14 m/s. The experimental conditions where based on ISO standards, where the temperature was 288.15 K and the pressure was 101325 Pa. The maximum mass flow rate at the given wheel speed was measured to be 20.93 kg/s at chocking conditions.

All the mentioned performance parameters for NASA Rotor 37 are summed up in Table 2.3.1. The parameters are obtained at the design point, achieving supersonic inlet conditions. The geometric parameters are obtained at the mean span, which correspond to 50%.

PARAMETER	DESIGN VALUE
Rotor Total Pressure Ratio	2.106
Rotor Total Temperature Ratio	1.270
Rotor Adiabatic Efficiency	0.877
Rotor Head Rise Coefficient	0.333
Flow Coefficient	0.453
Mass Flow [kg/s]	20.188
Rotor Wheel Speed [rpm]	17188.7
Rotor Tip Speed [m/s]	454.14
Hub / Tip Radius Ratio	0.70
Rotor Aspect Ratio	1.19
Number of Rotor Blades	36
Blading Type	Multiple Circular Arc (MCA)

Table 2.3.1: NASA Rotor 37 design parameters [12]

2.3.3 NASA Rotor 37 geometry

Figure 2.3.2 shows the experimental rotor used by NASA on the experiments, whereas Figure 2.3.3, depicts the CAD model used in the CFD simulations. Note that the views are not equal, being one taken from the rear and the other from the front.

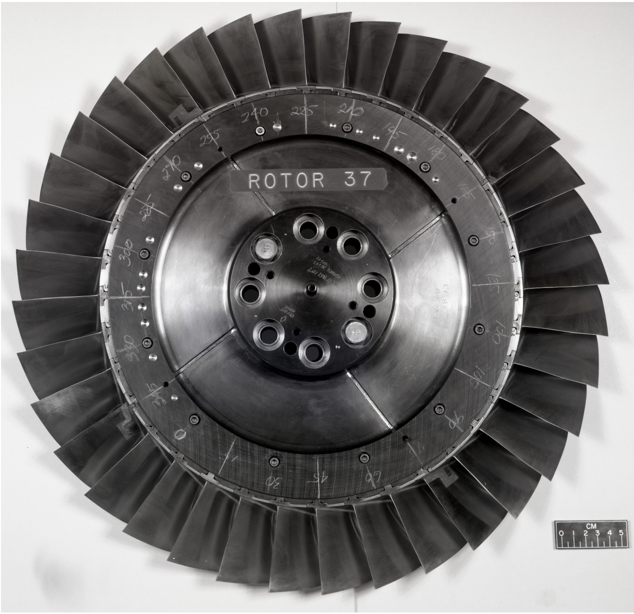

Figure 2.3.2: Rear view of the NASA Rotor 37 experimental rotor [22]

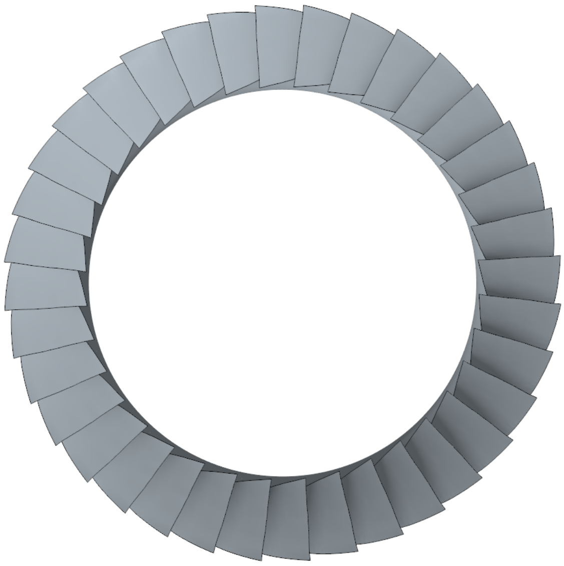

Figure 2.3.3: Front view of the NASA Rotor 37 CFD rotor

Both images show evident similarities with respect to the geometry, in fact the CAD model is accurate to reality in terms shape and dimensions. However, the CAD model does not include some of the tiny protuberances on the hub and the shroud, for the aim of simplicity. As it will be analyzed in the future one of this small gaps will cause numerical discrepancies between the CFD simulations and the experimental results.

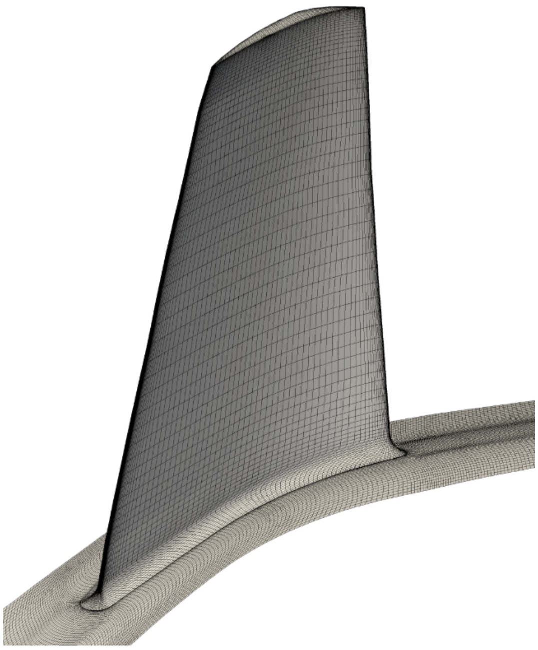

Figure 2.3.4: NASA Rotor 37 lateral cut [23]

The geometry of NASA Rotor 37 blade is a finely tuned design that addresses the challenges of transonic flow within an axial compressor. Despite the already commented features, such as the MCA blade profile, aspect ratio, tip solidity, and precise clearances, they are other features which also define it's geometry. Blade twist and varied blade section profiles to handle the complex flow patterns at high speeds, are another of the geometric characteristics of the rotor. Figure 3.1.4 shows that the blade will decrease in chord length when increasing the span, due to the higher velocities of the tip. Furthermore, the blade will be more twisted showing a higher inlet metal angle (β_1), but maintaining the same outlet metal angle (β_2). Is also noticeable that due to the decline in the chord length the leading and trailing edges will be tilted downstream and upstream, respectively.

On Figure 2.3.5 the domain of the rotor is parameterized in a series of spanwise and cross-channel planes. This planes will serve for future analysis of the contour of velocities and pressures. Is worthy to note that span is divided in percentage from the hub to the shroud, becoming higher as it approaches the tip of the blade. Furthermore, the axis direction is divided into different stations, where experimental data is obtained as explained in the next section.

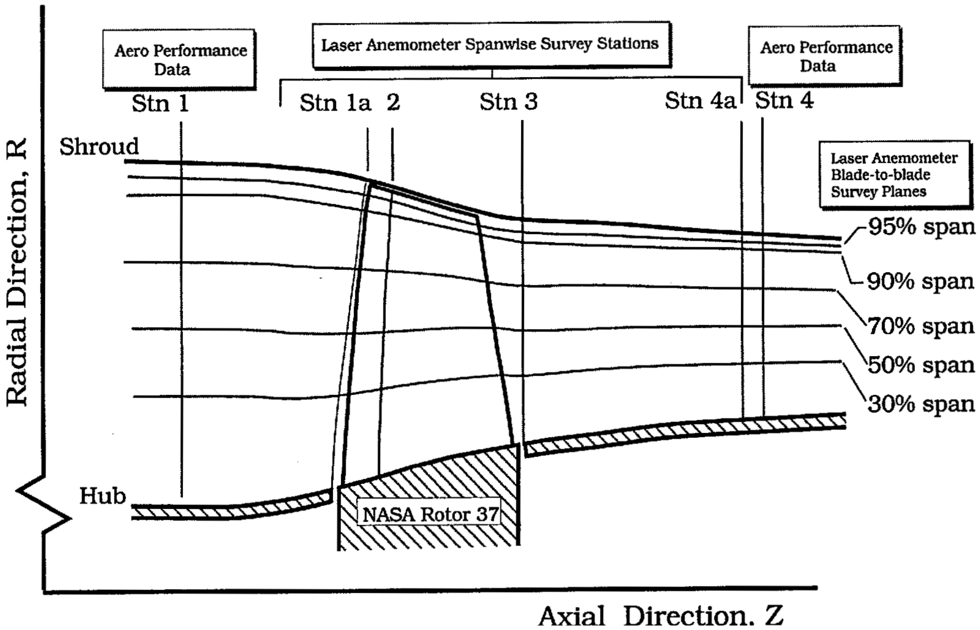

Figure 2.3.5: NASA Rotor 37 lateral cut [24]

2.3.4 Experimental procedure and results

On this section the experimental procedure undertaken by Suder et al [24] is reviewed, investigating in the experimental facilities and techniques.

The Rotor 37 and Stator 37, both forming Stage 37, were designed as the inlet stage of a eight-stage axial compressor. This axial compressor was design to achieve a 20:1 pressure ratio. The rotor was tested isolated to avoid the interference on the flow produced by upstream inlet guide vane or a downstream stator blades. The rotor was representative of the flight hardware at the time, employing multiple circular arc blades, low aspect ratio and a high solidity. The experiments undertaken at the Glenn Research Center were used to study the blockage and losses in an axial compressor. However, huge number of studies have delved into the validation of CFD models through the experimental results obtained in the article.

Figure 2.3.6, depicts the experimental facility used to test Rotor 37. The system is open loop with atmospheric inlet and outlet conditions. The rotor is driven by DC motor. The rotor exit pressure and mass flow is varied using a sleeve-type throttle valve downstream of it.

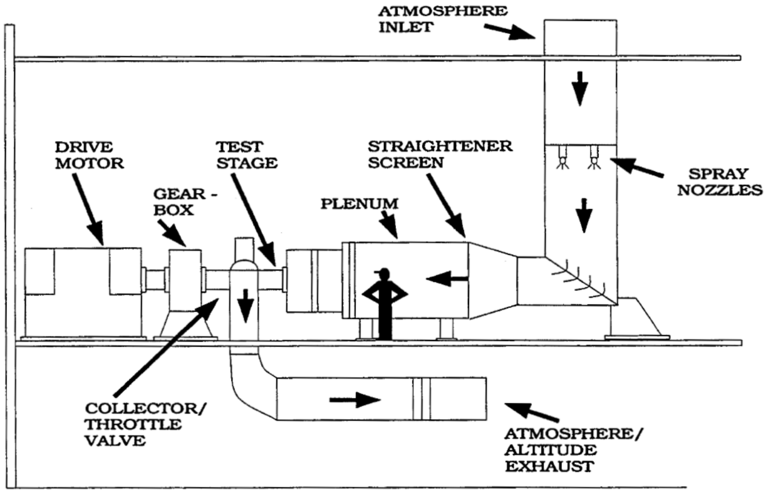

Figure 2.3.6: NASA Rotor 37 experimental facilities (Suder et al. [24])

Probes

A series of probes of two types were used: aerodynamic probes and laser anemometric probes.

The aerodynamic probes were placed in eighteen radial locations (5%, 10%, 15%, 20%, 25%, 30%, 37%, 44%, 51%, 58%, 65%, 70%, 75%, 80%, 85%, 90%, 94%, and 97% span from the hub) at a constant axial location. The axial location of the probes were upstream, station 1, and downstream, station 3, both depicted in Figure 2.3.5.

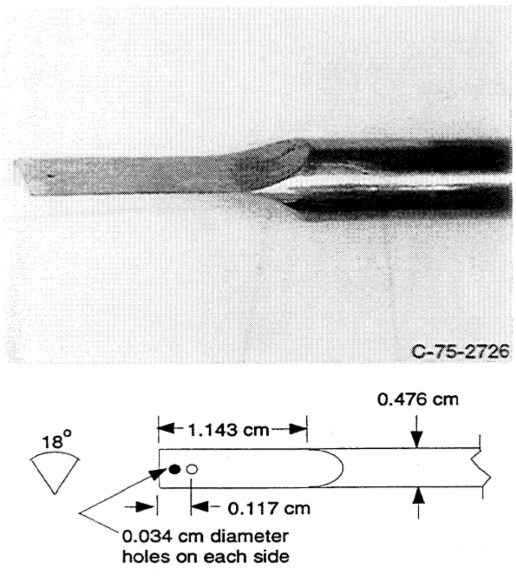

(a) Wedge Probe

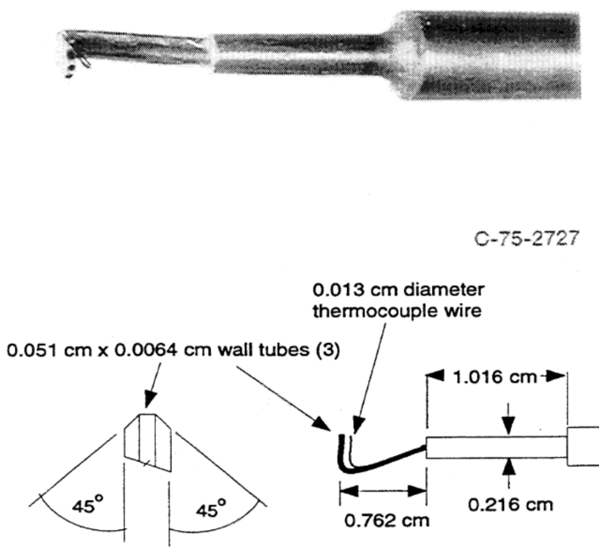

(b) Cobra Probe

Figure 2.3.7: Aerodynamic probes [24]

Figure 2.3.7 shows the two types of aerodynamic probes. The first one correspond to wedge probe and measures the average static pressure and flow angle. The second is the cobra probe and measures average total pressure, total temperature, and flow angle.

A laser anemometer system is used to measure upstream and downstream velocities, acquiring the tangential and axial components of the velocity. A schematic representation of the optical components of the laser anemometer system is provided in Figure 2.3.8. Basically the system allow velocity measurements, through an optical system formed by the mirror, optical devices and a laser beam. This laser beam measures the velocity of seed particles introduced to the flow, which consist on polystyrene latex particles.

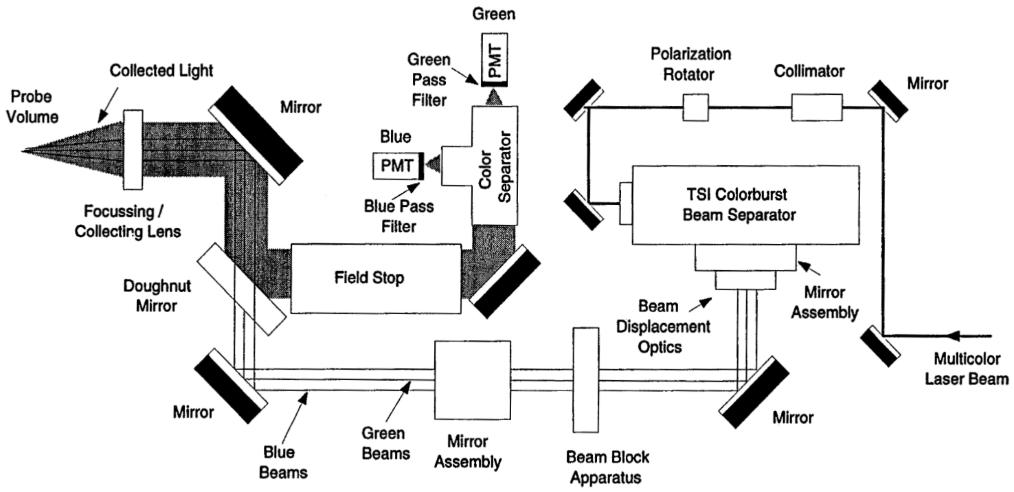

Figure 2.3.8: Schematic of Optical Components Layout in the Laser Anemometer System [24]

The laser anemometer system was used to collect data on two directions: the cross-channel and the laser anemometer stream surface. In both surveys data was acquired across the 36 blade passages at points circumferential resolution of 184 points. Approximately 60000-100000 measurements were taken at each axial/radial location.

The cross-channel survey indicates the flow features in the circumferential and radial direction for a constant axial location (Stations 1a and 3 for velocity). Measurements were taken between 20% and 98% of the span, with a 5% span spacing between points. A lower spacing of 2% was employed near the tip.

The streamsurface survey data is acquired at various axial and circumferential locations at a constant span. The data was obtained for the 30%, 50%, 70%, 90%, and 95% span planes. The axial spacing between points was approximately 5% of the rotor chord.

The static pressure, total pressure, and total temperature measured with the aerodynamic survey probes at stations 1 and 4 are averaged. Pressure is energy averaged in Equation 8 and temperature is mass averaged across the annulus in Equation 9.

$$\frac{\overline{P_j}}{P_{ref}} = \left[\frac{\sum_{i=1}^{nrp} \left(\frac{P_j}{P_{ref}}\right)^{\left(\frac{\gamma-1}{\gamma}\right)} \rho_{j,i} \left(V_z \, \Delta A_{an}\right)_{j,i}}{\sum_{i=1}^{nrp} \rho_{j,i} \left(V_z \, \Delta A_{an}\right)_{j,i}} \right]^{\left(\frac{\gamma-1}{\gamma}\right)} \tag{8}$$

$$T_j = \frac{\sum_{i=1}^{nrp} T_{j,i} \rho_{j,i} \left(V_z \, \Delta A_{an}\right)_{j,i}}{\sum_{i=1}^{nrp} \rho_{j,i} \left(V_z \, \Delta A_{an}\right)_{j,i}} \tag{9}$$

Note that the subscript j refers to the probe axial location and i to the radial location.

Results

A series of experimental results arise from the rotor tests. The experiments information is principally summed up into Performance Maps, Radial Distributions, Blade-to-Blade flow field contour plots and Cross-Channel flow field contour plots.

On the performance maps the efficiency is computed using Equation 10. In this equation the averaged pressure and temperature at the upstream and downstream stations of the rotor are used (stations 1 and 4 respectively). Moreover, the pressure ratio is also displayed on this maps and computed on Equation 11, averaging the pressure at the given stations.

$$\eta_{ad} = \frac{\left(\frac{\overline{P_4}}{\overline{P_1}}\right)^{\left(\frac{\gamma-1}{\gamma}\right)} - 1}{\frac{\overline{T_4}}{\overline{T_1}} - 1} \tag{10}$$

$$\Pi = \frac{\overline{P_4}}{\overline{P_1}} \tag{11}$$

The Radial Distributions analyze the distribution of pressure, temperature, adiabatic efficiency and blade loading across different spans the radius at the design speed. Throughout the testing program which lasted several years the Radial Distributions where compared, showing a decline in efficiency.

Blade-to-Blade flow field contour plots shows the Mach number contours at the 70% span plane. Generally a blockage occurs on the intrados (pressure surface) near the leading and on the extrados (suction face) near the trailing edge.

Finally the Cross-Channel flow field contour plots, show the circumferential Mach number contours upstream (Station 1a) and downstream (Station 3) of the rotor. Moreover, the flow angle is depicted for these planes, a comparison of this parameter on this project is not interesting and consequently not included.

For the CFD and experimental results comparison the Performance Maps, Blade-to-Blade flow field contour plots and Cross-Channel flow field contour plots are used. This comparison allow an accurate validation of the CFD models. The results figures obtained by Suder et al. are showed in future sections and therefore are not included here.

3 Numerical model

3.1 Geometry and mesh models

3.1.1 Geometry model

The numerical models used in the CFD analysis uses a 3D CAD model of the NASA ROTOR 37 introduced in subsection 2.3. The global domain is depicted in Figure 3.1.1 and Figure 3.1.2. On this figure the walls of the computational domain of the CFD simulation is shown, this walls enclose 1 of the 36 blades disposed axisymmetrically through the rotor.

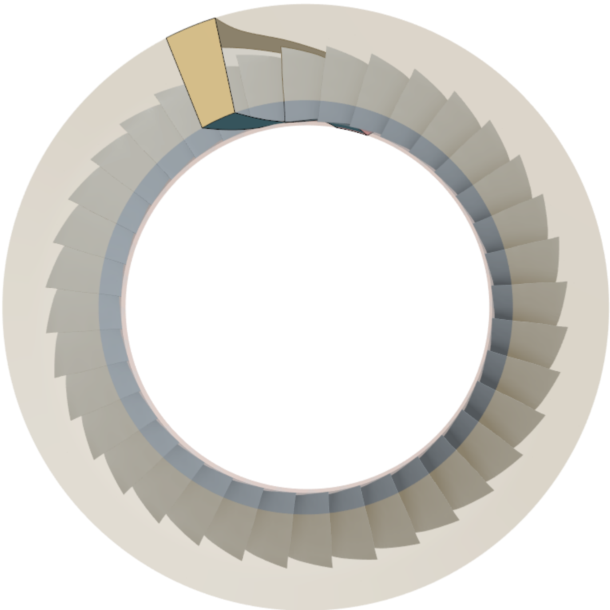

Figure 3.1.1: Front view of the ROTOR 37 CAD model

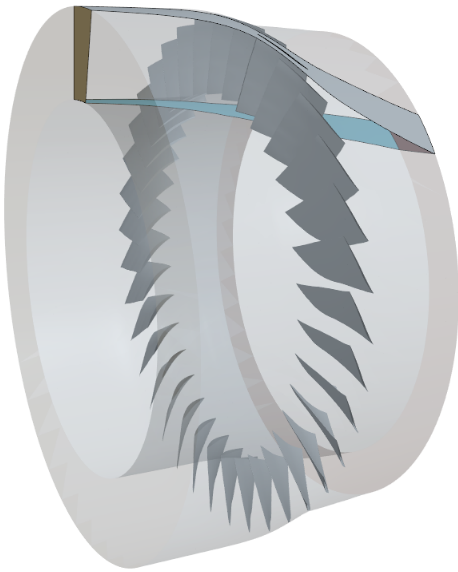

Figure 3.1.2: Lateral view of the ROTOR 37 CAD model

As a previously explained, for a reduction of the CFD computational effort the compressor domain is dived into 1 of the 36 blades that the NASA ROTOR 37 model has. Therefore the computational domain of the CFD model will consist of a single passage of the compressor, the periodic interference will be established between the two walls on the rotational direction (setting up periodic flow fields). The computational domain will consist of 8 surfaces: the Inlet, the Outlet, the Hub, the Shroud, 2 lateral walls (Periodic Interface) and 2 Blade surfaces (Extrados and Intrados), all of them depicted in Figure 3.1.3. The Shroud and the Hub will be rigid walls as the Blade surfaces, whereas the Inlet and Outlet will be crossed by the flow.

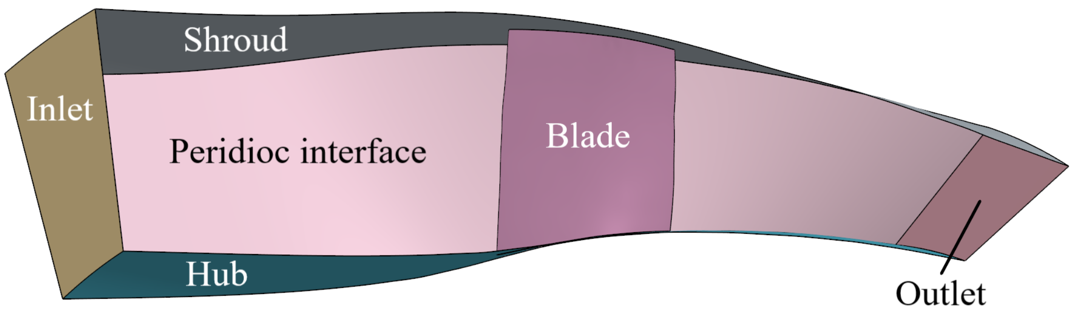

Figure 3.1.3: Computational domain (Single passage of the ROTOR 37 model)

The geometrical model has been provided by [12], this 3D model represents with a high fidelity the geometry of the NASA axial compressor. The lateral walls (Periodic interference) are streamline shaped, so that the domain contains a high percentage of the streamlines. Sufficient distance has been left between the Inlet and the Blade to make sure that the flow fully develops and between the Blade and the Outlet to keep the wake inside the domain.

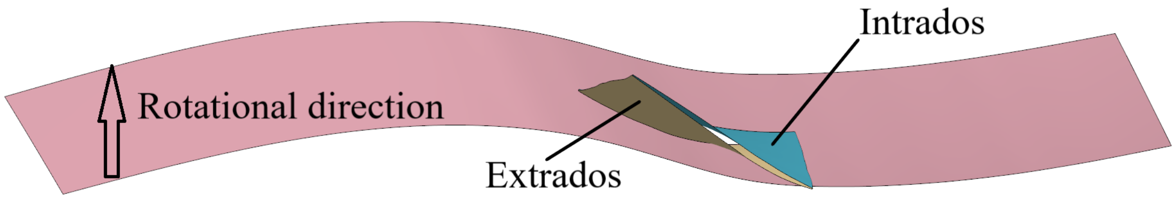

Figure 3.1.4: Blade Extrados and Intrados identification

Finally on Figure 3.1.4 the direction of rotation of the axial compressor is depicted. The Extrados and Intrados faces are therefore known and showed in the figure, they will be important for the future analysis of different coefficients above the blade.

3.1.2 Mesh model

The mesh strategy used in the CFD simulation is unstructured. The choice of the mesh has been done following the conclusions of Segarra's articles [14]. On this document the author concludes that the unstructured mesh results are more precise to the experimental data of NASA ROTOR-37. Succeeding with Segarra's work, the unstructured mesh used in this project contains 1.53 million elements. This base size is employed due to the high accuracy of the results and mesh independence achieved in [14]. Furthermore, base size and wall refinement is used among the domain to enclose huge pressure gradients among the domain due to shear effects.

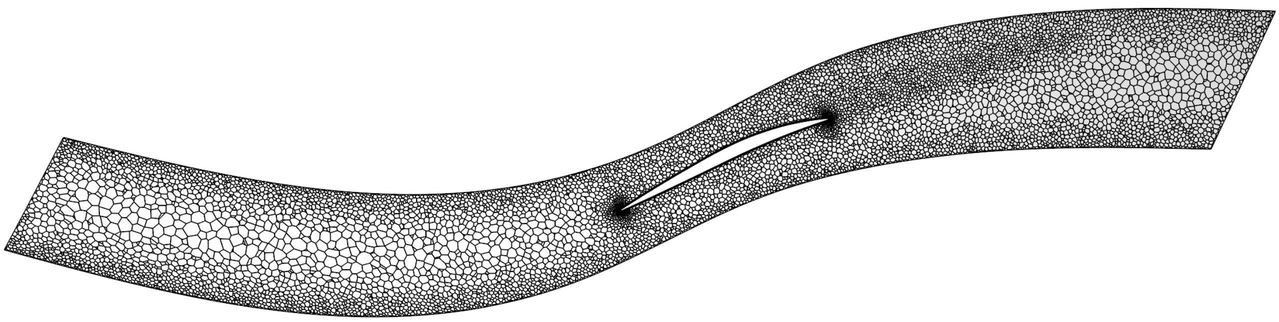

Figure 3.1.5: Mesh section display at 50% of the span

On Figure 3.1.5 the mesh at the 50% of the span is depicted. The base size of the grid is 0.018m, which corresponds to 3% of the rotor mean chord. This size has been chose since it presents a good trade-off between the accuracy of the mesh and the computational effort. The volume-growth rate is set to 1.15, whereas the surface growth rate is set to be 1.35 for a good quality of the mesh. Other details include a target surface size of 0.0012m and a minimum surface size of 10% of the base size.

Several local refinements have been done in order to achieve a higher accuracy in the results. Subsequently the base size of the wake is shown in Figure 3.1.6 to be smaller, a local refinement is used to enclose the pressure gradients produced by the wake. The base size on the wake is reduced to 25% of the global base size to capture the turbulent wake. Furthermore, on the leading and trailing edge, the cell size has been reduced to 5.4E-5 m, to capture the curvature of this sharp edges.

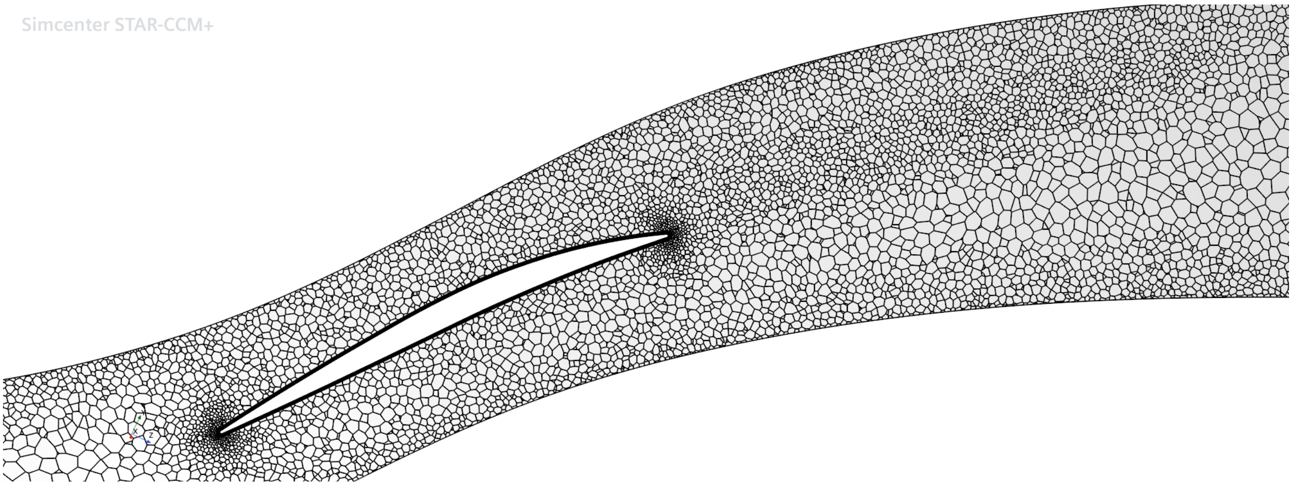

Figure 3.1.6: Zoom view at 50% of the span mesh section display

On the lateral walls where the periodic interference takes place the size of the surface mesh elements is also reduced to 35% of the global base size, for a higher fidelity. On the blade a surface mesh of 50% of the global base size is implemented. Whereas the hub and shroud surface meshes have a 200% and 25% of the global base size respectively.

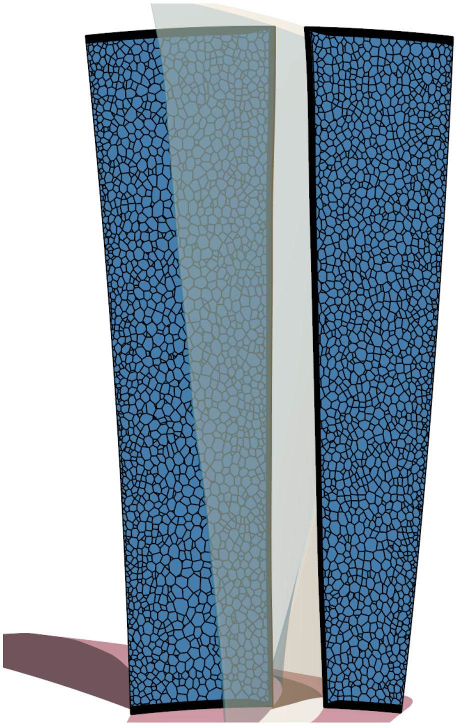

Figure 3.1.7: Front view of the mesh on the blade

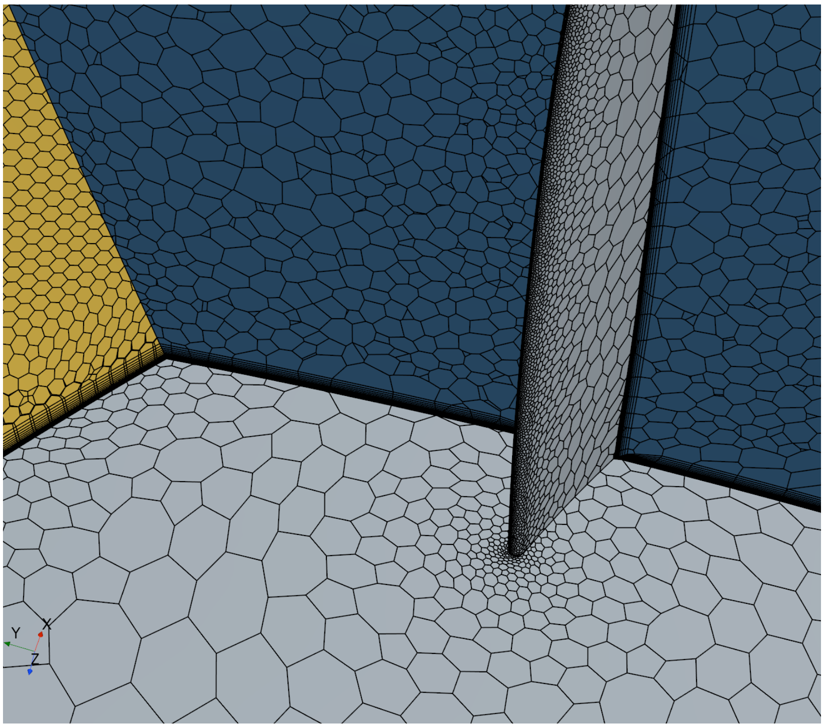

Figure 3.1.8: Zoomed view of the mesh on the hub and blade intersection

Furthermore, a prism layer is added in the hub, shroud and the blade surfaces, in order to precisely compute the boundary layer generated over this rigid walls. The prism layer is defined through three parameters: an element size of 7.2E-4 m, 13 number of element layers and a stretching factor of 1.25. The objective of this parameters id to ensure a gradual transition from polyhedral to cubic cells, while achieving the lowest values of y^+. The distribution of prism layer and the mesh refinement on the leading edge can be seen in Figure 3.1.7 and Figure 3.1.8.

3.1.3 Derived parts

To show the results and mesh parts a series of surfaces and points have been developed to show and plot the data. The computational domain has been parameterized in order to obtain this planes for a better understanding of the results.

The span-wise planes correspond to the a series of planes at a relative distance between the hub and the shroud. To compute these surfaces the domain is parameterized, the planes at 10%, 50%, 70% and 90% of the rotor span are used for further comparisons, see Figure 3.1.9.

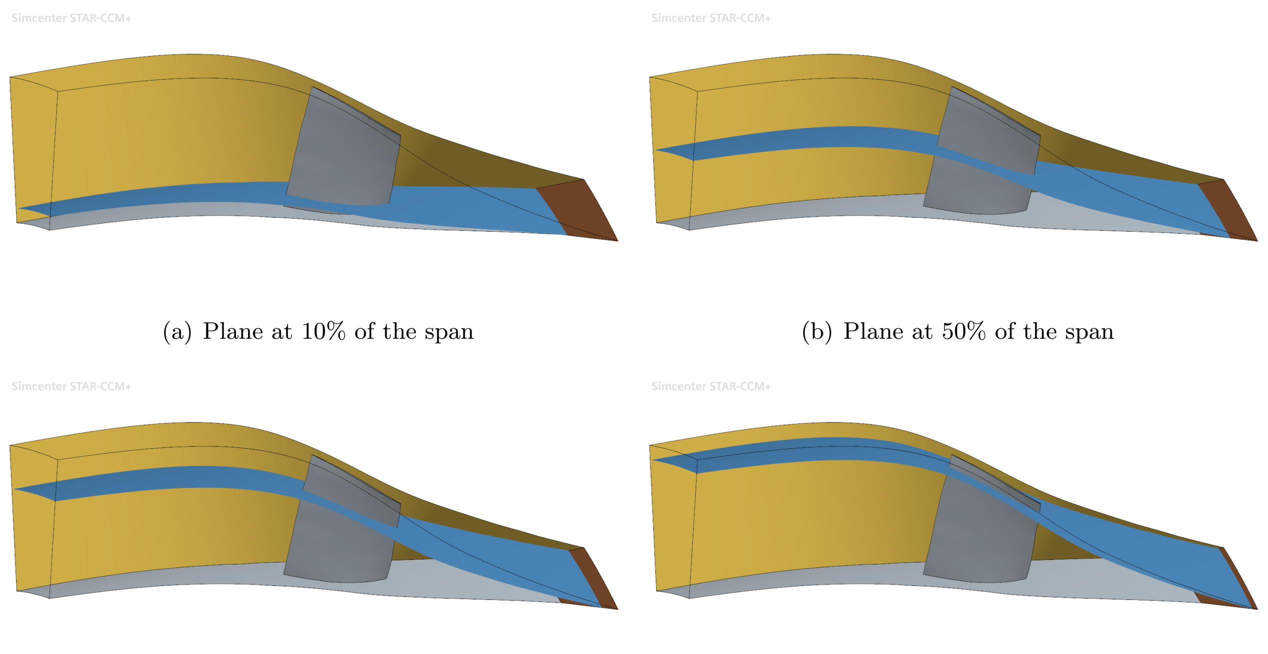

(a) Plane at 10% of the span

(b) Plane at 50% of the span

(c) Plane at 70% of the span

(d) Plane at 90% of the span

Figure 3.1.9: Span wise planes

The Meridional plane correspond to a plane at the same distance between the Extrados and the Intrados of two contiguous blades. To compute this surface a function in STAR CMM+ is used to compute the plane at the same distance between the contiguous blades inside the computational domain, see Figure 3.1.10.

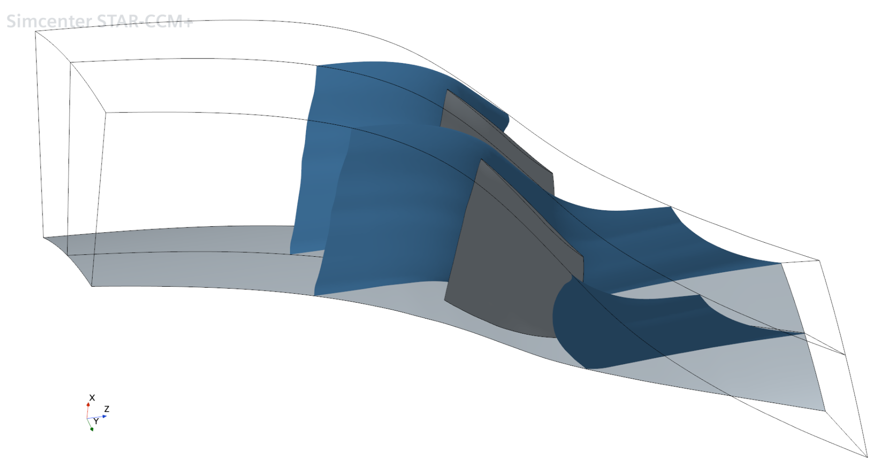

Figure 3.1.10: Meridional plane

Furthermore, the adimensional plane and point are computed at a one chord distance upstream of the leading edge. The flow properties will be evaluated here to obtain the adimensional pressure, density and velocity, needed to adimensionalized certain coefficients used in future sections, see Figure 3.1.11 and Figure 3.1.12.

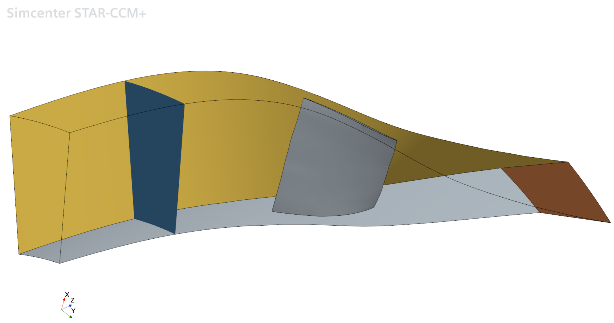

Figure 3.1.11: Adimensional plane

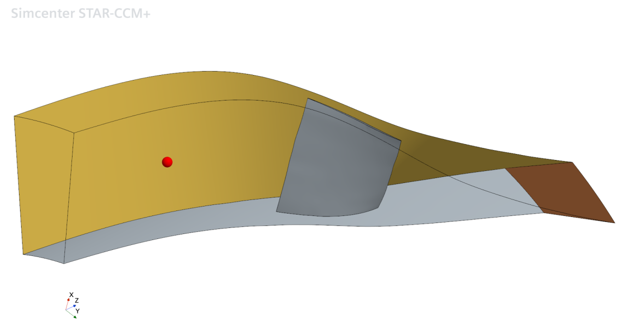

Figure 3.1.12: Adimensional point

Finally a set of cross-channel planes are computed in Figure 3.1.13. The purpose of the two of the two first planes is to serve a section for comparisons against the experimental results from NASA ROTOR 37. Station 1a and 3 have been already depicted in Figure 2.3.5. Note that Station 1a is 5% the chord distance upstream of the leading edge, whereas Station 3 is a normal plane, parallel to the inlet, immediately downstream of the blade. The third plane is computed at the middle of the blade with mesh visualization purposes.

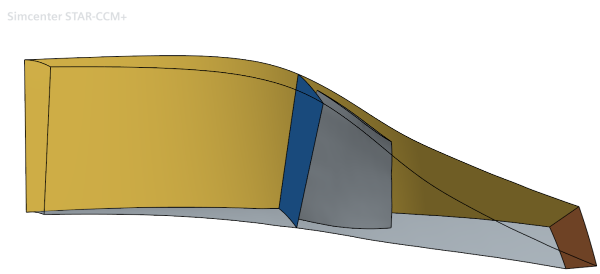

(a) Cross-channel plane at Station 1a

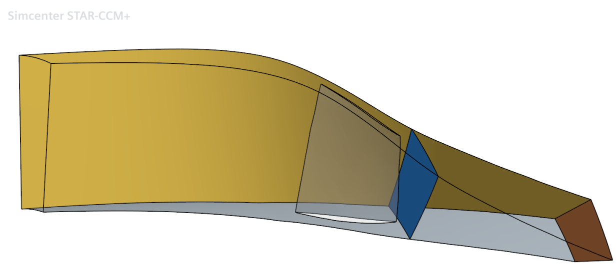

(b) Cross-channel plane at Station 3

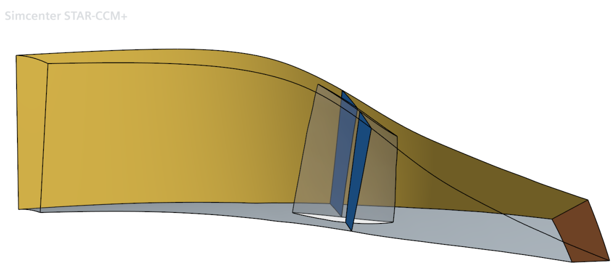

(c) Cross-channel plane at middle of the blade

Figure 3.1.13: Cross-channel planes

3.2 Setup: computational domain and boundary conditions

3.2.1 Model selection

The problem can be considered as steady, the domain will rotate at a constant speed of 1800 rad/s. Therefore, in the CFD simulation a moving reference frame is established in the axial direction. The domain will be 3D and axisymmetrical as established in subsubsection 3.1.1. In order to solve the problem, a pressure-based, coupled equation method is used to solve the Reynolds-Averaged-Navier-Stokes (RANS) equations. The flow is assumed turbulent, as seen on the Reynolds number computed on Equation 12, which correspond to the 50% span, taking the mean chord of the blade. This turbulence is modeled using a k – omega (k - ω) shear-stress-transport (SST) model. The SST model is used due to the huge accuracy on the boundary layer computation for turbomachinery cases.

$$Re_c = \frac{c \cdot U \cdot \rho}{\mu} = \frac{0.0555\ [m] \cdot 425.4\ [m/s] \cdot 1.085\ [kg/m^3]}{1.855 \cdot 10^{-}5\ [Pa \cdot s]} = 1.381 \cdot 10^6 \tag{12}$$

The Gamma ReTheta Transition model is implemented due to it's capacity to determine the turbulence intermittency and the transition momentum thickness Reynolds number. This model is able to predict the start of the transition from a turbulent to a laminar boundary layer.

3.2.2 Boundary conditions

As previously mentioned during the work four different cases with the same corrected mass flow, but decreasing pressure of operation are computed. All the cases will target a corrected mass flow of 20.2 kg/s. Regarding the boundary conditions, the inlet is established as a mass flow inlet boundary, whereas the outlet is established as a pressure outlet. The purpose of this election is to establish a certain mass flow rate, for which it's corrected mass flow will be the target one when the inlet pressure equals the pressure of operation of the case. This mass flow rate is computed with the corrected mass flow rate reordered formula shown in Equation 13. The purpose is to vary the outlet pressure until the inlet pressure equals the target one for the given case, and therefore the corrected mass flow will be the targeted (20.2 kg/s). This iterative process of the pressure outlet value is manually changed in the simulation once convergence is obtained, seeking for simplicity.

$$\dot{m} = \dot{m}_c \cdot \frac{\delta}{\sqrt{\theta}} = \dot{m}_c \cdot \frac{\frac{P}{P_{ref}}}{\sqrt{\frac{T}{T_{ref}}}} = 20.2\ [kg/s] \cdot \frac{\frac{P_{op}(kPa)}{101.325\ kPa}}{\sqrt{\frac{288.15\ K}{273.15\ K}}} = 0.18898 \cdot P_{op}\ \ [kg/s] \tag{13}$$

Where the reference pressure and temperature are set to be: $T_{ref} = 273.15\ K,\ \ P_{ref} = 1\ atm$. P_{op} should be introduced using kPa units. The boundary values used on the inlet and outlet, including pressure, temperature, and turbulence parameters are tabulated in the following Table 3.2.1. The inlet and outlet temperature will be the same for all the cases, as well as the turbulence parameters.

	Case 1 (100 kPa)	**Case 2 (40 kPa)**	**Case 3 (10 kPa)**	**Case 4 (4 kPa)**
Inlet mass flow, $\dot{m}\ [Kg/s]$	0.54631	0.21853	0.05463	0.02185
Inlet temperature, $T_{in}\ [K]$	288.15	288.15	288.15	288.15
Outlet pressure, $P_{out}\ [Pa]$	126680	49545	11300	4190
Outlet temperature, $T_{out}\ [K]$	300	300	300	300
Turbulence intensity, $[-]$	0.01	0.01	0.01	0.01
Turbulence viscosity ratio, $[-]$	10	10	10	10

Table 3.2.1: Summary of the boundary conditions values for each case

The converged corrected mass flow rate is assumed to have an error due to the manual iterative process followed. Therefore, Table 3.2.2 shows the converged corrected mass flow rate and the numerical error absolute and relative to the targeted corrected mass flow rate. This errors are computed according to the Equation 14 and Equation 15.

	Case 1 (100 kPa)	Case 2 (40 kPa)	Case 3 (10 kPa)	Case 4 (4 kPa)
Corrected mass flow rate, $\dot{m}_c$ $[kg/s]$	20.191	20.199	20.243	20.205
Absolute error, $ABS.\ ERR.$ $[kg/s]$	0.009	0.001	0.043	0.005
Relative error, $REL.\ ERR.$ [-]	0.045%	0.005%	0.213%	0.025%

Table 3.2.2: Relative and absolute error to the targeted corrected mass flow rate

$$Error_{abs} = |\dot{m}_{c,CFD} - \dot{m}_{c,target}| \tag{14}$$

$$Error_{rel} = \frac{|\dot{m}_{c,CFD} - \dot{m}_{c,target}|}{\dot{m}_{c,target}} \tag{15}$$

As the table above shows both kind of errors are minimal. The maximum relative error represents just a 0.243% and is achieved in the case 3. Therefore, the simulations corrected mass flow can be assumed to be the same for the four cases, despite the small errors.

3.2.3 Initialization techniques

To initialize the simulation, seeking for a rapid convergence the pressure data is tabulated from a previously converged case and used in the initialization of an not converged case. The data is first tabulated from the converged case and conditioned in accordance with the operational pressure ratio between the converged and not converged case, as see in Equation 16. Once extracted from the case, the data file is imported to the not converged case where is used for the initialization. The imported approximated case serve to a more quicker converge rate, reducing the computational effort for each of the simulated cases.

$$P_{ini}\left[x,y,z\right] = P_o\left[x,y,z\right] \cdot \frac{P_{op,ini}}{P_{op,o}} \tag{16}$$

Where $P_o[x,y,z]$ corresponds to the pressure of the converged case in the hole domain, $P_{ini}[x,y,z]$ is the pressure on the domain which will be used in the initialization and $P_{op,x}$ matches the pressure of operation of the given case.

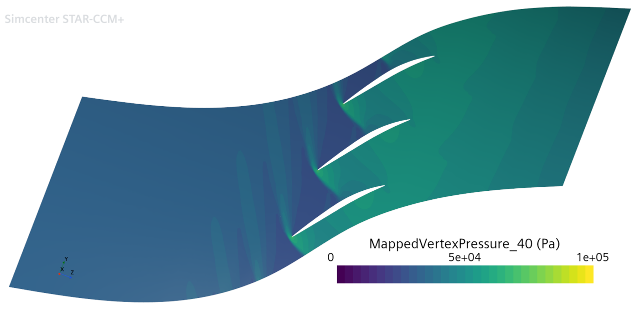

Figure 3.2.1: Initialized (Not converged) pressure on the 50% span

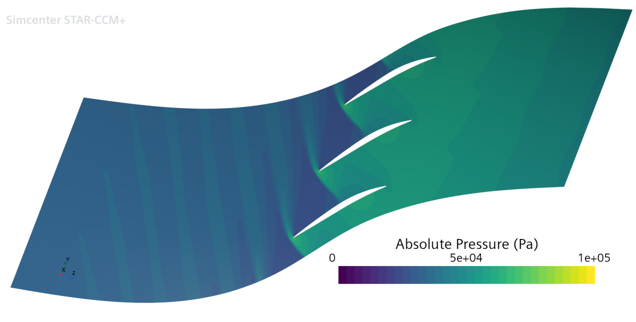

Figure 3.2.2: Converged pressure on the 50% span

Figure 3.2.1 is obtained with the data of the closest case (Case 3, 10 kPa), the plotted pressure has been conditioned and imported to the Case 2 (40 kPa). Once the case is converged the Figure 3.2.2 is obtained. To compare both pressure maps, the pressure is plotted in the 50% span plane, since it is the most representative because it illustrates the average field. The differences between the initialized model and the converged one seems minimal, on both figures. The only visible effect appears on the shock waves angle and length, which is different for the different cases as it will be shown in future chapter. 5000 less iterations are estimated to be required for complete converge of the case from the starting not converged point.

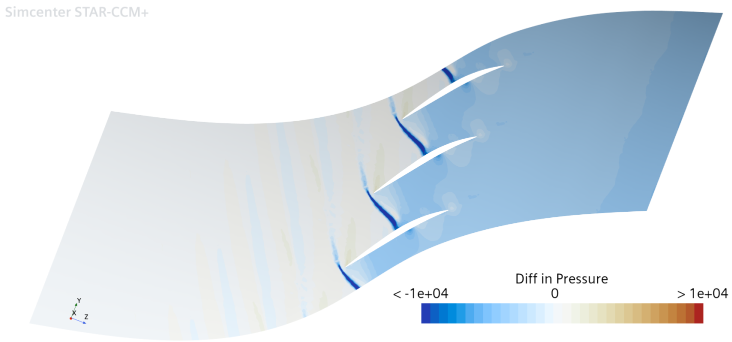

Figure 3.2.3: Differences between the not converged and converged pressure at 50% of the span

The differences between the initialized data minus the converged is shown in Figure 3.2.3.This figure bring insight on the main differences between the converged and not converged pressure maps. As already mentioned, the shock waves show an angular displacement and a higher pressure in the converged case. The back pressure of the initialized model is lower, some other minor effects are regarded in the airfoil boundary layer. Note that the highest differences in the color bar are of 10000 Pa, which correspond of a 25% relative difference with respect to pressure of operation. This maximum difference is only found in the shock wave and drop to 12.5% for the back-pressure, denoting small errors between both models.

The usage of this technique initializes the model with a reliable and accurate pressure map, similar to the converged case. This technique has therefore demonstrated a huge decrease on the computational effort, and a secure initialization to achieve convergence.

4 Results and discussion

During the results discussion a specif order will be followed, starting with the discussion of the global parameters across the cases. Continuing with the local effects and the flow coefficient effects on the compressor performance and ending with the pressure losses and the experimental results comparison.

4.1 Global parameters

Reducing the operational pressure in the system, consequently results in a decreased drag. However, this reduction is often related with a lower compressor performance and higher demand of energy to achieve this pressure in the tube. Since currently their is no possibility to completely simulate the Hyperloop system, the aim of this study is to analyze the compressor limitations at low pressures of operation. The approach followed in this work, ensures similar incidence angles by achieving the same corrected mass flow rates in the different cases.

$$Drag = \frac{1}{2} \cdot A \cdot \rho \cdot U^2 \cdot C_d = \frac{1}{2} \cdot \frac{P_{op}}{R \cdot T} \cdot A \cdot U^2 \cdot C_d \tag{17}$$

Based on the literature review, to study the low pressure effects and compare them to the cases simulated by Galindo et al. [13], a 100 kPa (ambient pressure), 10 kPa and 4 kPa cases are computed. Additionally a 40 kPa case is evaluated to ensure a smaller step between the 100 kPa a 10 kPa cases.

$$Re_c = \frac{c \cdot U \cdot \rho}{\mu} = \frac{c \cdot U \cdot P}{\mu \cdot R \cdot T}\ , \quad (c = 0.0555\ m) \tag{18}$$

$$\dot{m}_c = \dot{m} \cdot \frac{\sqrt{\theta}}{\delta} = \dot{m} \cdot \frac{\sqrt{\frac{T}{T_{ref}}}}{\frac{P}{P_{ref}}}\ , \quad (T_{ref} = 273.15\ K, \quad P_{ref} = 1\ atm) \tag{19}$$

$$\pi_c = \frac{P_{t,out}}{P_{t,in}} \tag{20}$$

$$\eta = \frac{\pi_c^{\frac{\gamma-1}{\gamma}} - 1}{\frac{T_{t,out}}{T_{t,in}} - 1} \tag{21}$$

	Case 1 (100 kPa)	Case 2 (40 kPa)	Case 3 (10 kPa)	Case 4 (4 kPa)
Reynolds number, Re_c	1,379,700	551,568	137,190	54,827
Corrected mass flow, $\dot{m}_c$ [m/s]	20.191	20.199	20.243	20.205
Pressure ratio, π_c	2.1127	2.0769	1.9499	1.8825
Rotor efficiency, η_r	0.8328	0.8266	0.8075	0.7823

Table 4.1.1: Summary of the compressor global parameters

Table 4.1.1 has been obtained following the definitions on: Equation 18, Equation 19, Equation 20 and Equation 21. Is evident that the differences between the cases 1 and 2 are relatively smaller than between case 2 and 3, and cases 3 and 4. As the operational pressure decreases, so does the efficiency and therefore the pressure ratio. Is important to note that this axial rotor hasn't been optimized for low pressure conditions.

Regarding the pressure ratio, π_c, the operational pressure decrease from 100 kPa to 40 kPa supposes an small jump on this parameter, just 1.71%. This percentage goes up to 6.31% between 40 kPa and 10 kPa, and decreases a bit to 3.52% between 10 kPa and 4 kPa. This similarity between the first cases and discrepancy between the three others, as expected on the literature, could occur due to the flow separation of the blades at small Reynolds numbers. This hypothesis will subsequently discussed on the flow patterns of the different cases.

The rotor efficiency, η_r, shows a similar trend to the one depicted by the pressure ratio. The efficiency between the both first cases (100 kPa and 40 kPa) is minimal, just a 0.75%. Similarly this gap increases between 40 kPa and 10 kPa to a 2.34%, probably due to the flow separation. However, the decrease is even higher between 10 kPa and 4 kPa, where the percentage is 3.17%. This further decrease for the lowest pressures of operation could probably be reasoned with an increase of secondary losses, such as the tip leakage.

4.2 Local effects

In order to reinforce these ideas, a complete analysis of the local effects have been conducted, including the flow patterns and their differences among the cases. For several spans sections (10%, 50% and 90% spanwise planes), the relative Mach number, pressure coefficient, friction coefficient and intermittency have been studied. Nevertheless, since not all the sections provide relevant and unique information, a special focus has been given to the rotor 50% spanwise plane. Since this plane represents the mean flow, the local effects displayed on them have a big importance on the analysis.

4.2.1 Flow patterns

In this section the results of the simulations are assessed focusing in the impact of the pressure reduction and consequent decreases in Reynolds number effects. Especially the patterns on the relative Mach number fields are the study purpose of this section. To aim for brevity some of the figures are omitted and included in Appendix A.

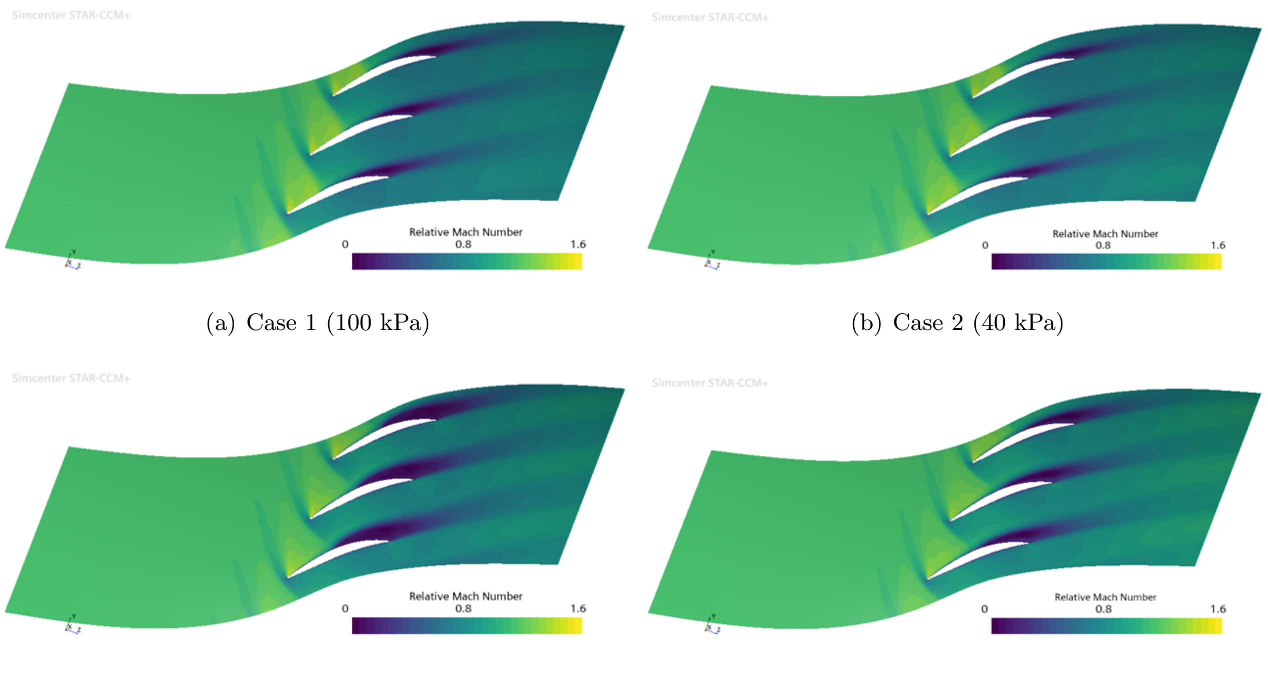

(a) Case 1 (100 kPa)

(b) Case 2 (40 kPa)

(c) Case 3 (10 kPa)

(d) Case 4 (4 kPa)

Figure 4.2.1: Relative Mach on 10% span

Figure 4.2.1 shows the relative Mach number for the 10% span plane. As already shown in the global parameters, cases 1 and 2 are nearly identical, the shock wave position and the blade wake are indistinguishable. On contrary, the breadth and length of the wake grows for case 3, where it's the biggest, and case 4. On this two cases the flow exhibits a larger separation in the suction face of the blade. Similarly, case 3 and 4 shock angle differs from the first case, being moved towards the trailing edge (lower shock angle). The shock-shape also changes in case 3 and 4, evolving from a straight shock to a more curved bow-shock type.

As a consequence of the low operational pressure flow detachment and boundary layer thickening appear. This effect enhance the partial choke of the passage, decreasing the performance of the axial rotor. Also, the leading edge shock wave gradient is weaker on cases 3 and 4, causing higher velocities inside the passage. Furthermore, the cases with lower operational pressures, show higher relative Mach numbers at the output, which denote lower pressure ratio as it has already been mentioned in subsection 4.1.

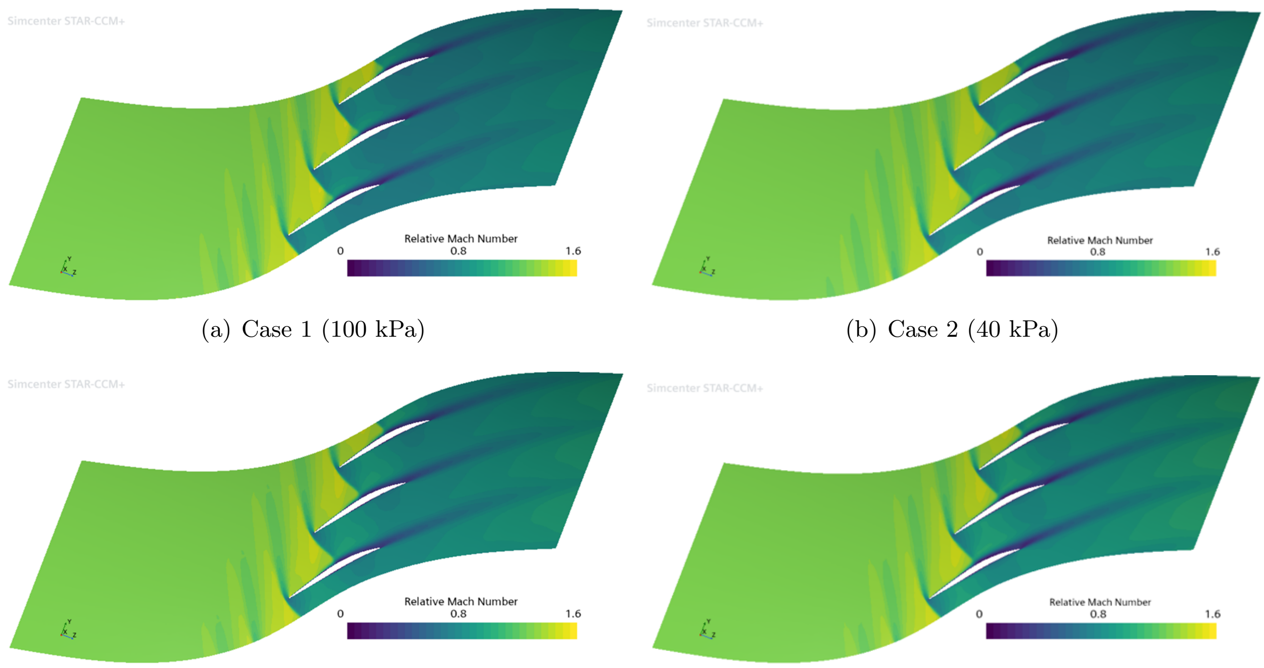

(a) Case 1 (100 kPa)
(b) Case 2 (40 kPa)
(c) Case 3 (10 kPa)
(d) Case 4 (4 kPa)

Figure 4.2.2: Relative Mach on 50% span

Figure 4.2.2 shows the relative Mach number for the 50% span plane. This plane represents the average flow behavior, being of great importance for the analysis. Similarly to the 10% span figures, cases 1 and 2 doesn't represent big differences with the exception of the wake. Which is more breadth in the second case. Cases 3 and 4, again diverge slightly in the angle and shape of the shock wave. However, the wake for case 3 is relatively smaller, but bigger for case 4 with respect to the first case. The relative Mach number at the exit are again bigger for lower operational pressures.

Figure 4.2.3 shows the relative Mach number for the 90% span plane. Similar effects are appreciated in this figure with respect to the already mentioned. On this plane the shock waves become stronger, whereas the variations between the models are less appreciable. This span section the tip clearance effects, detailed on further sections, become more important.

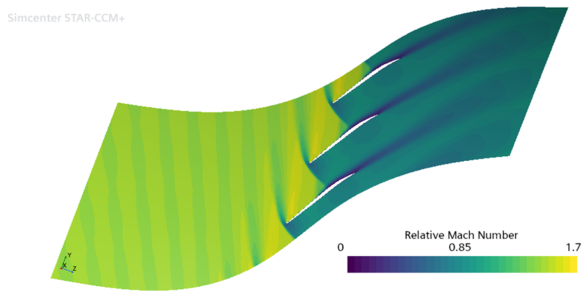

(a) Case 1 (100 kPa)

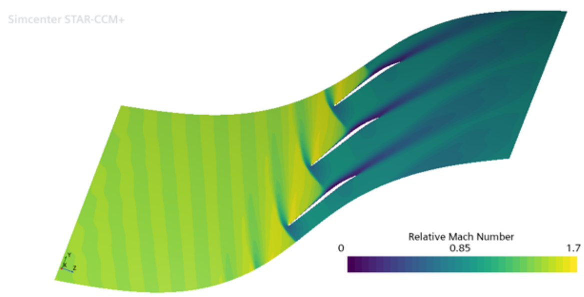

(b) Case 2 (40 kPa)

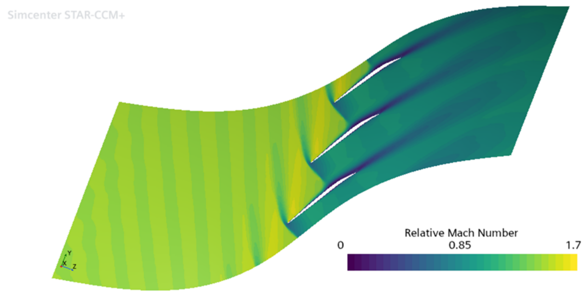

(c) Case 3 (10 kPa)

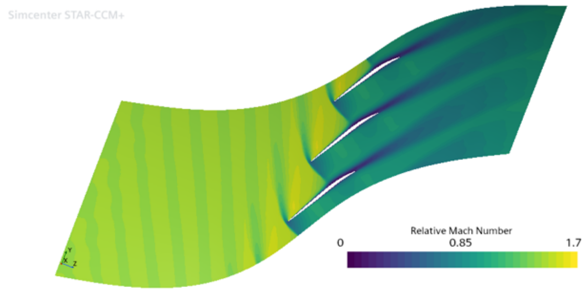

(d) Case 4 (4 kPa)

Figure 4.2.3: Relative Mach on 90% span

Figure 4.2.4 shows the relative Mach number at the meridional plane between the blades. First of all, a zone with lower relative Mach number can be observed in the lower left corner due to the boundary layer thickening of the rotor hub. The effect of the shock of the adjacent blade is observed on the left, before the main shock. Furthermore, the meridional plane shows the effect of the tip clearance at the right top of the passage. The high-pressure flow from the pressure face try to cross the tip clearance gap circulating towards the suction face.

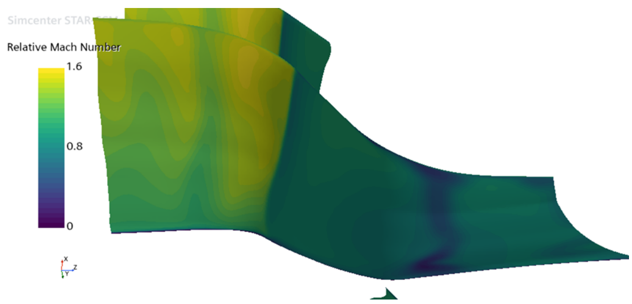

(a) Case 1 (100 kPa)

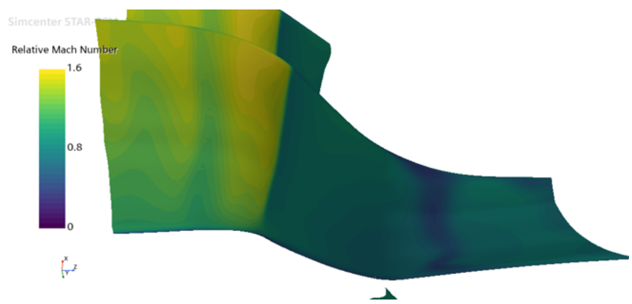

(b) Case 2 (40 kPa)

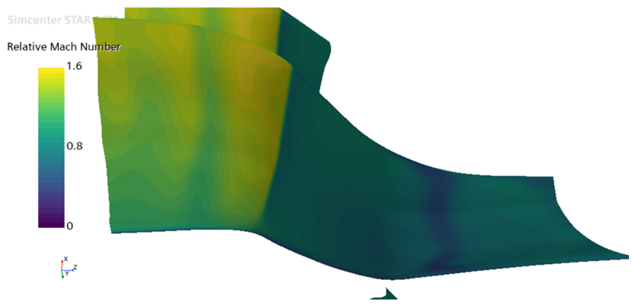

(c) Case 3 (10 kPa)

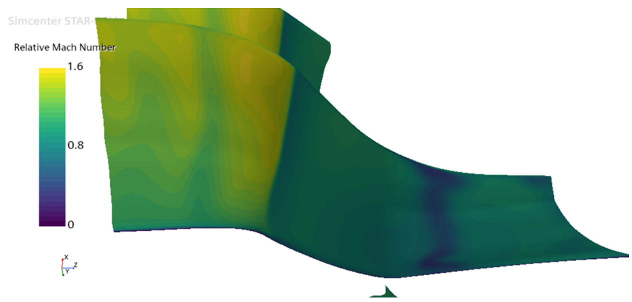

(d) Case 4 (4 kPa)

Figure 4.2.4: Relative Mach on meridional plane

Furthermore, the differences between the meridional plane models serve to bring greater insight. Despite, the repeated trends, the spanwise variation of the shock wave varies evidently between models. The wake produced by the blade is also illustrated to increase while the operational pressure decreases, although this variation change on the span. The tip clearance effect on the wake is also appreciated downstream the wake, becoming more present for lower pressure cases.

Table 4.2.1 show the differences in the flow angle. The flow angle is illustrated and not the metal one, because the metal flow angle is constant. Therefore, for the seek of comparison, the differences on the incidence angle equals the flow angle ones. Shows Equation 22 the calculation of the incidence angle, i, and the velocity components involved in the flow angle calculation, β_{flow}.

$$i = \beta_{flow} - \beta_{metal} = \arctan\left(\frac{V_{tg}}{V_{ax}}\right) - \beta_{metal} \tag{22}$$

Is essential to have similar angles of incidence to achieve a correct comparison between cases. The flow angle in calculated both at point at 50% of the rotor span and one chord distance upstream of the leading edge, and at a cross-channel plane also one chord distance upstream of the leading edge. Both values are compared to avoid possible effects of the shock waves in the evaluations. The differences in flow angles on the table result minimal, accounting for a 0.48% difference on the point and 0.52% on the plane. The highest discrepancy is given between cases 2 and 3, and could be reasoned by the mass flow differences.

Flow angle, β_{flow} [º]	**Case 1 (100 kPa)**	**Case 2 (40 kPa)**	**Case 3 (10 kPa)**	**Case 4 (4 kPa)**
On a point	66.86	66.95	66.63	66.85
Averaged on the plane	66.94	67.06	66.71	66.9

Table 4.2.1: Flow angle for all the cases

4.2.2 Differences between the models

In order to get a clear image of the differences between the models, the differences in relative Mach number are computed. For this purpose, case 1, of 100 kPa, is used as the reference case to get compared between the rest of the models. The differences are obtained by subtracting to the relative Mach number of case 1, the one in case 2, 3 or 4 (40 kPa, 10 kPa or 4 kPa). In the color bar of Figure 4.2.5, Figure 4.2.8, Figure 4.2.9, Figure 4.2.10..., blue tones will correspond to a lower relative Mach in case 1 and a red color to higher relative Mach. Always case 1 is being compared to the other cases. Is also important to note that figures are clipped and therefore, the color bar is not representative of the real maximum or minimum but only of the zones where differences appear with more or less intensity.

$$RM_{diff} = RM_{100\ kPa} - RM_{x\ kPa} \tag{23}$$

All the rest other possible combinations of differences and extra local effect figures are displayed in Appendix A.

Figure 4.2.5 shows the relative Mach number differences taking case 1 as reference in the 10% span plane. The differences between cases 1 and 2 are slight, the breadth and length of the wake are smaller in case 2, since the relative Mach is higher in a part of the wake region. Cases 1 and 3 so a great differences in the wake, which hugely increases for case 2. Furthermore, the shock waves are curved backwards as shown by the blue colors on it and the passage shows higher relative velocities for case 3. On the suction side near the leading edge and the middle of the pressure side of the blade the boundary layer is thicker in case 3. Finally case 1 and 4 show similarities to the previous comparison, the shock waves are tilted backwards in case 4, the passage speed is even higher for this case and the boundary layer is even thicker. However, the breadth is higher in case 4, but not as much as in case 3.

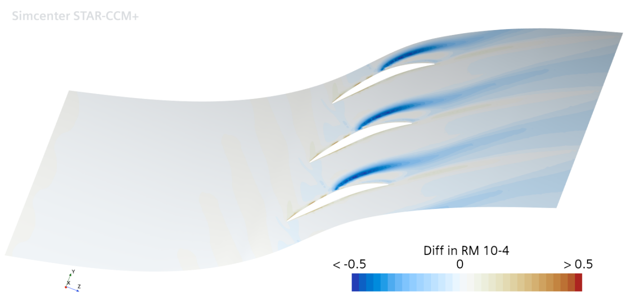

(a) Case 1 and 2 (100 kPa and 40 kPa)

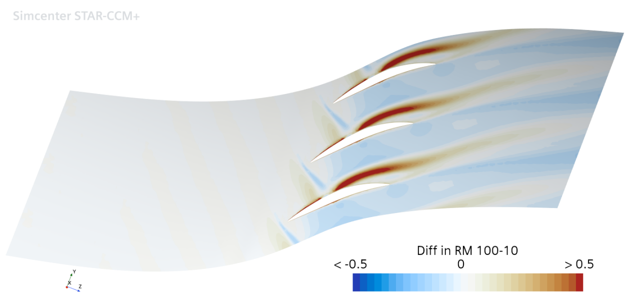

(b) Case 1 and 3 (100 kPa and 10 kPa)

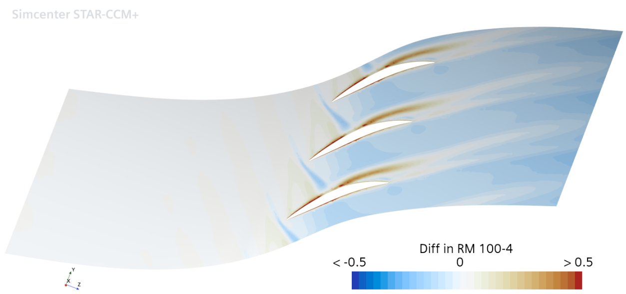

(c) Case 1 and 4 (100 kPa and 4 kPa)

Figure 4.2.5: Relative Mach differences on 10% span

Figure 4.2.8, Figure 4.2.6 and Figure 4.2.7 shows the relative Mach number differences taking case 1 as reference in the 50% span plane. The greater size of the figure account for the importance in the analysis due to its characteristic resemblance to the mean flow.

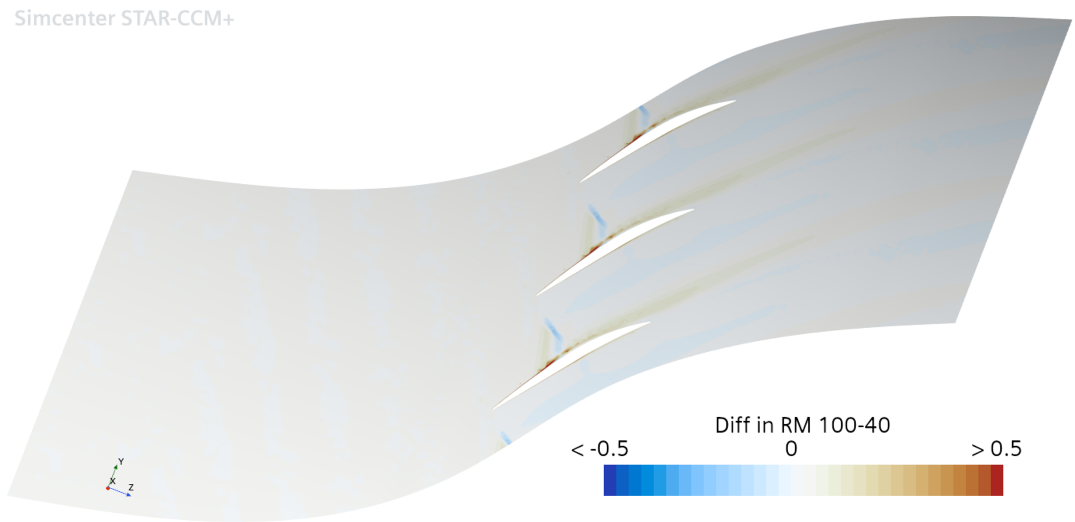

Figure 4.2.6: Relative Mach differences on 50% span, Case 1 and 2 (100 kPa and 40 kPa)

Figure 4.2.8 compares cases 1 and 2. The similarity between both simulations is evident. However minimal differences are appreciated in the shock wave position, tilted backwards, and in the wake, which becomes wider in the 40 kPa case. The boundary layer is specially thicker in the suction side of case 2, producing a earlier detachment of the flow which contributes to the breadth of the wake. The velocity of in the passage of the second case is slightly bigger.

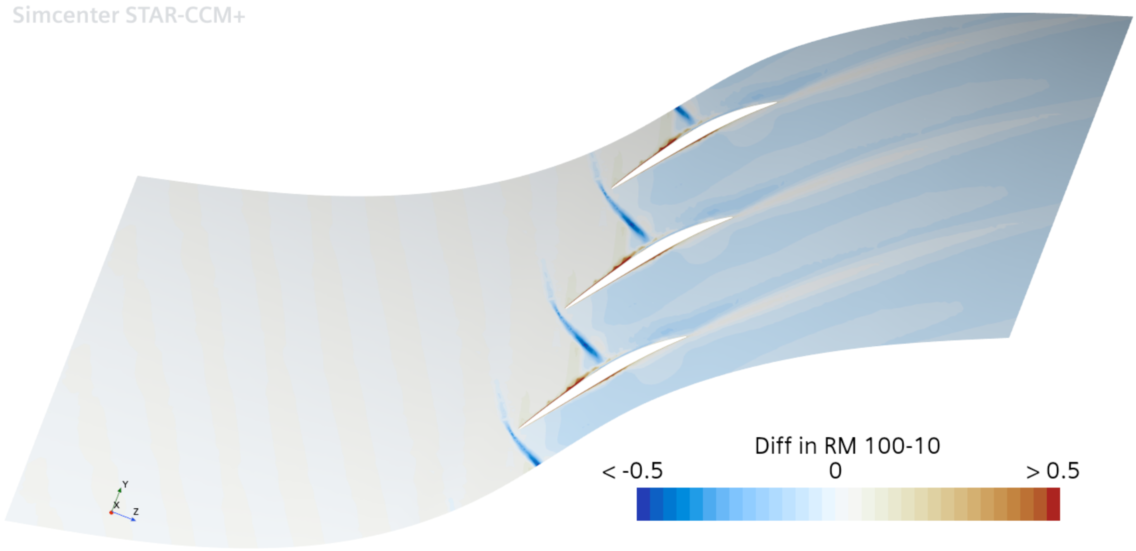

Figure 4.2.7: Relative Mach differences on 50% span, Case 1 and 3 (100 kPa and 10 kPa)

Figure 4.2.8 compares cases 1 and 3. Differences are widely appreciable between this models, consolidating the big step hypothesis between this two models seen in the global parameters comparison. First of all, the shock wave is even more backwards displaced, getting the mentioned bow shock shape. The boundary layer due to its laminar nature (less energetic) becomes wider at the beginning of the suction side and on the middle of the pressure side. The wake detaches earlier, closer to the leading edge, in the first case. The wake length is also, slightly smaller in case 2. These effects on the wake could be a consequence of the weaker shock waves and therefore, higher passage velocities achieved for lower pressures.

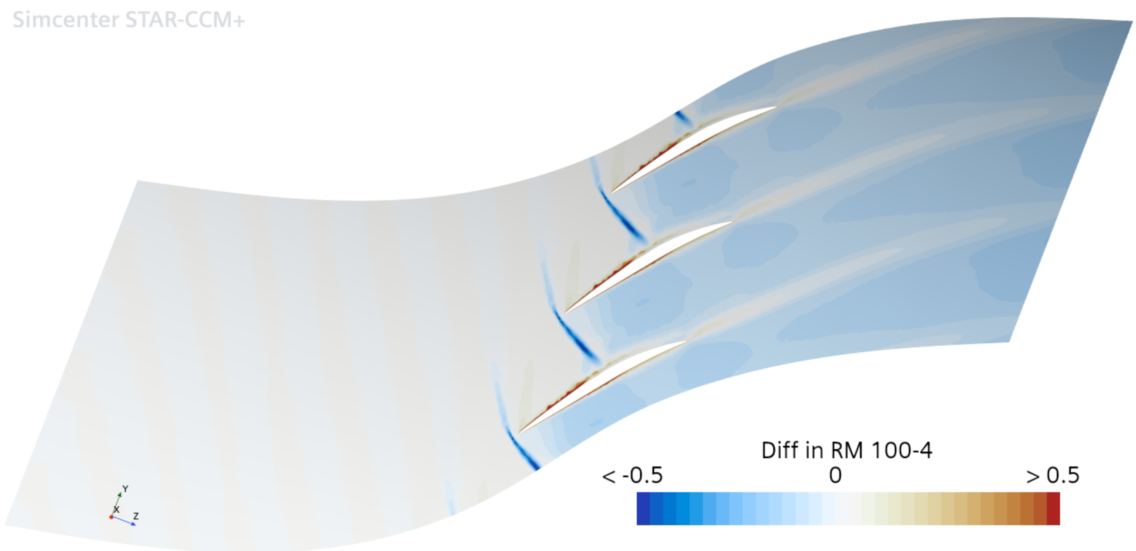

Figure 4.2.8: Relative Mach differences on 50% span, Case 1 and 4 (100 kPa and 4 kPa)

Figure 4.2.7 compares cases 1 and 4. The differences commented in the previous image, become even more noticeable in this figure. The boundary layer increases in thickness specially at the beginning of the suction face. The shock wave is similarly displaced, as in the previous figure. Whereas, the wake is more intense in the fourth case, the relative mach number is lower immediately behind the trailing edge, despite the lower length presented. The flow detachment is more violent in the 4 kPa case after the shock wave, producing a higher passage velocity and partial choking.

Figure 4.2.9 shows the relative Mach number differences taking case 1 as reference in the 90% span plane. This section further emphasizes the changes already mentioned. The differences from case 1 and 2, become less noticeable and is only the thicker boundary layer of the suction side in case 2, the only noticeable effect. When lowering more the operational pressure the relative Mach number effects become more similar. Therefore the differences between cases 1 and 3 and cases 1 and 4 reassemble in many aspects, although being more quantitative in the last figure. For this two images the wake is more intense, lower relative Mach, despite being a little bit shorter. Furthermore, the boundary layer becomes even thicker, whereas flow detachment is more relevant. The shock waves and the passage flow follow the same tendency as in Figure 4.2.6 and Figure 4.2.7.

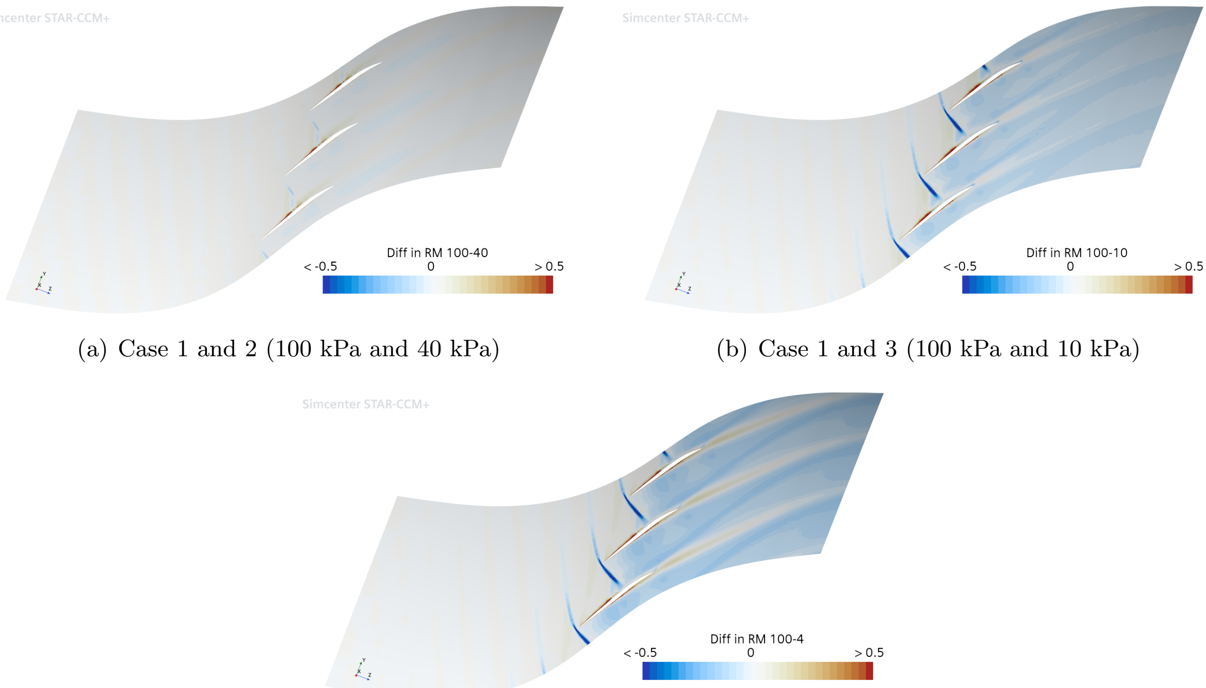

(a) Case 1 and 2 (100 kPa and 40 kPa)

(b) Case 1 and 3 (100 kPa and 10 kPa)

(c) Case 1 and 4 (100 kPa and 4 kPa)

Figure 4.2.9: Relative Mach differences on 90% span

Figure 4.2.10 shows the relative Mach number differences taking case 1 as reference in the Meridional plane. The differences in relative Mach number between cases 1 and 2 are none, despite the slight variation in the shock wave position. Cases 1 and 3 shows a greater difference in the shock wave position. The relevant differences points to the boundary layer in the hub which becomes thicker in the third case. The wake also presents important variations through the span. Increasing in intensity and length in the lower half of the span, whereas slightly shrinking on the upper half. Tip clearance effects are also higher, as the relative Mach is considerable smaller in the 10 kPa, specially in the shroud near the blade. The passage velocity boosts with respect to the first case.

Finally the differences between cases 1 and 4, present similarity between cases 1 and 3 differences in the hub boundary layer, shock wave and passage velocity, although with a higher intensity. The focus is put onto the wake, which increases with less intensity with respect to the previous comparison. The lower span half shows a higher wake intensity, with respect to the first case, although this difference in higher on the third case. The upper span shows a bigger wake difference, which is even higher than in the 10 kPa case. This wake increase for higher spans could be due to the higher tip clearance effects for lower pressures.

It is also mentioned that the boundary layer in the shroud is thicker for the first case. This fact could be due to the higher relative Mach achieved in the passage for lower pressure and therefore more energetic and turbulent boundary layers.

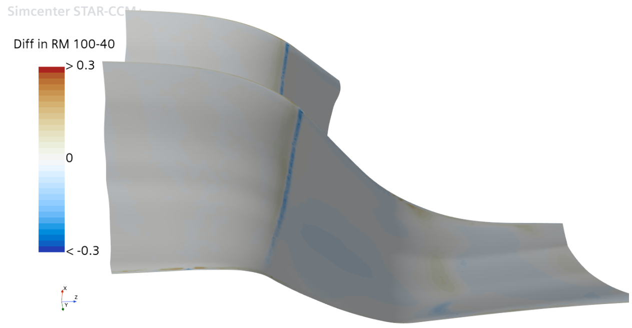

(a) Case 1 and 2 (100 kPa and 40 kPa)

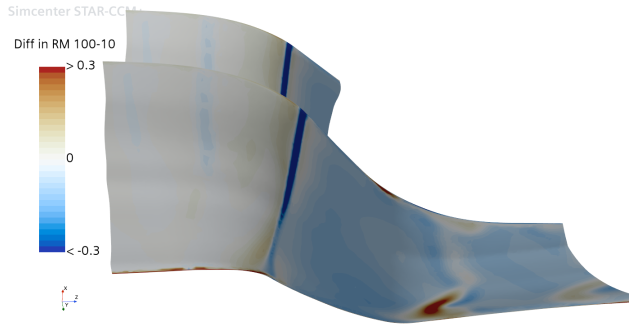

(b) Case 1 and 3 (100 kPa and 10 kPa)

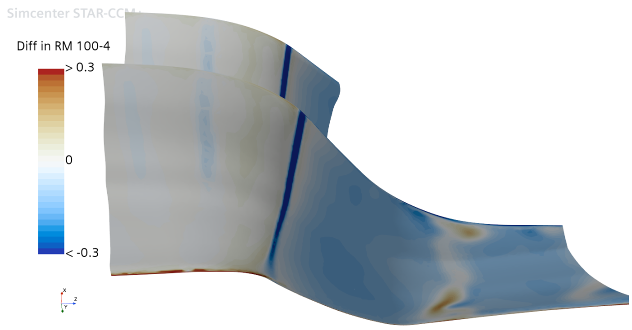

(c) Case 1 and 4 (100 kPa and 4 kPa)

Figure 4.2.10: Relative Mach differences on the Meridional plane

To sum up, the differences between cases 1 and 2, are almost negligible compared to the ones present between cases 1 and 3, and cases 1 and 4. When decreasing the operational pressure one order of magnitude from 100 kPa to 10 kPa, the effects become really noticeable. However this big differences doesn't increase when decreasing even more the operational pressure to 4 kPa, showing similar flow patters to the third case.

More comparisons between the cases are presented in Appendix A. Specially differences between cases 2 and 3, 2 and 4, and 3 and 4 are included.

4.3 Flow coefficients

To compare the low pressure effects on the compressor, some relevant flow parameters, such as the pressure coefficient, the skin friction coefficient and the intermittency, are used to study the flow behavior around the blade under different conditions. The following plots show the evolution of the mentioned parameters, differentiating the intrados and extrados for the different pressures cases.

To compute the indicated flow parameters the following formulas are used. Note that position is adimensionalized using the chord at 50% span.

$$C_p = \frac{P - P_{op}}{\frac{1}{2} \cdot \rho \cdot U^2} \ , \ \ (P_{op} \ depends \ on \ the \ case) \tag{24}$$

$$C_f = \frac{\tau_w}{\frac{1}{2} \cdot \rho \cdot U^2} \tag{25}$$

$$In = f(Re_c) \tag{26}$$

Is important to mention that the wall shear stress, τ_w, is compute in STAR CMM+ is computed creating a special laboratory reference system for each span. This reference system will have its origin in the leading edge and its Y component in the direction of the trailing edge, so that the wall shear stress is computed in the direction parallel to the the blade surface.

The Intermittency is a parameter that depends on the turbulence model, k - ω SST, and the transition model used, γ - $Re_{\theta t}$ Gamma ReTheta model, the intermittency represents the flow regime. Values close to 0 correspond to near laminar flow, while fully turbulent flow correspond to an intermittency near 1. Therefore, those parts parts with a intermittency close to 0 will be more prone to boundary layer detachment when encountering a adverse pressure gradient.

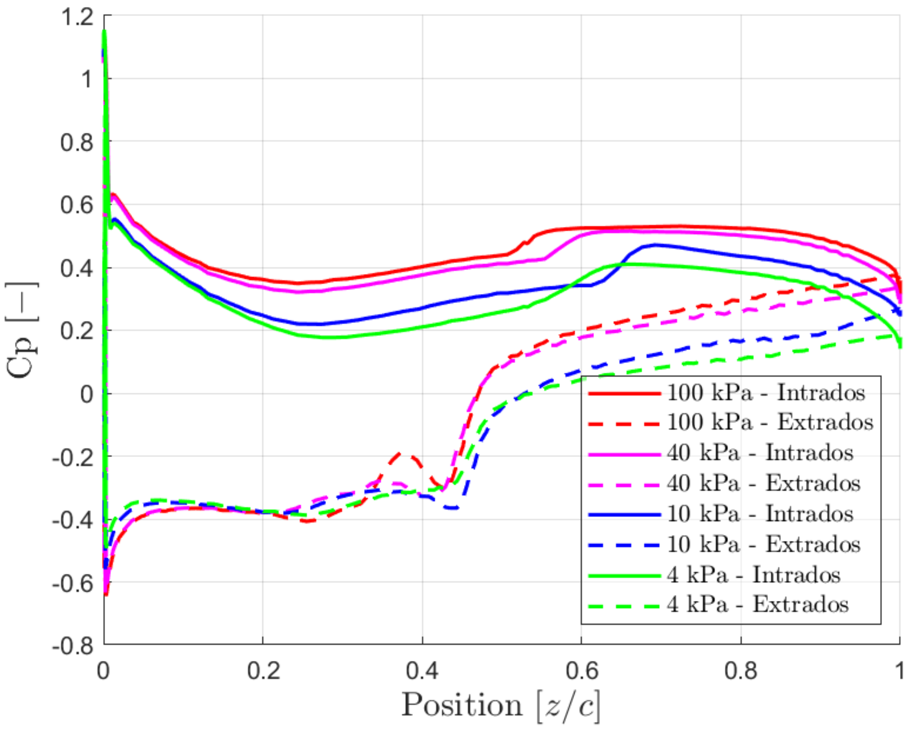

Figure 4.3.1: Pressure coefficient on 50% span plane respect to the adimensionalized position

Figure 4.3.1 shows the pressure coefficient around the extrados and intrados. In suction face (extrados) flow separation is noticeable around z = 0.02 m, which correspond to the middle of the blade chord. The flow is accelerated until a point where the pressure coefficient abruptly decreases. This sudden shrink is due to the boundary layer detachment. As the flow is separated, the velocity around the airfoil decreases, which is traduced into a pressure increase and thus, a pressure coefficient boost [25]. The relative Mach decrease due to flow detachment is an effect present in Figure 4.2.2. The detachment of the boundary layer is similar for all the operational pressures, however in case 1, a slight detachment and reattachment is produced immediately after the main flow separation. Moreover, a small plateau on the extrados is shown near the leading edge, where the four cases collapse mainly due to the flow similarities at the first stages.

The pressure face (intrados), shows a smother evolution with respect to the suction face. As the boundary layer evolves and gets thicker (already seen in the flow patters), the velocity around the blade decreases, and therefore an increase in the pressure coefficient is produced. An abrupt increase is produced near the middle of the blade, probably due to the transition to a totally laminar and wider boundary layer, as it will be corroborated in Figure 4.3.4. At the end of the pressure face the flow is re-accelerated, showing higher pressure coefficient losses for lower pressures of operation, due to frictional losses that are more present in laminar boundary layers.

For lower pressures of operation the greater passage velocities produce higher relative velocities around the blade, which are traduced to lower pressure coefficients. This higher velocities and the laminar boundary layers nature produce a lower static pressure recovery specially for low pressures of operation. As it will be corroborated in the future in subsection 4.4, the cases 1 and 2 have similar static pressure recovery at the trailing edge, whereas case 3 and 4 diverge more as the pressure is further decreased. Furthermore, in the suction side the first peak, which indicates the blade lift generated, decreases with the pressure of operation, showing a worse performance because the flow becomes more unstable at low pressures. Consequently the pressure ratio and adiabatic efficiency become worse.

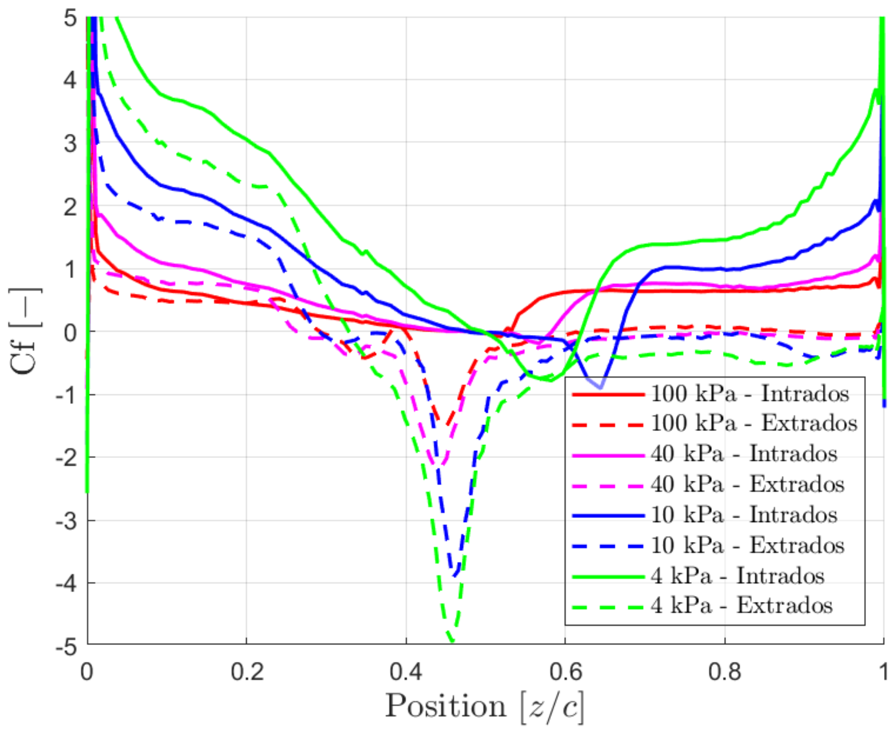

Figure 4.3.2: Skin friction coefficient on 50% span plane respect to the adimensionalized position

Figure A.3.2 shows the skin friction coefficient around the extrados and intrados. As the friction coefficient is positive the flow is moving forward in the vicinity of the wall, however, as soon as this value is negative the flow will be traveling backwards (reference frame fixed on the blade LE-TE direction). Again the suction face (extrados) denotes that the flow separation occurs at the middle of the airfoil, around z = 0.02 m. In this region the friction coefficient falls below positive, which means that a re-circulation of the flow is occurring, caused by the detachment of the flow. This re-circulation is higher for lower pressures of operation and is associated with laminar boundary layers. From the detachment region, friction coefficient values will remain negative, denoting that no flow reattachment occur. Moreover, in the extrados prior to the main flow separation, C_f oscillate from positive to negative and back to positive values, this is produced by the impact of the shock wave and the production of re-circulation. This effect is relevant specially for cases 1, 2 and 3, where reattachment occurs, in case 4 the flow will direcly separate after the shockwave.

At the pressure side (intrados) the skin friction decreases and so does the pressure around the blade until the middle of the blade. As negative values are reached for the smaller pressures of operation, it could be suggested that re-circulation exits at the middle of the airfoil due to the large thickness of the laminar boundary layers and a possible flow separation. Immediately downstream an abrupt increase in friction coefficient is produced, as the flow is re-attached. The C_f keeps increasing until the trailing edge, specially at low pressures.

Lower pressures are related in both faces with higher frictional coefficients at both faces, the extrados and the intrados. Which cause a lower recovery of static pressure at the trailing edge and therefore worse performances. Near the leading and trailing edge, where the relative velocities of the flow around the airfoil are substantially higher, bigger differences of C_f are appreciated for lower operational pressures. Whereas cases 1 and 2 show flat trends, cases 3 and 4 display huge evolution's at those regions. Despite the lower frictional coefficient produced by laminar boundary layers with respect to turbulent [26], the lower density and higher velocities near the wall (higher stresses) produce the increase of the C_f, specially for lower pressure of operation, see Equation 24.

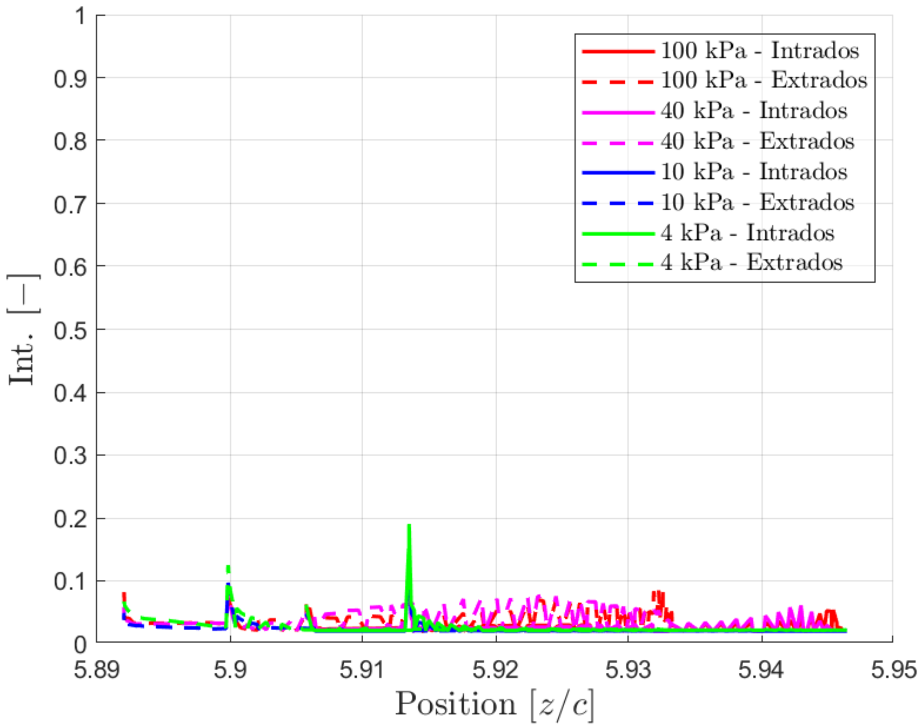

Figure 4.3.3: Intermittency on 50% span plane respect to the adimensionalized position

Figure 4.3.3 shows a really low intermittency for all the cases. Since the extrados and intrados derived parts are attached to the wall, the intermittency evaluated on the Gamma ReThetat transition model, used won't bring relevant. Due to the closeness between both derived parts to the wall, is logical to think that the intermittency should be 0, for all the cases. Therefore to analysis this parameter Intermittency contour plots are added for the four cases. This figures will help understanding the intermittency distribution around the blade.

Figure 4.3.4 shows the intermittency contour plot on the 50% span section. On the suction side (extrados) the tendency is to evolve from a turbulent boundary layer into a more laminar one. However, after the shock, flow detachment occurs and the boundary layer recovers its turbulent nature, specially for cases 1 and 2. Cases 3 and 4, show a huge difference in their boundary layer nature. Despite following a similar tendency the laminar layer shrinks in thickness after the shock wave but does not disappear. As it is evidently seen, lower pressures of operation are directly related to huge decreases in intermittency, achieving complete laminar boundary layers for case 4 and almost complete for case 3.

On the pressure side (intrados) intermittency grows in the first two cases, despite this evolution the boundary layers will remain turbulent in both cases. The intermittency will grow and become 0 specially at the trailing edge of the last two cases. The abrupt increase in the pressure coefficient is due to the transition into a wider a completely laminar boundary layer which takes place at the middle of the intrados. Further downstream the boundary layer is totally laminar and increases in thickness. This effects are slightly bigger in case 4 compared to case 3.

Is also noticeable that although the wake always remains turbulent, the passage flow evolves to more laminar state when decreasing the pressure of operation.

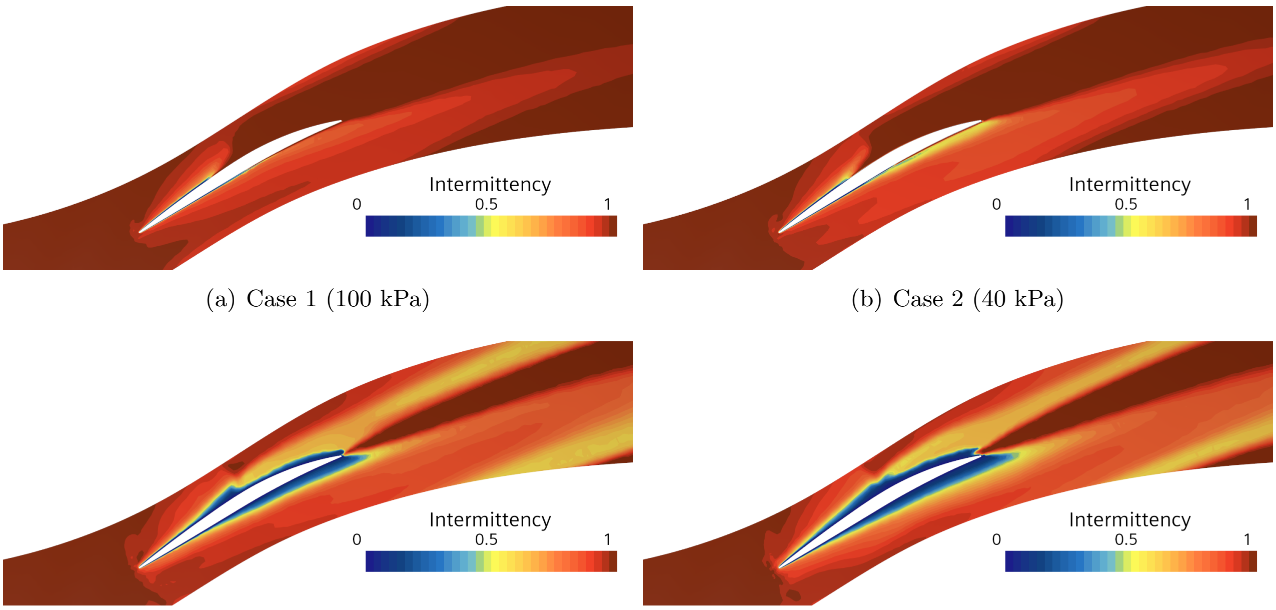

(a) Case 1 (100 kPa)

(b) Case 2 (40 kPa)

(c) Case 3 (10 kPa)

(d) Case 4 (4 kPa)

Figure 4.3.4: Intermittency contour plot on 50% span

Note that only the 50% span plane is used in this analysis. The reason is already mentioned, and is based on the similarities of this section and the mean flow and also the lack of information contributed by the 10% and 90% span planes. Despite bringing less insight, the rest of the plots for the different flow in different span sections can be compared in Figure A.3.1, Figure A.3.2 and Figure A.3.3.

4.4 Pressure losses

In order to compute the total pressure losses among the compressor, the pressure coefficient is employed. The pressure coefficient in an axial compressor is a dimensionless parameter that represents the ratio of the pressure difference across it to the dynamic pressure of the inlet. It provides insight into the compressor's performance and efficiency. The Equation 27 shows the formula of the mentioned coefficient.

$$C_{p,loss} = \frac{P_{1tr} - P_{2tr}}{P_{1tr} - P_1} \tag{27}$$

On Table 4.4.1 the pressure loss coefficients are shown for the four cases. As it can be seen the decrease in the operational pressure is directly related to a increase in the pressure loss coefficient, and therefore a worse performance. The reason for the shrinking in this parameter is the greater friction losses, generated due to the laminar behavior of the boundary layer under low pressures.

	Case 1 (100 kPa)	**Case 2 (40 kPa)**	**Case 3 (10 kPa)**	**Case 4 (4 kPa)**
Pressure loss coefficient, $C_{p,loss}$	24.503%	24.824%	25.314%	27.1704%
Difference to the previous case, $\delta C_{p,loss}$	-	0.321%	0.49%	1.856%

Table 4.4.1: Pressure loss coefficients

Figure 4.4.1 shows the tendency on the pressure loss coefficients as the pressure of operation is decreased. The coefficient tendency is to exponentially increase as the pressure of operation decreases. The low pressure conditions promote the appearance of a laminar boundary layer, increasing the friction and losses across the blade exponentially as the pressure becomes lower. The huge difference between Case 3 (10 kPa) and Case 4 (4 kPa) depicts this effect.

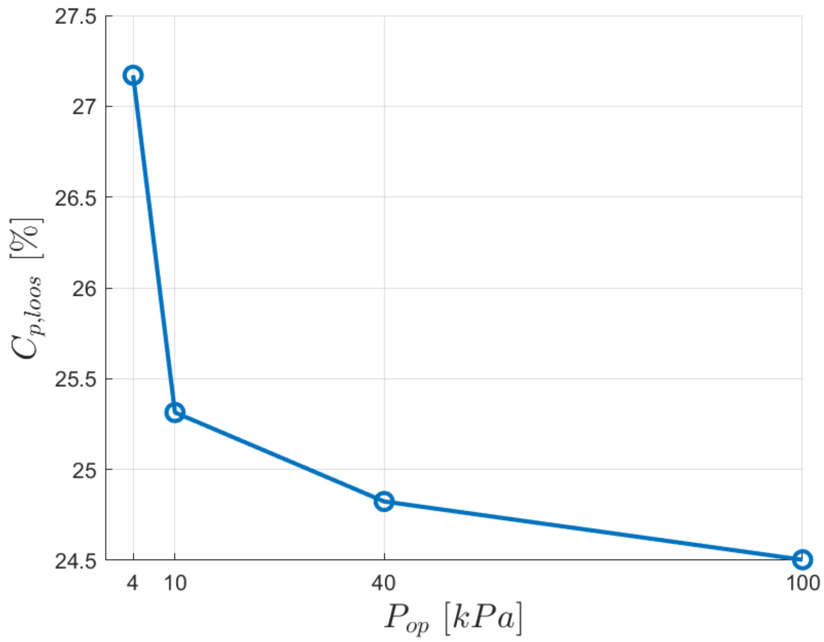

Figure 4.4.1: Pressure loss coefficient

This hypothesis is corroborated on the previous sections, where the global parameters, flow patters and flow coefficients show worse performance when decreasing the operational pressure.

4.5 Experimental results

The main purpose of studying specifically NASA ROTOR-37 geometry becomes the possibility of comparing the results from the CFD simulations with the experimental results. Allowing the validation of the CFD models and bringing insight on their accuracy.

However, the experiments carry out on this geometry where performed under ambient pressure and therefore, case 1, with a pressure of operation of 100 kPa, is the only case which can be compared. Yet they are no test facilities able to experiment which such low pressures as the ones used in a Hyperloop tube. Comparisons among all the cases is done graphically for the global parameters only, to compare the distance between the models and the experimental design point. Comparisons among local effects are only done for the first case.

In order to asses a complete comparison of the CFD results with the experimental results of the NASA ROTOR-37 model [24], a particular order is followed. First, the global data in compared, after that the local effects, specially on the flow patterns, are addressed.

4.5.1 Global experimental data

The main global parameters discussed across the article consist of the pressure ratio, adiabatic efficiency and the corrected mass flow. The first two are graphed into speed lines. Since the CFD simulations are performed at the design speed (1800 rad/s) and with a constant corrected mass flow (20.2 kg/s), the comparison of the cases will be done for the Design Intent point.

On both Figure 4.5.1 and Figure 4.5.2 a constant corrected mass flow line is drawn where the global CFD results are drawn. It is worthy mentioning that in the experimental conditions where carried under reference temperature and pressure and therefore the corrected mass flow is equivalent to the mass flow. Note that both figures are manually drawn, and therefore the representation is not completely accurate when representing the values of pressure ratio and adiabatic efficiency.

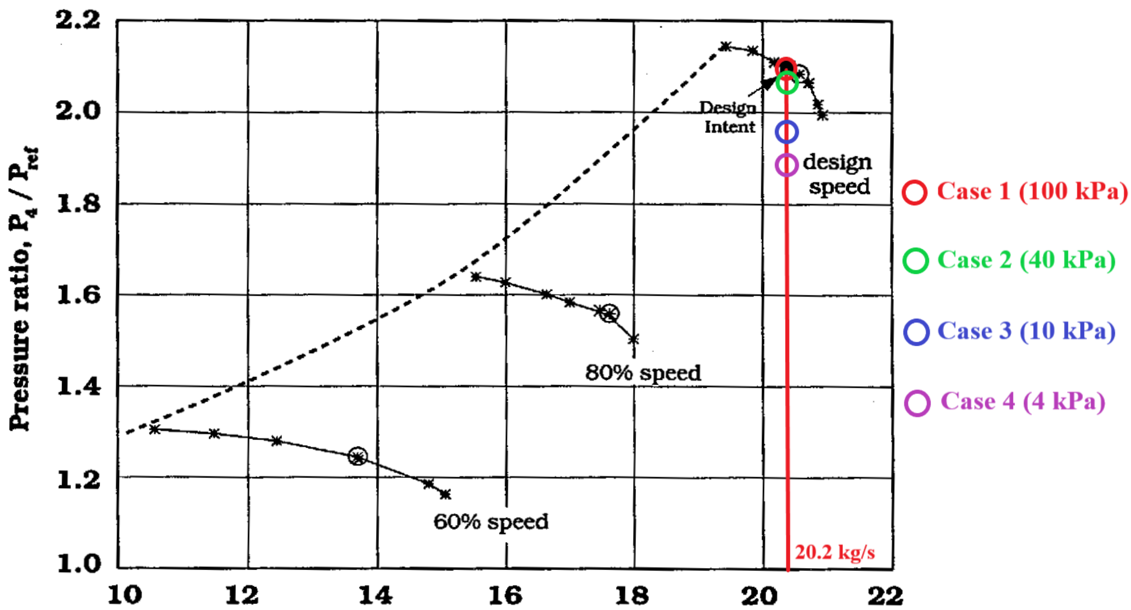

Figure 4.5.1: NASA ROTOR-37 pressure ratio map [24]

Figure 4.5.1 displays the pressure ratio lines for different speeds. The Design Intent point almost collapse with the case 1 point. The distribution of the pressure ratio for the rest of the cases follows an already mentioned tendency. Whereas case 1 and therefore case 2, are really closed to the Design Intent point, a big steps separates case 3 and 4. Those case show lower pressure ratio as a consequence of the bigger losses in static pressure, presented in subsection 4.4. Case 4 is even further away from the reference point, since it has the biggest pressure losses. However, the pressure ratio obtained for the last two cases, is clearly above the pressure ratio line of 80% speed. This indicates that despite the worse performance and higher energy consumption for lower speeds the differences between pressure ratios does not suppose an extreme effect.

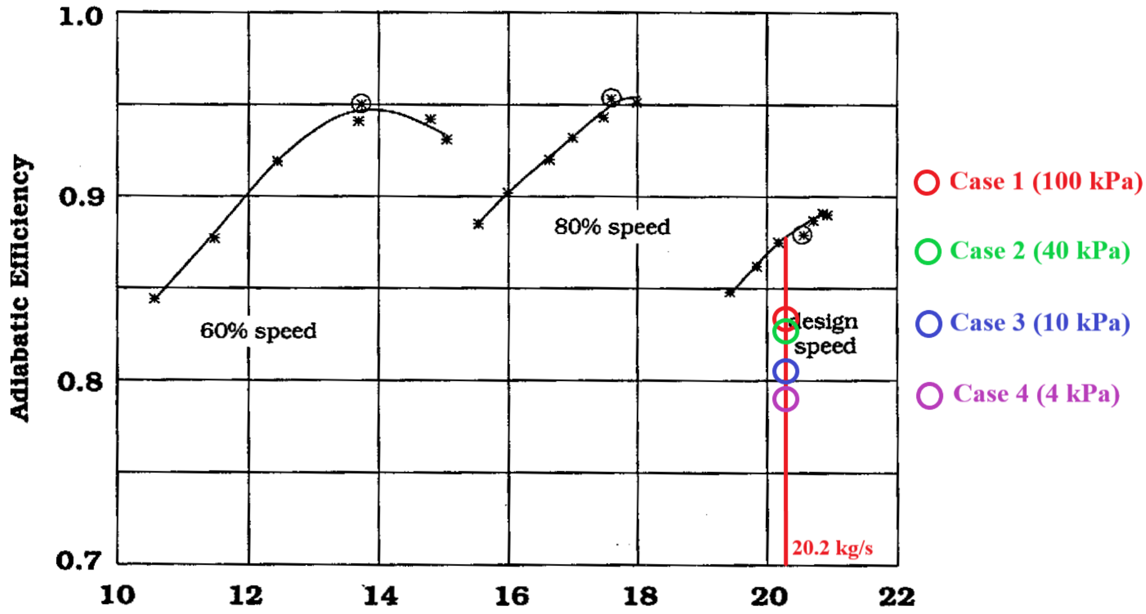

Figure 4.5.2: NASA ROTOR-37 compressor efficiency map [24]

Figure 4.5.2 displays the adiabatic efficiency lines for different speeds. In this case the adiabatic efficiency of case 1 is clearly lower than the Design Intent point. This divergence could probably be due to the CFD models errors an is further discussed in detail. Again the tendency between cases is similar showing close efficiencies for the first two cases and bigger discrepancies between the two others. It is important to note that because of the CFD inaccuracy and the low pressures of operation the adiabatic efficiency is far lower in the simulations than in the experimental design points. The illustration shows a good efficiency for the 60% and 80% speeds lines, where the efficiency reaches up 0.95. Respect to the Design Intent point, where efficiency reaches 0.9, the difference is considerable between the CFD models with values of 0.83-0.79. As already explained friction losses, due to the laminar nature of the boundary layer contribute to a worse performance.

	Experimental results	**Case 1 (100 kPa)**
Corrected mass flow, $\dot{m}_c$ [m/s]	20.188	20.191
Corrected mass flow difference, $\delta\dot{m}_c$	+0.0149 %	
Pressure ratio, π_c	2.106	2.1127
Pressure ratio difference, $\delta\pi_c$	+0.3176 %	
Rotor efficiency, η	0.877	0.8328
Rotor efficiency difference, $\delta\eta$	-5.1702 %	

Table 4.5.1: Experimental global parameters comparison

It is important to note that the relative differences are computed between the experimental and CFD result using the following equation, Equation 28. Where X_{EXP} and X_{CFD} correspond respectively, to the experimental and CFD values from case 1 (100 kPa).

$$\delta = \frac{X_{CFD} - X_{EXP}}{\frac{X_{EXP}+X_{CFD}}{2}} \tag{28}$$

Table 4.5.1 summarize the comparison between the experimental results published in [24] and the CFD results for case 1. Regarding the corrected mass flow the difference is minimal and could be negligible, this tiny error arise from the manual iterative process to achieve the given corrected mass flow rate. The pressure ratio difference is also small, lower than 1%. In this case the CFD model obtain higher values with great accuracy. Finally the rotor adiabatic efficiency is the main source of concern due to the big relative difference of about 5%. Looking into the definition of the adiabatic efficiency, Equation 21, and knowing that the pressure ratio in for both cases is similar, the only discrepancy arise on the temperature ratio. Several effects regarding friction losses, could be the reason for this difference which provoke a larger temperature ratio and therefore lower efficiency.

Regarding literature review a huge portion of the comparisons showed similar trends. On the one hand the pressure ratio tended to be over-predicted by the CFD codes. Whereas, the adiabatic efficiency tended to be lower in the CFD cases. Figure 4.5.3 and Figure 4.5.4 compare the algebraic/mixing length turbulence models and experimental data. Both parameters are represents in function of the normalized mass flow, which represents: $\dot{m}/\dot{m}_{max}$.

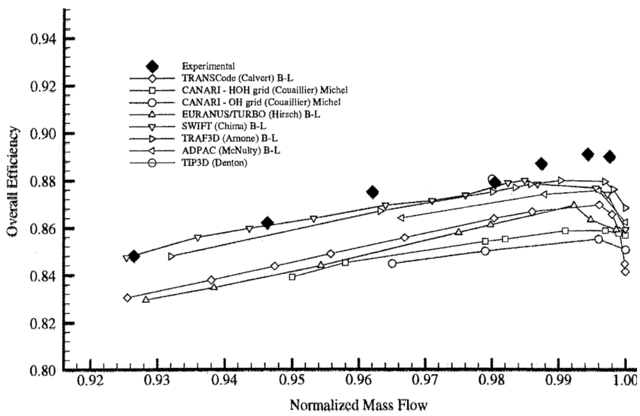

Figure 4.5.3: Comparison of CFD and experimental adiabatic efficiency [27]

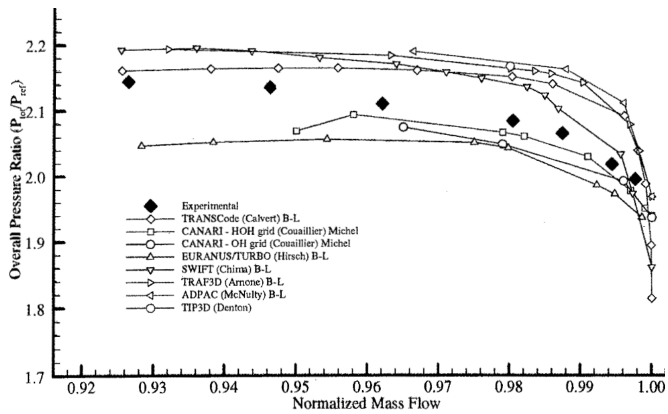

Figure 4.5.4: Comparison of CFD and experimental pressure ratio [27]

Figure 4.5.3 compares the adiabatic efficiency of the CFD models and the experimental results. All the models show a lower adiabatic prediction, as in this case, which is caused by the over estimation of the frictional losses. [27] points that the losses are specially over-estimated in the tip wall region, due to the tip clearance. The article also points out that the losses near the side walls are also higher in the CFD models.

Figure 4.5.4 compares the pressure ratio of the CFD models and the experimental results. The majority of the models show a higher pressure ratio, as in this case, which is caused by corner stall. Corner stall is observed at the hub of Rotor 37, which was affected by the presence of a small axial gap in the hub annulus line just upstream of the rotor. Most of the codes didn't implement that gap and therefore they over-predicted the pressure ratio.

4.5.2 Local experimental data

This section will be divided into two parts, in the first one the blade-to-blade effects will be studied, the second one, focus on the cross-channel planes from two different stations of the rotor.

Blade-to-Blade Relative Mach contour

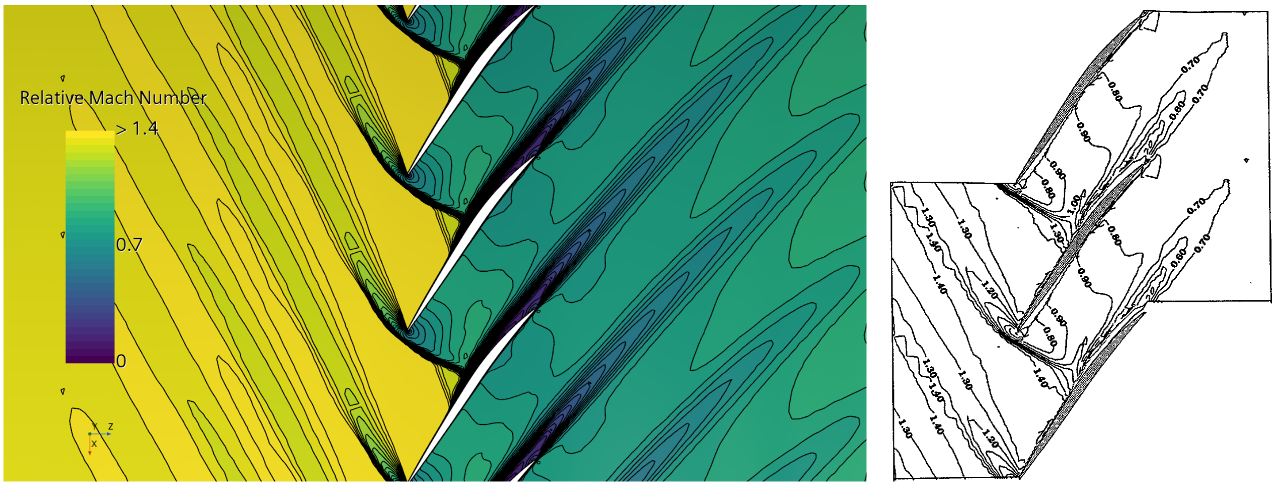

(a) CFD results (Case 1, 100 kPa) (b) Experimental results

Figure 4.5.5: Relative Mach contour comparison at 70% span

Figure 4.5.5 show a global picture of the relative Mach contour along three rows of blades. Overall, both the experimental and CFD cases show evident similarities in the Relative Mach. The bow shaped shock wave and it's interaction with the blade below show indistinguishable differences in the contour. The wake breadth and lenght and the flow detachment also dentes huge similarity. Despite, the slight differences in the passage flow across the channel and the pressure side boundary layer, the figures could be considered identical.

It must be noted, that the shape of the contour lines highly depends on the scale resolution, number of lines, maximums and minimums... and therefore some differences arise. Moreover, the erratic shape of the experimental lines differ from the CFD ones as a RANS model is used where the turbulence is time-averaged and therefore the lines are smooth.

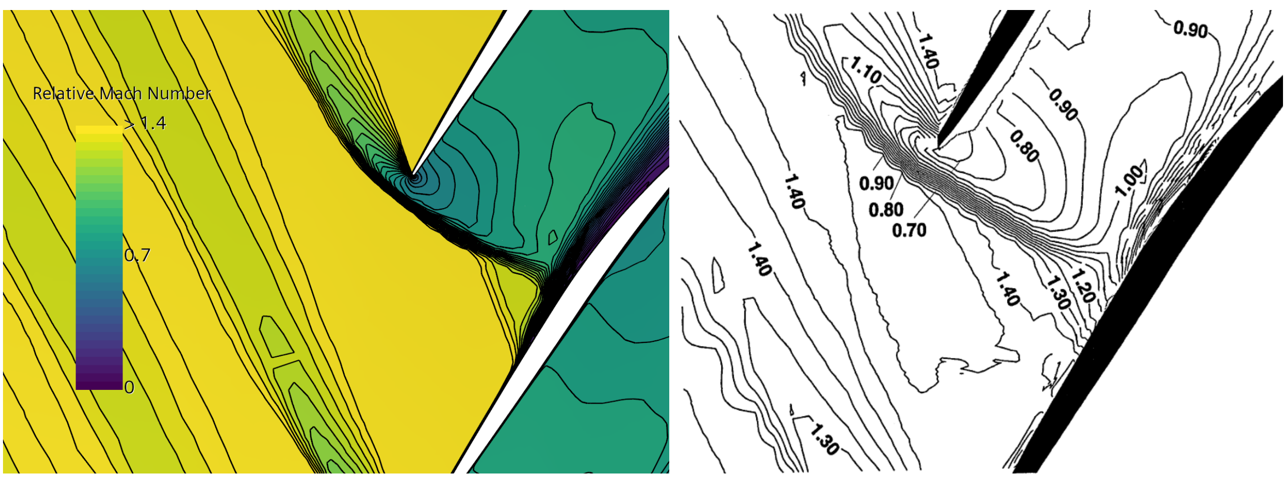

(a) CFD results (Case 1, 100 kPa) (b) Experimental results

Figure 4.5.6: Relative Mach zoom contour comparison at 70% span

On Figure 4.5.6 a closer look to the passage is taken. Again, clear similarities are found in the shock wave, passage flow in the channel, interaction between the shock wave and the lower blade boundary layer, and the boundary layer detachment. Slight differences occur in the pressure peak, at the from of the shock wave where lower relative Mach is expected and at the pressure side boundary layer. Again lines seen more erratic than in CFD due to the usage of a RANS model of turbulence.

Cross-channel Relative Mach contour

Finally the cross-channel relative Mach contour will compare the relative Mach number in the circumferential region in station 1a (immediately upstream of the rotor) and station 3 (downstream of the rotor), both parameterized in Figure 2.3.5. The plots try to achieve maximum similarity to the ones provided in the article [24].

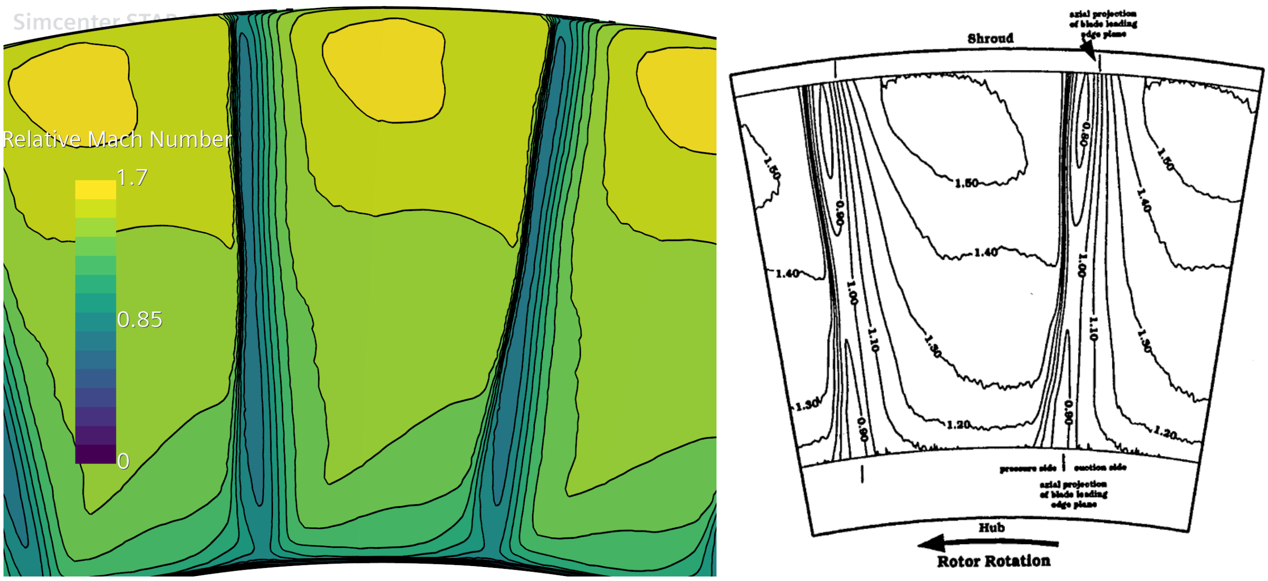

(a) CFD results (Case 1, 100 kPa) (b) Experimental results

Figure 4.5.7: Relative Mach contour comparison at the cross-channel plane on Station 1a

Figure 4.5.7 depicts the relative Mach contour in station 1a which is 5% a chord distance from the leading edge and parallel to it. The passage flow and shock waves show general similarities. However, a higher relative Mach is predicted at the middle of the blade perturbation. While decline on velocity should occur on the perturbation near the shroud and the hub. Regarding the passage flow, the lower section shows a different shape, with higher velocities in the lower left corner.

Regarding Figure 4.5.8, relative Mach contour is depicted for station 3. This station is parallel to the inlet and outlet, radial-circumferential plane, and is located just before the trailing edge intersection with the shroud. Again general similarities are present, depicting similar contour lines for the wake and the flow passage. This figure shows a relevant different on the wake, which is more pronounced near the shroud and with lower relative Mach numbers. Similarly to the previous image at the middle of the wake the velocity is also slightly higher, over-predicting the wake intensity in both regions.

Is important to note that the cross-channel plots are only showed between the a 15% and 97% and therefore the effects related to the hub and the shroud, are not included. This directly affects the tip clearance comparison which can not be done.

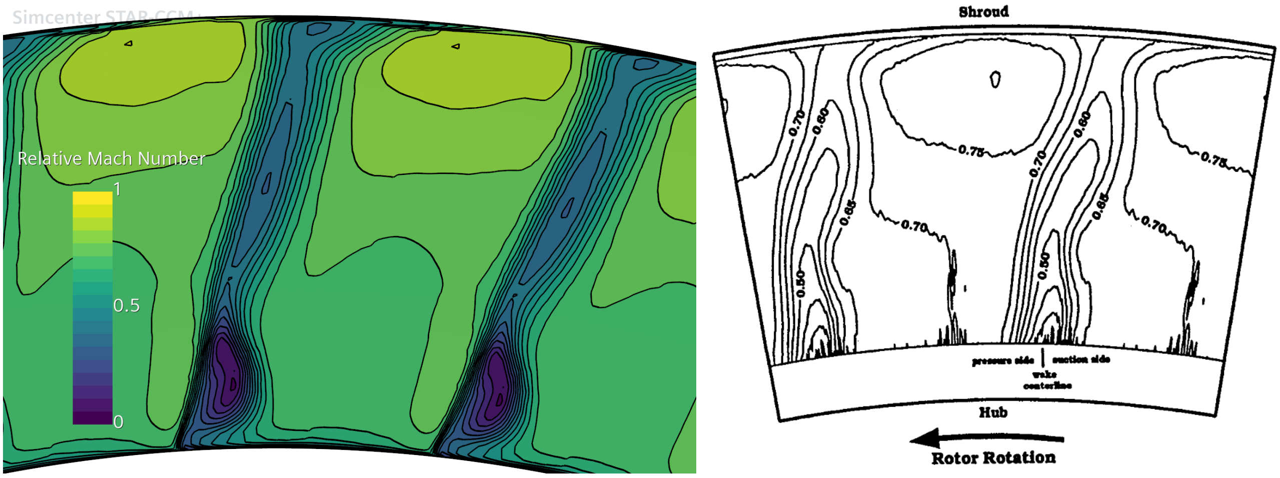

(a) CFD results (Case 1, 100 kPa) (b) Experimental results

Figure 4.5.8: Relative Mach contour comparison at the cross-channel plane on Station 3

As a conclusion of this section, despite in global terms efficiency is under-estimated, literature shows that is a normal effect on CFD and that the rest of terms are accurate to experimental results. Moreover, the flow patterns are really similar and figures resemble to experimental results, despite the different layout. All this validates case 1 accuracy, proving the fidelity of the used models in the rest of the cases and their accuracy. Furthermore, the results on this section are akin to the ones shown in Segarra's work [14].

5 Concluding remarks

5.1 Comparison with the Hyperloop geometry

Finally the CFD cases tendencies from NASA ROTOR 37 are compared against the data obtained in the article of Galindo et al. [13]. The graphs serve to validate the evolution of the efficiency and the pressure ratio when decreasing the pressure of operation or Reynolds number.

Is important to note that the data extracted from the Hyperloop article is collected at the same corrected mass flow, 53 kg/s, which diverges from the NASA R-37 corrected mass flow, 20.2 kg/s. Therefore, some of flow patterns effects are not similar between the cases, as the incidence angle is different. This fact could lead into discrepancies in the trends.

Pressure of operation tendencies

First the efficiency and the pressure ratio of the rotor is depicted in function of the pressure of operation. The ROTOR 37 geometry has a bigger efficiency than the Hyperloop one. As the pressure of operation decreases and evident decrease in the efficiency is observed in Figure 5.1.1. For both the CFD results and Hyperloop data the tendency is similar and smooth decline in efficiency is produce, for a P_{op} between 100 kPa and 10 kPa. As the pressure reaches 4 kPa, the Hyperloop geometry shows a bigger diminish in the studied parameter. The decrease is even more pronounced for lower pressures, denoting that the blade shape is not clearly optimized for conditions close to vacuum.

Similarly, the pressure ratio is considerably higher for the ROTOR 37 geometry. Regarding this parameter, Figure 5.1.1 shows that while pressure ratio remains constant from 100 kPa to 10 kPa P_{op} on the Hyperloop, a pronounced decrease occurs for the ROTOR 37 geometry. Between 10 kPa dn 4 kPa the pressure decrease in similar manners, keeping this trend until 2 kPa in the Hyperloop case. The huge differences in pressure ratio could be caused by the differences in the flow behavior when decreasing the operational pressure, which reflects differences between both geometries.

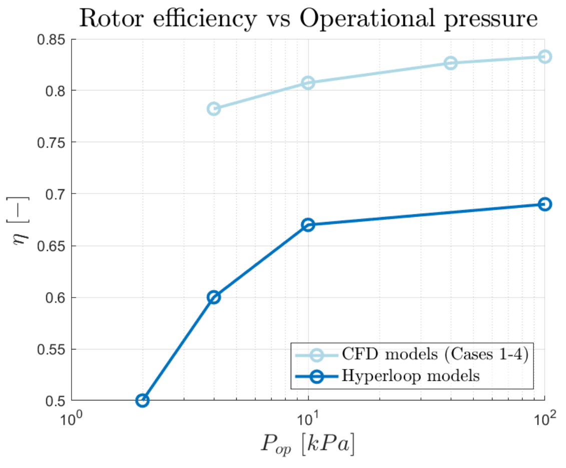

Figure 5.1.1: Rotor efficiency for different P_{op}

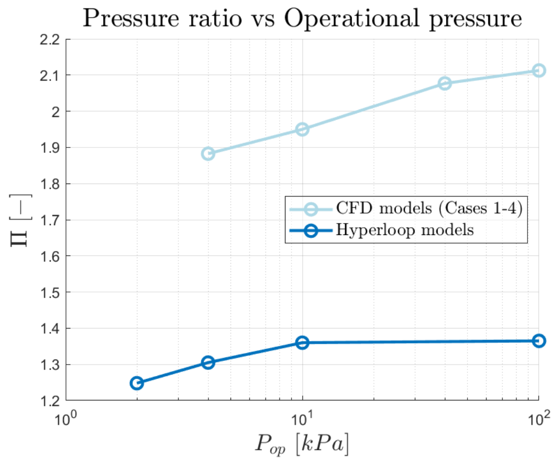

Figure 5.1.2: Pressure ratio for different P_{op}

Reynolds number tendencies

As the Reynolds number is clearly related to the pressure of operation through Equation 18, where density is dependent on the pressure, similar tendencies to the previous comparisons are depicted. Contrary to pressure of operation, the Reynolds number is not coincident between the different cases of the two geometries. When comparing in function of the Reynolds number, the ROTOR 37 curve moves leftwards, since it shows lower Reynolds than the Hyperloop geometry. Again for high Reynolds both cases show similarity, but for lower ones the abrupt decrease in efficiency occurs in the Hyperloop case but is not visible in ROTOR 37, see Figure 5.1.4.

Regarding efficiency, Figure 5.1.3 shows closer tendencies between the two geometries when switching leftwards the curve. However, similarly to the previous graph, similarity only occurs for lower Reynolds numbers.

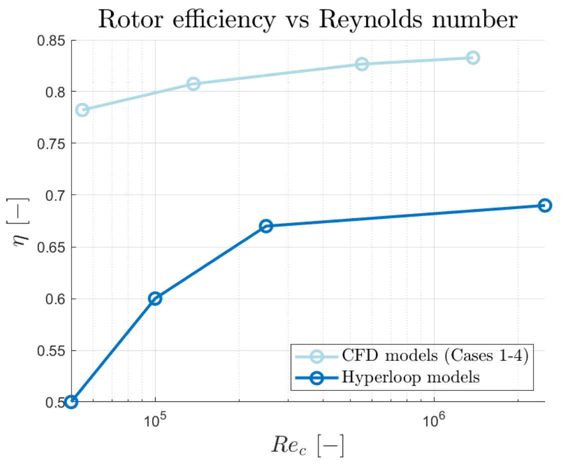

Figure 5.1.3: Rotor efficiency for different Re_c

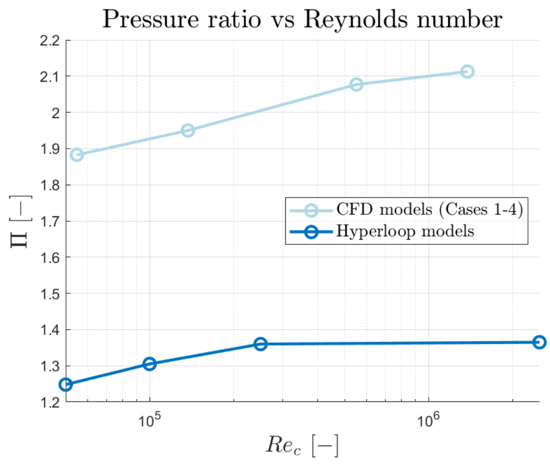

Figure 5.1.4: Pressure ratio for different Re_c

In general terms the tendency in efficiency for high pressures of operation and Reynolds numbers is similar, while becoming more abrupt in the Hyperloop case for low values of P_{op} and Re_c. The pressure ratio, shows the opposite, for high values of pressures of operation and Reynolds numbers both cases tendencies diverge (constant π_c in the Hyperloop case), while for low π_c they resemble.

5.2 Conclusions

This project conducts a study of the performance of an axial compressor for a decreasing pressure of operation and thus, a dramatically reduction of Reynolds number. In the framework of Hyperloop operating pressure, the performance of a turbomachinery-based propulsive system should be studied. Therefore, the ROTOR-37 performance is simulated under low Reynolds, at which no study has been conducted.

Regarding global parameters, pressure ratio and efficiency, similar trends are observed to the ones in the literature. From 100 kPa to 40 kPa (case 1 to 2), the differences are small, lower than 2%. However, when decreasing even more the pressure of operation, to values of about 10 kPa (case 3) the differences start to be more noticeable. For even lower pressures, 4 kPa (case 4), this tendency becomes even sharper.

Flow velocity contours show that the flow separation is aggravated by the pressure of operation decrease, totally damaging the performance of the compressor. The pressure of operation reduction causes the boundary layer to be less energetic, becoming a laminar boundary layer. This type of boundary layers are more prone to detach under adverse pressure gradients and are thicker. Consequently, the pressure decrease is also attached to a higher total pressure loss across the rotor, due to the nature of the boundary layer, causing higher frictional losses.

The differences in velocity contours show how the thicker boundary layers and weaker shock wave under lower pressures, provoke a higher blockage. Therefore, higher velocities are achieved at the blade passages arising as another symptom of the performance decline. The decrease of operational pressure also increases the intensity of the passage and tip clearance vortexes. This effect is inflicted by the increased thickness of the boundary layer at the hub, blade and shroud and it's tendency to easily detach. It is also noticeable that the passage vortex achieves it maximum intensity at 10 kPa, while tip clearance effect is bigger at 4 kPa.

As a consequence of the higher passage velocity, flow detachment and vortexes intensity, provoked by the laminarity of the boundary layer, the performance shrinks. As the global parameters forecasted, the contour differences in relative Mach numbers are small for cases 1 and 2 and clearly diverge for cases 1 and 3 and even more for cases 1 and 4.

The results comparison show high fidelity between the CFD and experimental results, especially in the Blade-to-Blade plane. Slight differences are seen on the cross-channels as a consequence of the viscous effects. Furthermore, the pressure ratio is slightly overestimated, whereas the efficiency is moderately underestimated. Literature review suggest that for the majority of the turbulence models, that the overestimation of tip clearance vortexes decreases the CFD efficiency. Whereas, corner stall due to a small axial gap not included in the CFD is the cause of the overestimation of the pressure ratio. Despite this the slight differences is some results, the CFD results and models are be validated for ambient conditions, due to the major similarities on the great part of results.

On this analysis, is of great importance to capture the nature of the boundary layer. The RANS (steady), $k-\omega$ SST model with $\gamma - Re_{\theta t}$ transition turbulence model, seems to properly predict the flow behavior, as demonstrated on the experimental results and literature review. However, the transient nature of the rotor, arise as one of the constant error causes during our analysis.

Finally regarding the Hyperloop comparison, similar tendencies are achieved, specially when comparing the Reynolds number. However, the discrepancies in flow conditions and geometry provoke trend differences. Despite this, the trends and differences in global and local parameters suggest a clear validation of the tendencies studied by Galiendo et al. [13].

All this insight has a direct impact on the Hyperloop system development. The study has demonstrated that low Reynolds numbers negatively affect the overall performance of an aircraft inlet compressor (decreasing up to $\eta_{min} = 0.78$). The design of an compressor capable of dealing with low-pressure effects, such as laminar boundary layer detachment, could positively increase the propulsive efficiency and feasibility on Hyperloop transportation systems.

5.3 Future work

Despite the great insight contributed by this project, the lack of time and computational resources have limited the number of CFD cases calculated. The four cases shared the same corrected mass flow, however, Galindo et al. performed a parametric study, varying the mass flow rate. Therefore for a correct comparison, it will be interesting to vary the corrected mass flow rate under a similar parametric study, obtaining the maximum efficiency points.

Moreover, it will be interesting the study of an unsteady CFD simulation of the rotor. The use of a steady problem is used for simplicity purposes, giving the hole fluid a relative velocity with respect to the blade. The unsteady problem will reassemble more to the reality, being the blade with the hub the only moving parts, increasing the results accuracy despite a higher computational cost.

Also, during this project the lack of experimental results for the cases with lower pressures of operation than atmospheric, does not allow validation. The creation of experimental facilities able to perform analysis of compressors under the Hyperloop tube conditions will solve part of the uncertainty generated by the CFD model.

For future projects the analysis of a complete stage, including a rotor and a stator will enormously contribute to the Hyperloop development. The interaction between the rotor wake and vortexes with the stator under low pressures is a non-explored field important for this mean of transport.

Finally, as demonstrated in this project, rotors show a great loss of performance under low pressures of operation. Therefore, is essential the development of a blade optimized for low pressure for the Hyperloop evolution.

References

[1] European Commission and Eurostat. “Energy, transport and environment statistics - 2020 Edition”. In: (2020). DOI: doi:10.2785/522192.

[2] Ken’etsu Uchida and Nao Sugiki. “Travel demand estimation risk for high-speed railway transport considering travel price competition”. In: *Journal of advanced transportation* 47 (Dec. 2013), pp. 737–750. DOI: 10.1002/atr.194.

[3] European Commission and Eurostat. “Key figures on European transport - 2022 Edition”. In: (2022). DOI: doi:10.2785/322262.

[4] F. Frommer. “High-speeed rail”. In: (May 2024). URL: https://www.britannica.com/technology/high-speed-rail.

[5] Ilaria Grasso Macola. “Timeline: tracing the evolution of hyperloop rail technology”. In: (May 2024). URL: https://www.railway-technology.com/features/timeline-tracing-evolution-hyperloop-rail-technology/.

[6] Rescale and AWS HPC. “Zeleros Bolsters Engineering Productivity with Rescale on AWS HPC”. In: (2022). URL: https://about.rescale.com/rs/285-WFD-495/images/Rescale_AWS_Zeleros_Case_Study.pdf.

[7] Ilaria Grasso Macola. “Conceptual Feasibility Study of the Hyperloop Vehicle for Next-Generation Transport”. In: (May 2017). URL: https://ntrs.nasa.gov/api/citations/20170001624/downloads/20170001624.pdf.

[8] Tesla Coorporation. “Hyperloop Alpha”. In: (2013). URL: https://www.tesla.com/sites/default/files/blog_images/hyperloop-alpha.pdf.

[9] Maurice Bizzozero, Yohei Sato, and Mohamed Aly Sayed. “Aerodynamic study of a Hyperloop pod equipped with compressor to overcome the Kantrowitz limit”. In: *Journal of Wind Engineering and Industrial Aerodynamics* 218 (2021), p. 104784. ISSN: 0167-6105. DOI: https://doi.org/10.1016/j.jweia.2021.104784.

[10] Alex J. Lang et al. “A review of Hyperloop aerodynamics”. In: *Computers & Fluids* 273 (2024), p. 106202. ISSN: 0045-7930. DOI: https://doi.org/10.1016/j.compfluid.2024.106202.

[11] Federico Rodríguez, Temoatzin González, and Sergio Hoyas. “CFD Simulation of a Hyperloop Capsule Inside a Low-Pressure Environment Using an Aerodynamic Compressor as Propulsion and Drag Reduction Method”. In: *Applied Sciences* 11 (Apr. 2021), p. 3934. DOI: 10.3390/app11093934.

[12] Duvid C. Junetzke Jumes E. Crouse and Ricrhurd E. Schwiriun. “A computer program for composing compressor blading from simulated circular-arc elements on conical surfaces”. In: NASA-TN-D-5437 (1969).

[13] José Galindo et al. “Effect of Operational Pressure Reduction on Axial Compressor Performance by Means of 3D CFD Modeling at Nominal Operating Speeds”. In: GT2024-124093 (June 2024).

[14] Miguel Segarra López. “Analysis of the predictive capability of numerical configurations of 3D CFD axial compressor models”. In: NASA-TN-D-5437 (Mar. 2024).

[15] Marco Gambini and Michela Vellini. “Preliminary Design of Axial Flow Compressors”. In: *Turbomachinery: Fundamentals, Selection and Preliminary Design*. Cham: Springer International Publishing, 2021, pp. 155–197. ISBN: 978-3-030-51299-6. URL: https://doi.org/10.1007/978-3-030-51299-6_4.

[16] Vishwas Iyengar, Lakshmi N. Sankar, and Russell K. Denney. “A First-Principles Based Methodology for Design of Axial Compressor Configurations”. In: (2012). URL: https://api.semanticscholar.org/CorpusID:108519458.

[17] Gherardo Zambonini. "Unsteady dynamics of corner separation in a linear compressor cascade". In: (Dec. 2016).

[18] Roberto Biollo and Ernesto Benini. "Recent advances in transonic axial compressor aerodynamics". In: *Progress in Aerospace Sciences* 56 (2013), pp. 1–18. ISSN: 0376-0421. URL: https://www.sciencedirect.com/science/article/pii/S0376042112000528.

[19] Robert Meyer et al. "A Parameter study on the influence of fillets on the compressor cascade performance". In: *Journal of Theoretical and Applied Mechanics (JTAM)* Vol 50 (Jan. 2012).

[20] Debashis Dey and Cengiz Camci. "Development of tip clearance flow downstream of a rotor blade with coolant injection from a tip trench". In: (Jan. 2000).

[21] *Fluid Machinery.* Accessed: 2024-06-24. URL: https://archive.nptel.ac.in/content/storage2/courses/112104117/chapter_5/4_16.html.

[22] Donald Huebler. *Rotor 37 and stator 37 assembly.* 1977. URL: https://catalog.archives.gov/id/17468361.

[23] Jan Kamenik et al. "Application of sweep to transonic compressor rotor blades for low-order statistical moment averaging in robust design". In: Oct. 2016.

[24] Kenneth L. Suder. "Experimental Investigation of the Flow Field in a Transonic, Axial Flow Compressor with Respect to the Development of Blockage and Loss". In: (2013). URL: https://api.semanticscholar.org/CorpusID:107474184.

[25] Radoslav Bozinoski and Roger Davis. "A DES Procedure Applied to a Wall-Mounted Hump". In: *International Journal of Aerospace Engineering* 2012 (Aug. 2012). DOI: 10.2514/6.2009-3667.

[26] Duncan Ohno, Jonas Romblad, and Ulrich Rist. "Laminar to Turbulent Transition at Unsteady Inflow Conditions: Direct Numerical Simulations with Small Scale Free-Stream Turbulence". In: (Jan. 2020), pp. 214–224. DOI: 10.1007/978-3-030-25253-3_21.

[27] J. Dunham. "CFD Validation for Propulsion System Components". In: (May 1998). DOI: 10.1007/978-3-030-25253-3_21.

[28] James E. Crouse, David C. Janetzke, and Richard Earl Schwirian. "A computer program for composing compressor blading from simulated circular-arc elements on conical surfaces". In: 1969. URL: https://api.semanticscholar.org/CorpusID:107427969.

[29] Elsa Piollet, Florence Nyssen, and Alain Batailly. "Blade/casing rubbing interactions in aircraft engines: Numerical benchmark and design guidelines based on NASA rotor 37". In: *Journal of Sound and Vibration* 460 (2019), p. 114878. ISSN: 0022-460X. URL: https://www.sciencedirect.com/science/article/pii/S0022460X19304407.

[30] *Salario medio para Ingeniero Junior en España, 2024.* Accessed: 2024-06-24. URL: https://es.talent.com/salary?job=ingeniero+junior.

[31] *Salario medio para Ingeniero Senior en España, 2024.* Accessed: 2024-06-24. URL: https://es.talent.com/salary?job=ingeniero+senior.

[32] *What is the Average Lifespan of a Computer?* Accessed: 2024-06-25. URL: https://www.hp.com/in-en/shop/tech-takes/post/average-computer-lifespan.

[33] *Electricity usage of a Desktop Computer.* Accessed: 2024-06-25. URL: https://energyusecalculator.com/electricity_computer.htm.

[34] *Costs Of Electricity In Spain.* Accessed: 2024-06-25. URL: https://electricityinspain.com/electricity-prices-in-spain/#:~:text=Currently%2C%20the%20price%20for%20electricity,29.66%20per%20100%20kilowatt%2Dhour..

[35] *CFDDFC on AWS: Pricing of Computing Resources.* Accessed: 2024-06-25. URL: https://cfd.direct/cloud/aws/pricing/.

Appendices

A Extra Results Figures

On this Appendix extra result analysis are included, which are not consider essential, but increase the insight of the compressor performance under the different operational pressures. For this reason figures which compare relative mach between the rest of the cases, intermittency contour plots and coefficients plots for different span sections are depicted among this section.

A.1 Relative Mach differences

On this subsection, the relative Mach number difference is computed for the rest of possible combinations between cases. The figures agree with the hypothesis already figured in section 4.

The differences between the cases 2 and 3; 2 and 4; 3 and 4, in relative Mach number for the 10% span plane, are depicted in Figure A.3.4.

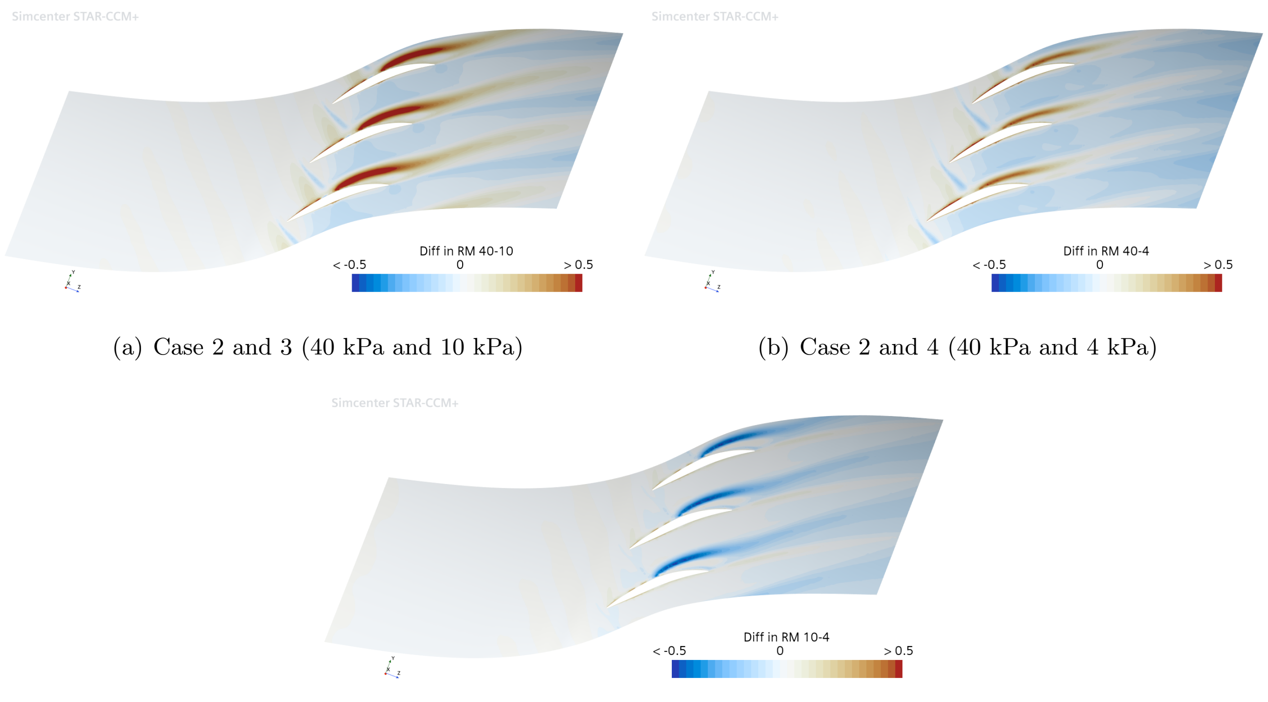

(a) Case 2 and 3 (40 kPa and 10 kPa)

(b) Case 2 and 4 (40 kPa and 4 kPa)

(c) Case 3 and 4 (10 kPa and 4 kPa)

Figure A.1.1: Relative Mach differences on 10% span

The differences between the cases 2 and 3; 2 and 4; 3 and 4, in relative Mach number for the 50% span plane, are depicted in Figure A.1.2.

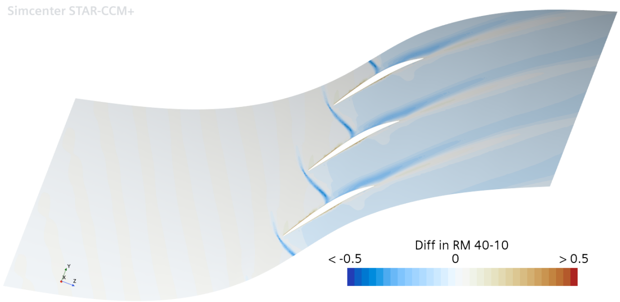

(a) Case 2 and 3 (40 kPa and 10 kPa)

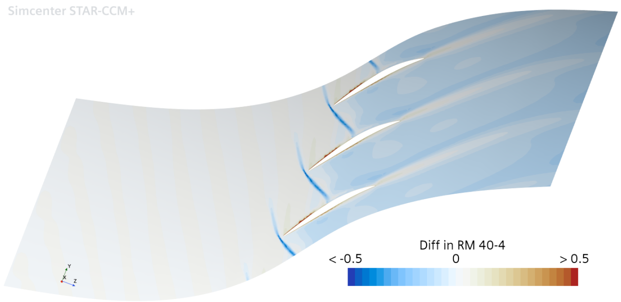

(b) Case 2 and 4 (40 kPa and 4 kPa)

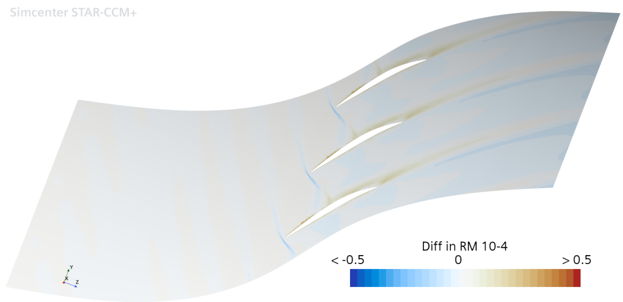

(c) Case 3 and 4 (10 kPa and 4 kPa)

Figure A.1.2: Relative Mach differences on 50% span

The differences between the cases 2 and 3; 2 and 4; 3 and 4, in relative Mach number for the 90% span plane, are depicted in Figure A.1.3.

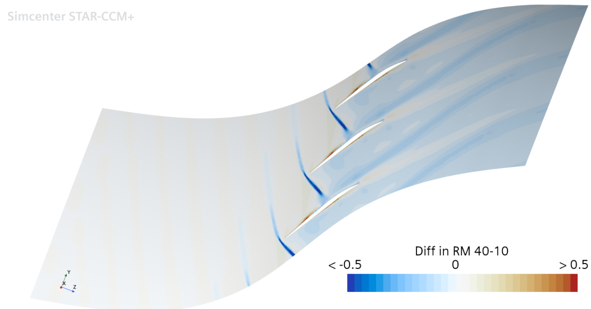

(a) Case 2 and 3 (40 kPa and 10 kPa)

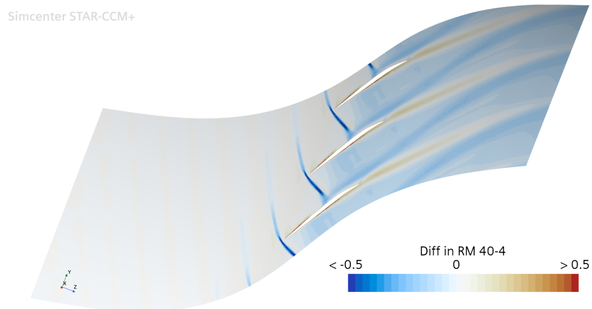

(b) Case 2 and 4 (40 kPa and 4 kPa)

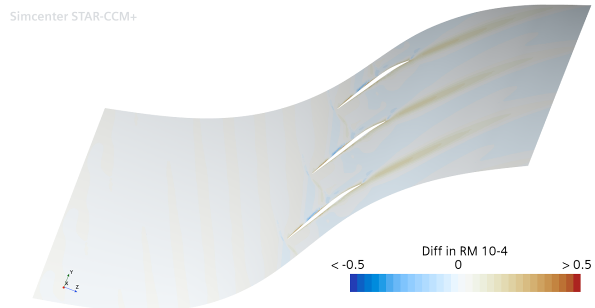

(c) Case 3 and 4 (10 kPa and 4 kPa)

Figure A.1.3: Relative Mach differences on 90% span

The differences between the cases 2 and 3; 2 and 4; 3 and 4, in relative Mach number for the Meridional plane, are depicted in Figure A.1.4.

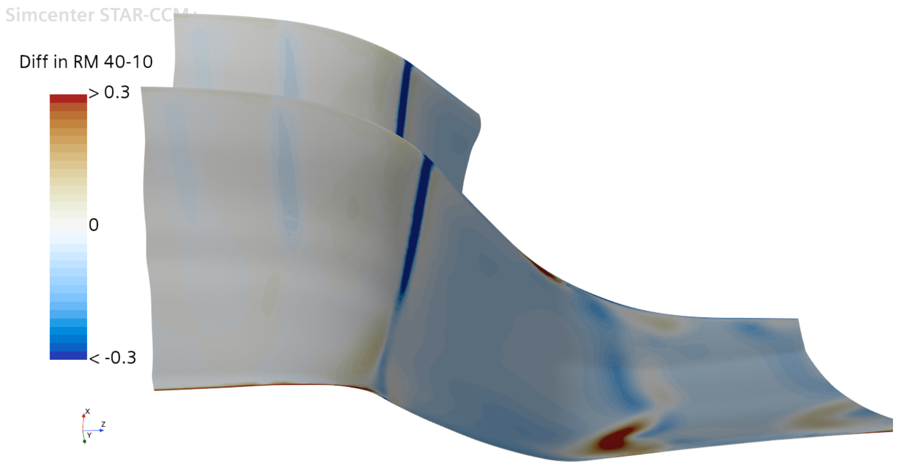

(a) Case 2 and 3 (40 kPa and 10 kPa)

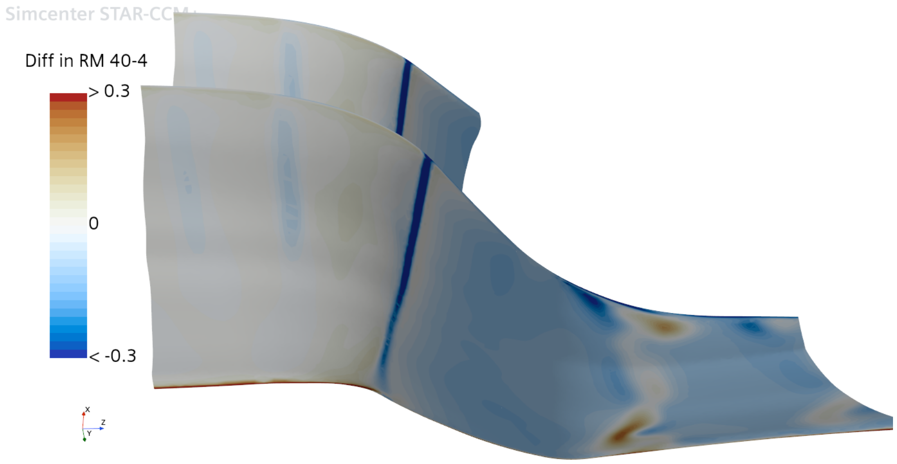

(b) Case 2 and 4 (40 kPa and 4 kPa)

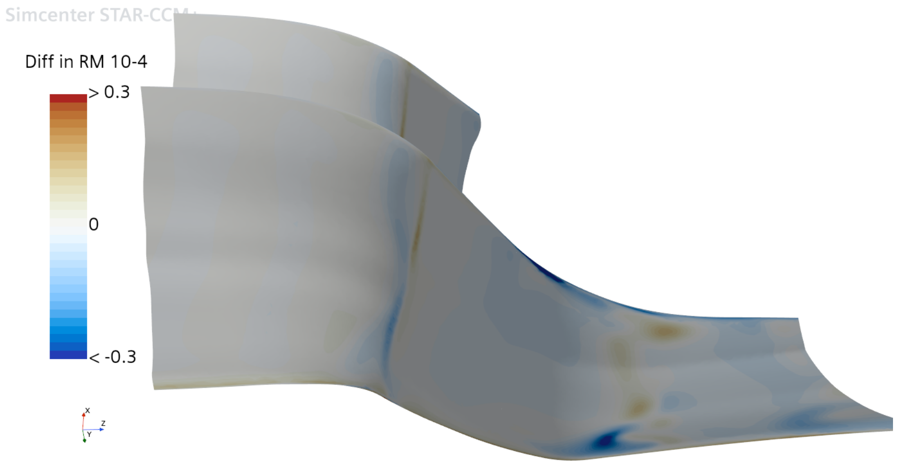

(c) Case 3 and 4 (10 kPa and 4 kPa)

Figure A.1.4: Relative Mach differences on the Meridional plane

A.2 Intermittency contour plots

As previously explained the intermittency contour depends on the turbulence model, k - ω SST, and the transition model used, γ - $Re_{\theta t}$ Gamma ReTheta model. The intermittency represents the flow regime, values close to 0 correspond to near laminar flow, while fully turbulent flow correspond to an intermittency near 1. This extra figures are of relevance to understand the flow regime evolution across the span. The contour plots of intermittency are obtained for the four operational pressure cases, in order to quantify the nature of the boundary layer around the blade. First the intermittency is shown for the 10% span plane in Figure A.2.1 and for the 90% span plane in Figure A.2.2.

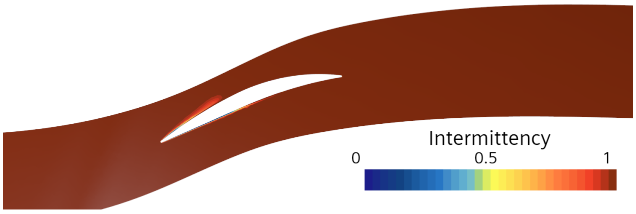

(a) Case 1 (100 kPa)

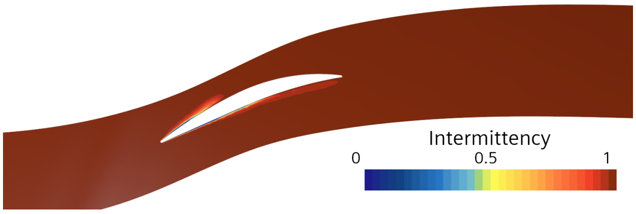

(b) Case 2 (40 kPa)

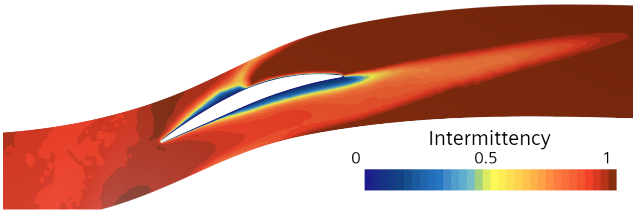

(c) Case 3 (10 kPa)

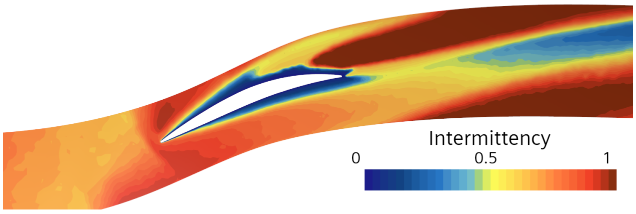

(d) Case 4 (4 kPa)

Figure A.2.1: Intermittency on 10% span

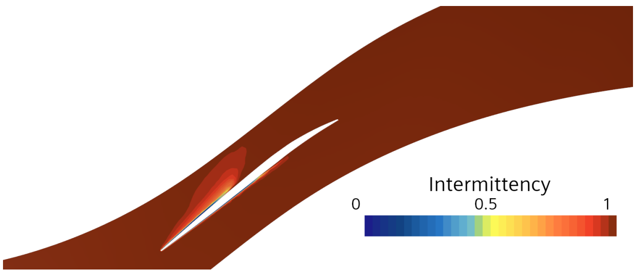

(a) Case 1 (100 kPa)

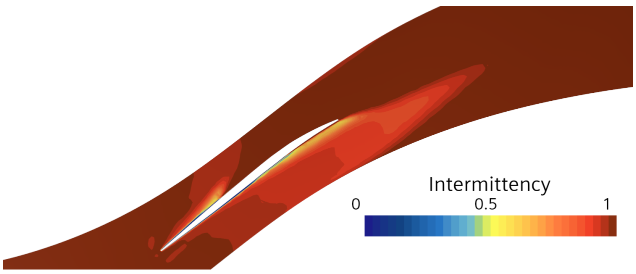

(b) Case 2 (40 kPa)

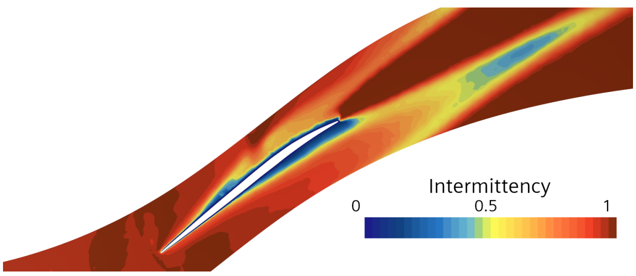

(c) Case 3 (10 kPa)

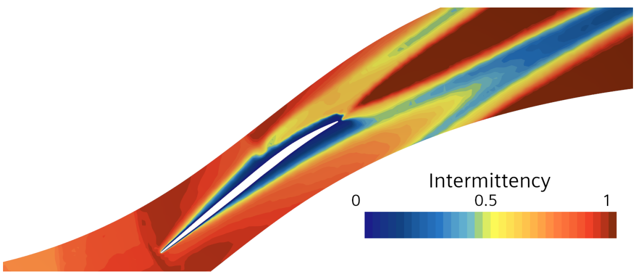

(d) Case 4 (4 kPa)

Figure A.2.2: Intermittency on 90% span

A.3 Flow coefficient parameters

Now the different flow coefficients are depicted together for all the possible span sections (10%, 50% and 90%). The the joint display allows a qualitative comparison between the sections, which wasn't possible in section 4.

First the pressure coefficient is depicted for all the different blade spans in Figure A.3.1.

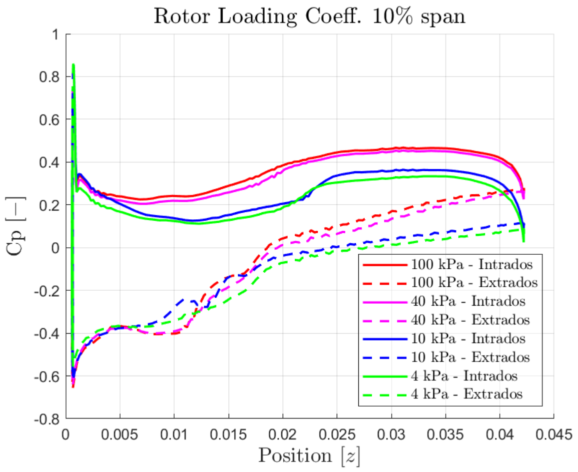

(a) 10% span

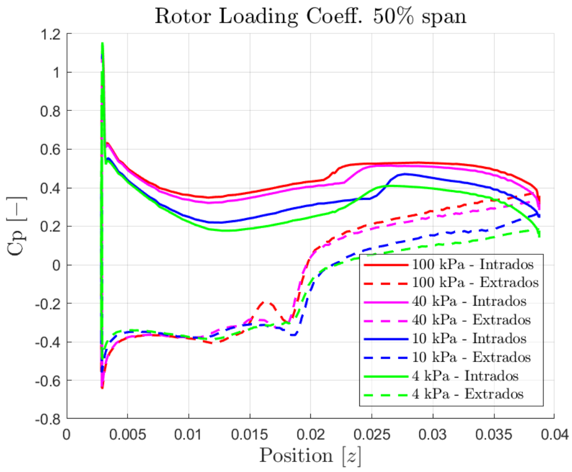

(b) 50% span

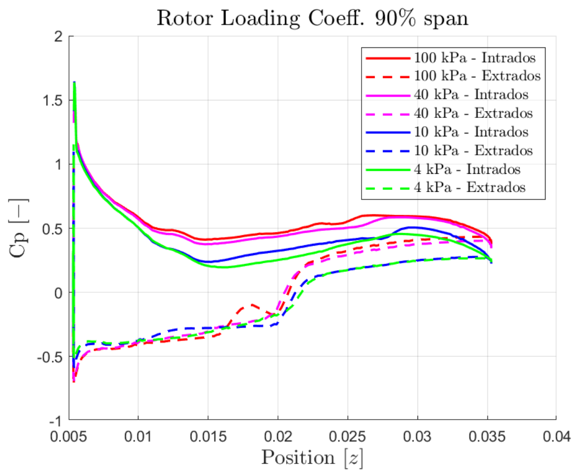

(c) 90% span

Figure A.3.1: Pressure coefficient on the span plane

Now the plots of the skin friction coefficient are shown for all the different blade spans in Figure A.3.2.

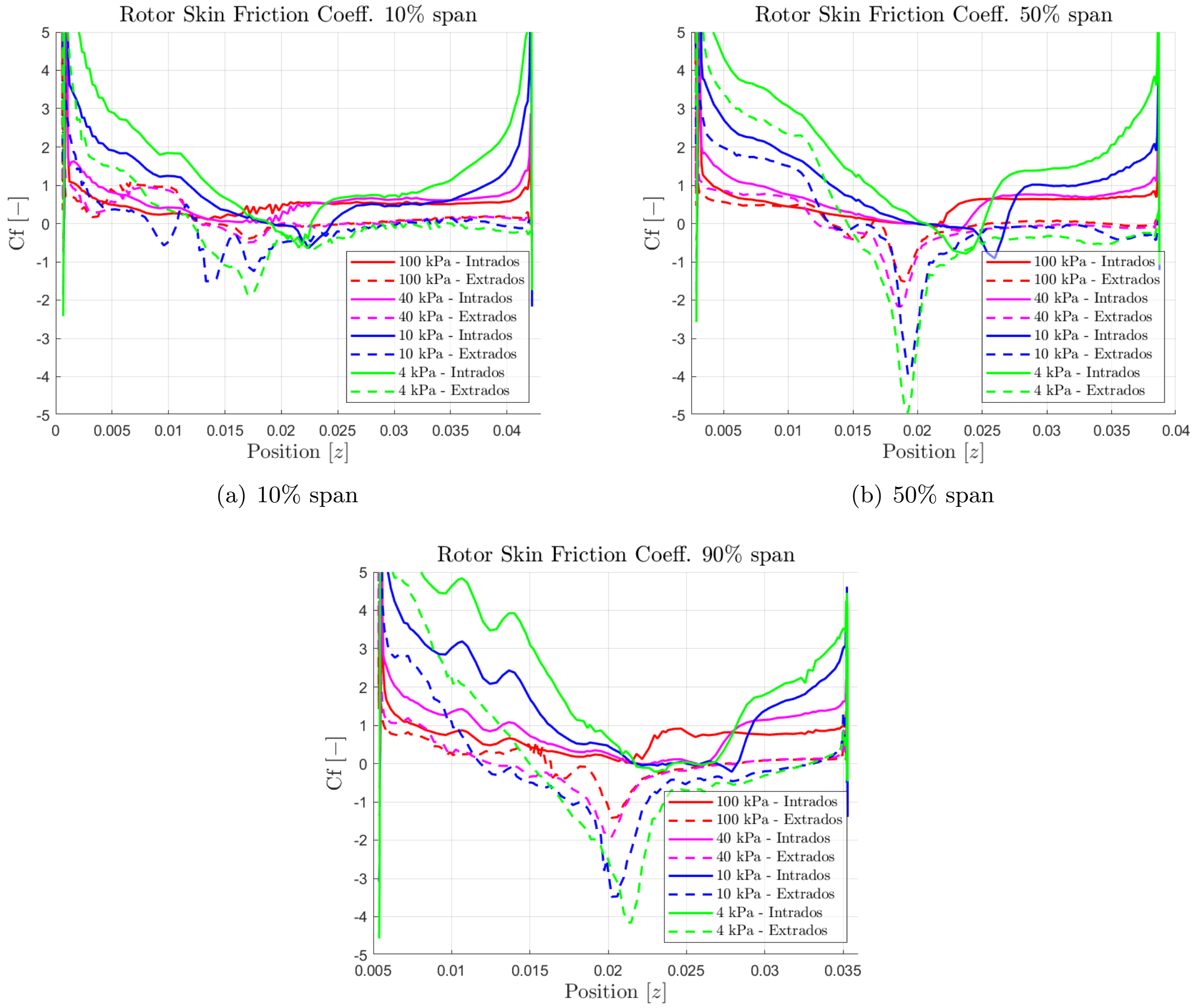

(a) 10% span

(b) 50% span

(c) 90% span

Figure A.3.2: Skin friction coefficient on the span plan

Finally, the plots of the intermittency are shown for all the different blade spans in Figure A.3.3.

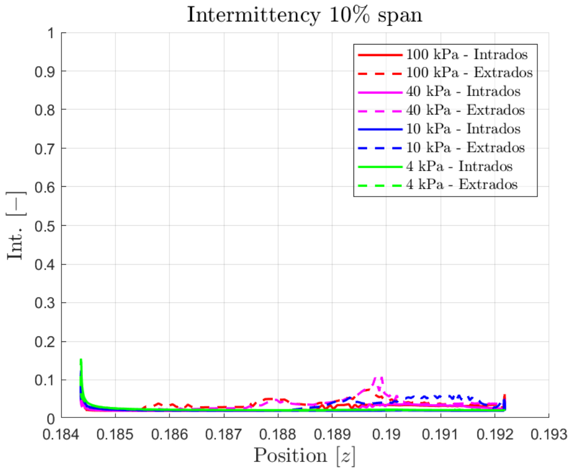

(a) 10% span

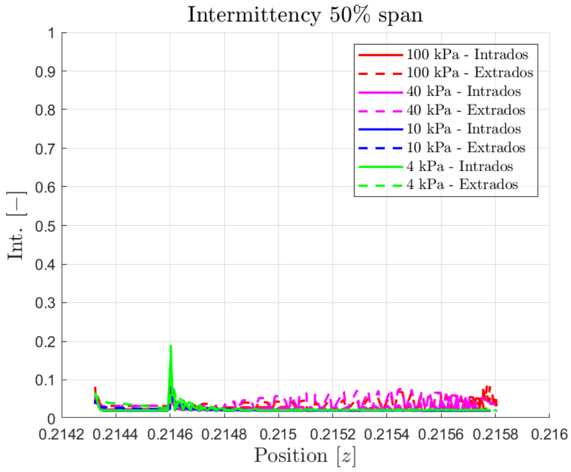

(b) 50% span

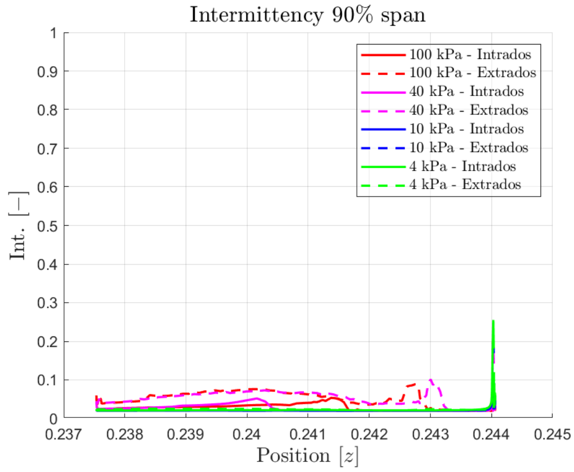

(c) 90% span

Figure A.3.3: Intermittency on the span planes

To complete this section Figure A.3.4 shows the hole Mach differences figures together, to be able to make an easier analysis between them.

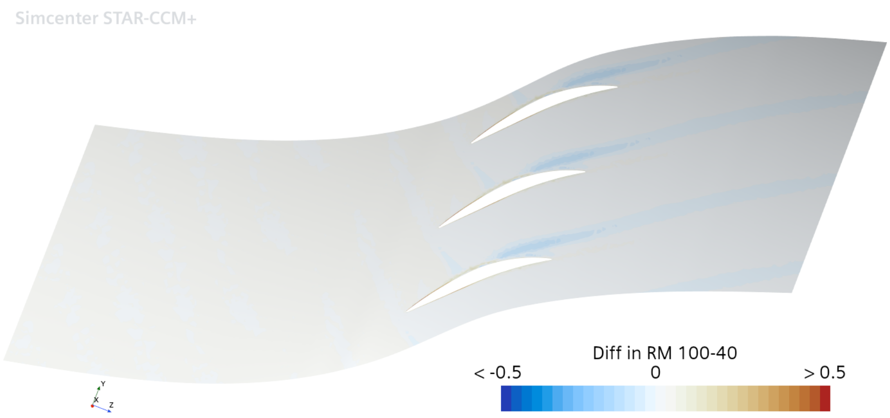

(a) Case 1 and 2 (100 kPa and 40 kPa)

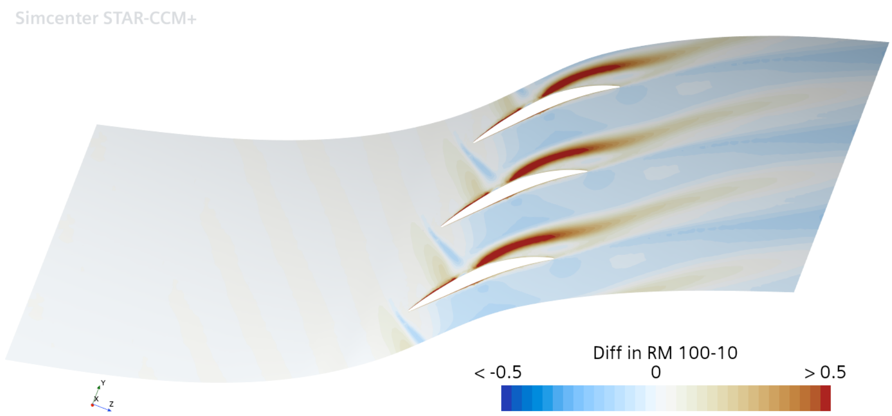

(b) Case 1 and 3 (100 kPa and 10 kPa)

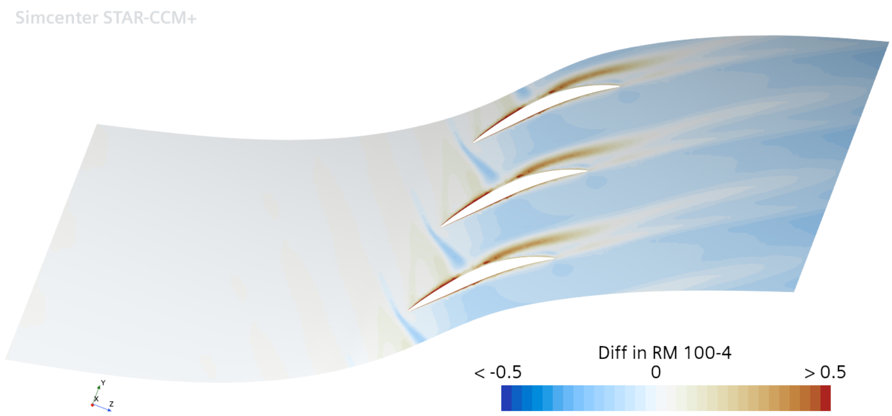

(c) Case 1 and 4 (100 kPa and 4 kPa)

Figure A.3.4: Relative Mach differences on 50% span

B Sustainable Development Goals

The following appendix section sum ups the alignment between the project and the Sustainable Development Goals (SDGs):

The initiative presented in this project demonstrates a significant connection with the SDGs outlined in the Agenda 2030. Specifically on the following goals: SDG 9 (Industry, Innovation, and Infrastructure), SDG 11 (Sustainable Cities and Communities) and SDG 13 (Climate Action). Medium connection is consider with: SDG 8 (Decent Work and Economic Growth). Lower connection is consider with: SDG 3 (Good Health and well-living).

The project focus on the development of an efficient, non pollutant, and economic mean of transport, which aligns with innovation and industry evolution. Promoting sustainability inside the cities and communities, industrial innovation and a solution to mitigate climate change.

Additionally, it is expected to create numerous occupations, thereby boosting economy, while also improving the well-living and connectivity of people. Therefore, the project has links with creating decent jobs and economic growth, and also with enhancing the health and well-living in the society.

The development of the mean of transport introduced in this project, main objective is to become a feasible initiative to tackle one of the biggest challenges which humanity faces, climate change.

Table B.0.1 sum up the level of connection between the project and the Sustainable Development Goals (SDGs):

Sustainability Development Goals	**High**	**Medium**	**Low**	**N/A**
SDG 1. No poverty.				**X**
SDG 2. Zero hunger.				**X**
SDG 3. Good Health and well-living.			**X**	
SDG 4. Quality Education.				**X**
SDG 5. Gender equality.				**X**
SDG 6. Clean water and sanitation.				**X**
SDG 7. Affordable and clean energy.				**X**
SDG 8. Decent work and economic growth.		**X**		
SDG 9. Industry, innovation, and infrastructures.	**X**			
SDG 10. Reduced inequalities.				**X**
SDG 11. Sustainable cities and communities.	**X**			
SDG 12. Responsible consumption and production				**X**
SDG 13. Climate action.	**X**			
SDG 14. Life below water.				**X**
SDG 15. Life on land.				**X**
SDG 16. Peace, justice, and strong institutions.				**X**
SDG 17. Partnership for the goals.				**X**

Table B.0.1: Table for the Sustainability Development Goals

C Drawings

Since the geometry is already explained in subsubsection 3.1.1, **no drawings are included in this project**. Furthermore, the complex geometry used to build NASA Rotor 37 requires the use MCA parameters through a complex algorithm. Therefore, it's shape can not accurately be outlined in a drawing. This algorithm is printed using Fortran IV program, where it is implemented. The parametrization and algorithm implementation is described by James E. Crouse et al. in [28].

The blade geometry is then obtained by a series of blade sections at different spans and positions. Consequently a drawing won't be effective when representing the blade geometry, whereas a parametrization yes. Therefore the parameters used to create the MCA blade sections are depicted in the succeeding section.

C.1 Geometric parametrization of NASA Rotor 37

Figure C.1.1 shows the an axial cut of the blade, including the position and length of the blade sections and the parameters used on the algorithm for their generation. The parameter used are:

- r_{ic}: radial distance to the leading edge point.
- r_{oc}: radial distance to the trailing edge point.
- κ_{ic}: camber angle at the leading edge point*.
- κ_{tc}: camber angle at the transition point*.
- κ_{oc}: camber angle at the trailing edge point*.
- t_i: blade thickness at the leading edge point.
- t_m: blade thickness at the maximum thickness point.
- t_o: blade thickness at the trailing edge point.
- z_{ic}: axial distance to the leading edge point.
- z_{mc}: axial distance to the maximum thickness point.
- z_{tc}: axial distance to the transition point.
- z_{oc}: axial distance to the trailing edge point.

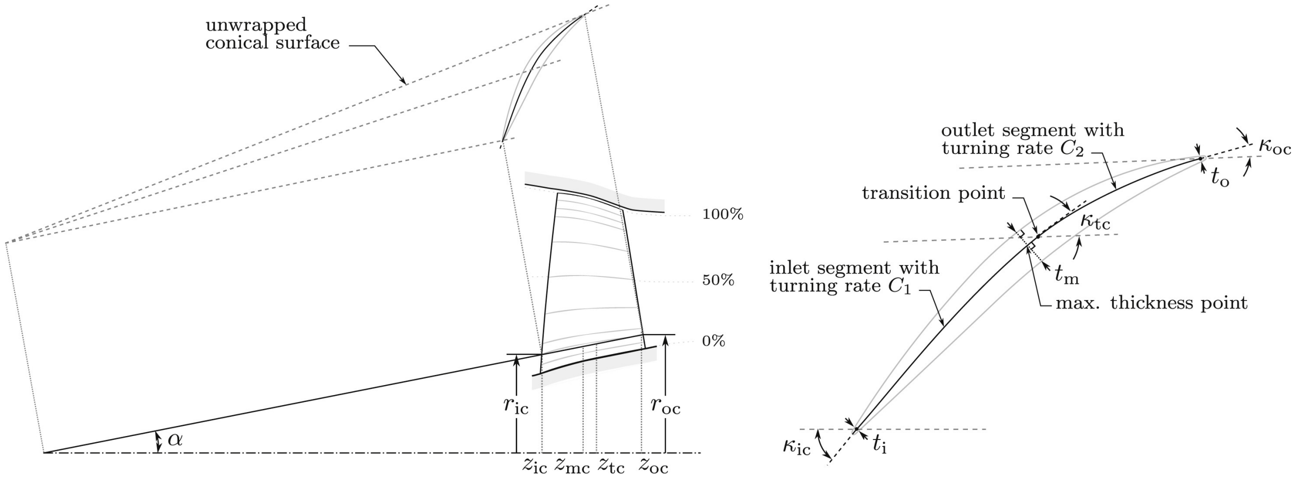

Figure C.1.1: Multiple circular arc parameterization [29]

*Note that the angles are measured with respect to the axis of rotation direction.

Table C.1.1 shows the values that the parameters previously explained take on the different spans of the rotor. This spans are closer near the hub and the shroud, to have a higher resolution on those points, where the blade has greater shape gradients. Whereas, the span is distant at the half of the blade, where lower resolution is needed.

% span	r_{ic} (cm)	r_{oc} (cm)	κ_{ic} (deg)	κ_{tc} (deg)	κ_{oc} (deg)	t_i (cm)	t_m (cm)	t_o (cm)	$z_{mc} - z_{ic}$ (cm)	$z_{tc} - z_{ic}$ (cm)	$z_{oc} - z_{ic}$ (cm)
100	25.230	24.502	62.246	62.480	50.008	0.025	0.175	0.025	1.719	1.725	2.672
95	24.935	24.218	61.651	61.861	49.100	0.026	0.186	0.026	1.721	1.705	2.759
90	24.597	23.932	60.988	61.162	48.180	0.027	0.199	0.028	1.726	1.687	2.846
85	24.254	23.644	60.334	60.421	47.242	0.029	0.211	0.029	1.734	1.672	2.933
70	23.211	22.774	58.470	57.953	44.176	0.032	0.250	0.033	1.769	1.643	3.187
50	21.761	21.622	56.190	54.212	39.090	0.037	0.303	0.038	1.834	1.631	3.517
30	20.246	20.468	54.204	50.406	32.168	0.042	0.360	0.043	1.899	1.627	3.836
15	19.030	19.602	52.910	47.831	25.329	0.047	0.407	0.047	1.932	1.608	4.068
10	18.603	19.313	52.520	47.061	22.666	0.048	0.424	0.049	1.936	1.594	4.143
5	18.161	19.026	52.152	46.367	19.805	0.050	0.442	0.050	1.936	1.575	4.218
0	17.780	18.740	51.864	45.837	16.726	0.051	0.459	0.051	1.932	1.553	4.292

Table C.1.1: Multiple-circular-arc parameters for the 11 profiles of the reference blade [29]

$z_{mc} - z_{ic}$ correspond to the axial distance between the leading edge and the maximum thickness points. Whereas, $z_{tc} - z_{ic}$ correspond to the axial distance between the leading edge and the transition points and $z_{oc} - z_{ic}$ correspond to the axial distance between the leading edge and the trailing edge points.

D Cost Estimates

On this section the approximated cost estimates for the project development are exposed. The accounts will be subdivided into the following sections: direct costs, general costs, benefits and the total cost estimate, where the VAT is added.

D.1 Direct costs

The direct cost can be subdivided at the same time into human resources, equipment costs and software and licenses costs.

Human resources costs

On this calculation people involved in this project and their respective salaries are accounted. The author of the project, the student, is considered as a Junior Engineer. According to [30] the mean net salary for a junior engineer in Spain in the year 2024 is 12.82 €/hour. On the other hand, the cost related to the Tutor and Co-Tutor, is considered the net salary of a senior engineer [31], which is around 19.23 €/hour. To obtain the gross salary from the net salary a 30% should be added, and to get the direct company cost an extra 40% is added. Therefore the approximated final salaries that the company pays are shown in Table D.1.1.

Costs description	Time [h]	Salary [€/hour]	Cost [€]
Student	300	23.33	7000
Tutor	20	35.00	700
Co-Tutor	20	35.00	700
		Total	**8400**

Table D.1.1: Human resources cost estimation

Equipment costs

On this account related to the equipment costs three items are exposed. The laptop is a HP Pavilion Gaming Laptop 15-ec2xxx, with a cost an approximated cost of 800 €. Expecting a mean lifespan of 4 years [32], with a mean usage of 5 daily hours, the total lifespan of the computer in hours will be of 7200 hours. Diving the cost by the lifespan in hours the cost per hour is obtained. The consumption of a laptop is estimated to be 0.0208 €/h [33], assuming an energy cost of 0.2966 €/kWh [34]. Finally the cluster cost is estimated to be around 0.1 €/(Core · Hour) [35], and 20 cores are assumed to be used. With this insight the equipment cost are computed in Table D.1.2.

Costs description	Time [h]	Price [€/hour]	Cost [€]
Laptop	500	0.111	55.6
Laptop consume	500	0.021	10.4
Cluster cost	200	2	400.0
		Total	**466**

Table D.1.2: Equipment cost estimation

Software and Licenses costs

In this account the software's and licenses required are exposed. The STAR CCM+ license is estimated to have a cost of 0.1 €/(h·CPU), this cost is private and depends on the customer needs. Assuming that 8 CPUs are used on the simulations a cost of 0.8 €/h is estimated. Matlab license for student has a cost of 262 €/year, the Microsoft Office Package has an cost of 69 €/year and Overleaf cost for students is 79 €/year. Note than some units of Table D.1.3 are in hours and others in years.

Costs description	Time	Price	Cost [€]
STAR CCM+	200 hours	0.8 €/hour	160.0
Matlab License	0.5 years	262 €/year	131.0
Microsoft Office Package	0.5 years	69 €/year	34.5
Overleaf	0.5 years	79 €/year	39.5
		Total	**365**

Table D.1.3: Software and Licenses costs estimation

Total direct cost

Finally the totality of the direct cost are summed up in Table D.1.4.

Costs description	Cost [€]
Human resources	8400
Equipment	466
Software and Licenses	365
Total	**9231**

Table D.1.4: Total direct cost estimation

D.2 General costs

On this section the indirect costs related to the project are exposed. As human resources have been already accounted in the previous section, on this one the only the cost related to the workplace will be accounted. For the indirect costs 20% overheads coefficient is estimated over the direct costs, this percentage is estimated for a engineering company. Table D.2.1 sums up the accounts related to the indirect costs and direct costs.

Costs description	Cost [€]
Direct costs	9231
Overheads Coefficient	+20%
Total	**11077**

Table D.2.1: General cost estimation

D.3 Benefits

Furthermore, a benefit percentage must be set in order to provide and appeal for the company owner or project investors. There is no reason to invest, assuming a risk, without a benefit. Therefore a benefit of 7% is established over the general costs. Table D.3.1 sums up the benefits costs for this project.

Costs description	Cost [€]
General costs	11077
Benefit percentage	+7%
Total	**11853**

Table D.3.1: Benefits estimation

D.4 Total costs

Finally the total project costs for the customer are showed in Table D.4.1, where all the cost are broke down. On this table a 21% VAT tax is added to the final price. Is worthy to note that this cost estimation is focused towards the client final price, accounting for every type of needed resource. Note that the extra money that the percentage represents is shown at the right of it in brackets.

Costs description	**Cost [€]**
Human resources	8400
Equipment	466
Software and Licenses	365
Direct costs	9231
Overheads Coefficient	+20% (1846 €)
General costs	11077
Benefit percentage	+7% (775 €)
Total income	11853
VAT	+21% (2489 €)
Quotation	**14342**

Table D.4.1: General cost estimation

The final total cost for the client after taxation will be: **14342 €**.

E Articles and Conditions

This section describes the technical and operative specifications needed to study the performance of the NASA Rotor 37 under different pressures of operation using CFD simulations. This Final Degree Project will focus on the on the validation and comparison of the flow patterns and effects that appear at low pressure of operation. The final objective is to bring insight into the development of a Hyperloop transportation system. On this section the legal conditions will be exposed, before each article a brief explanation of the accomplishment of the legislation will be included. Note that this work was conducted on the CMT installations on building 6D, inside the UPV.

E.1 Legal Conditions

It is legally required to follow the conditions specified in the Real Decreto 486/1997, where the minimum requisites for security and healthiness are accomplished. It is required a proper workplace where the security and comfort conditions are meet to achieve a good performance.

Furthermore, since the project requires the use of informatics equipment, the Real Decreto 488/1997 should be enforced, ensuring that the minimum security and healthy conditions are accomplished, in a work that requires the use of visualization screens. Also the minimum hardware and software requirements for this project will be specified.

E.1.1 Workplace conditions

The legislation regarding the workplaces is regulated in the Real Decreto 486/1997 of the 14th of April, where the minimum health and security conditions are stipulated. The Real Decreto 488/1997, specifies the legislation regarding the work with screens.

Workplace conditions

Regarding the workplace, sufficient space should provided to ensure the comfort and productivity of the worker. The workplace should ensure the following minimum conditions.

- *Three meters high from floor to ceiling.*
- *Two square meters of workplace.*
- *Ten cubic meters of workplace.*

Security conditions

The implementation of evacuation paths on the workplace should be implemented in the workplace, including emergency routes and exits. It is important to communicate the evacuation plans to the workers.

With respect to the fire security, the competent body should authorize companies for the design, implementation and maintenance of the fire extinction installations on the workplace. This prevention will be combined with the general protection provided by the public fire extinguish services.

Regarding the electric installation on the workplace, it should be designed and maintained by an authorized company, accomplishing with the current electricity regulations.

All the permanent or provisional buildings, will be of firm and secure construction, avoiding structural collapse under extreme atmospheric conditions. The maximum allowable weight supported will be indicated among the building, being strictly prohibited to overload the structure.

The security conditions are accomplished in the building 6D, regarding both evacuation routes and fire and electric installations.

Ambient conditions

The Real Decreto 488/1997 establishes that the following ambient conditions to guarantee a correct thermal sensation for workers: a temperature between 23ºC and 26ºC in summer and between 20ºC and 24ºC in winter. Moreover, the relative humidity of the air should be between 45% and 65%.

The environmental carbon dioxide, should overpass the 50/10000 proportion, and the carbon monoxide should be lower to 1/10000 proportion. Moreover, a proper ventilation should be accomplish, with at least 30 cubic meters of air ventilated in during an hour.

Regarding the illumination it can be natural or artificial, although is recommended natural light. Natural illumination should be accompanied with artificial light to avoid glare and excessive contrasts. Also, the location of the screens should avoid reflects and glare on the workplace.

The building 6D provides the sufficient ambient comfort and illumination for a correct work development.

Ergonomics: Workplace design

The workplace should be properly conditioned to avoid posture problems due to the use of screens during work.

- ***Seat:*** *Adjustable seat height, with a proper backrest. Is recommended the use of a wheelchair.*
- ***Table:*** *A sufficiently wide and conditioned table without reflexes.*
- ***Screen position:*** *optimal distance of 45-75 cm at a correct angle.*
- ***Screen:*** *Stable image, with the proper luminosity and contrast.*
- ***Keyboard:*** *Proper size for the project drafting.*
- ***Individual protection equipment:*** *Screen protectors are recommended.*

The building 6D provides the proper equipment for a correct posture while working making use of screens.

Noise

Regarding the noise, certain noise levels should be accomplish as established in the Real Decreto 1316/1989. The noise level should as low as possible not exceeding 55 dB, for work that requires concentration.

On the building 6D, the noise levels where proper for the correct development of the project, ensuring a good concentration.

E.1.2 Computer resources conditions

For the CFD simulations and configuration, the use of high performance computer resources is needed and regulated on the Decreto Real 488/1997. The computer resources divided into hardware and software.

Hardware conditions

High performance computer equipment is required for the calculation of the CFD simulations, in this case the laptop model is: HP Pavilion Gaming Laptop 15-ec2xxx. Therefore, the hardware should include a proper calculation tool with sufficient memory and a decent maintenance. The hardware details are specified below.

- **Laptop model:** HP Pavilion Gaming Laptop 15-ec2xxx
- **Processor:** AMD Ryzen 7 5800H, 3201 MHz, 8 cores, 16 logical processes
- **RAM memory:** 16 GB
- **Graphic card:** NVIDIA GeForce GTX 1650, 12 GB
- **Memory:** SSD, 500 GB
- **Operative system:** W/indows 11 Home 64 bits

Software conditions

The following software is used in the calculations, edition and presentation of the project:

- **CFD Software:** Simcenter STAR-CCM+ 2310 (18.06.006-R8)
- **Post-processing Software:** MATLAB R2023b
- **Report Software:** Overleaf
- **Report and Post-processing Software:** Microsoft Office Package (Excel and PowerPoint)

E.2 CFD Configuration

Finally on the following pages the report of the CFD configuration is showed. Just one of the four cases configuration is exposed, since the boundary conditions, models and scenes are similar across all the cases. Case 1, 100 kPa, configuration is displayed, since is considered as the first and reference case, and it includes the biggest part of post-processing.

E.2.1 Configuratio Report of Case 1 (100 kPa)

Summary Report: F3-Rotor37_100_Des_GTLowMachRefp100

Session Summary	
File size	1,4e+03 MB
Number of Partitions	2
Number of Restored Partitions	7
Software Summary	
Version	BuildArch: win64 BuildEnv: clang15.0vc14.2-r8 PresentationVersion: 2310 ReleaseDate: Wed Oct 4 13:05:35 UTC 2023 ReleaseNumber: 18.06.006
MPI Version	MS MPI-10.1.12498.16
Hardware Summary	
Hosts	Number Processes: 2 Rank[0]: LAPTOP-VEU67S9V Rank[1]: LAPTOP-VEU67S9V

Simulation Properties

1 **F3-Rotor37_100_Des_GTLowMachRefp100**		
+-1 Continua	Continua	1
| `-1 **Physics 1**	Regions	[R37_SI]
| |	Interfaces	[Interface 1]
| |	Point Sets	[]
| |	Active	true
| |	Motion Always Active	false
| |	Tags	[]
| +-1 Models		
| | +-1 All y+ Wall Treatment	Iterative Ustar	false
| | +-2 Coupled Energy	Enthalpy Formulation	false
| | |	Flow Boundary Diffusion	true
| | +-3 Coupled Flow	Integration	IMPLICIT
| | |	Positivity Rate Limit	0.2
| | |	Preconditioning Enabled	true
| | |	Unsteady Low-Mach Preconditioning	true
| | |	Unsteady Preconditioning Max Factor	0.95
| | |	Pressure Difference Scale Factor	2.0
| | |	Minimum Reference Velocity	1.0E-10 m/s
| | |	Maximum Reference Velocity	1000000.0 m/s
| | |	Flow Boundary Diffusion	true
| | |	Secondary Gradients	On
| | |	Coupled Inviscid Flux	Roe FDS
| | |	Discretization	2nd-order
| | +-4 Gamma-ReTheta Transition	Sigma_f	1.0
| | |	ca2	0.06
| | |	ce2	50.0
| | |	Intermittency Minimum	1.0E-10
| | |	Secondary Gradients	On
| | |	Convection	2nd-order
| | |	Cross-Flow Term	false
| | |	Correlation Method	Suluksna-Juntasaro
| | |	Sigma_ReTheta	2.0
| | |	ca1	2.0
| | |	ce1	1.0
| | |	cTheta_t	0.03
| | |	s1	2.0
| | |	Conset1	2.193
| | |	ReThetaT Minimum	20.0
| | +-5 Gas		
| | | `-1 **Air**	Database Material	Air (Air) [Standard/Gases]
| | | |	Tags	[]
| | | `-1 Material Properties		

+-1 Dynamic Viscosity	Method	Constant
`-1 Constant	Value	1.85508E-5 Pa-s
+-2 Molecular Weight	Method	Constant
`-1 Constant	Value	28.9664 kg/kmol
+-3 Specific Heat	Method	Constant
`-1 Constant	Value	1003.62 J/kg-K
+-4 Thermal Conductivity	Method	Constant
`-1 Constant	Value	0.0260305 W/m-K
`-5 Turbulent Prandtl Number	Method	Constant
`-1 Constant	Value	0.9
+-6 Gradients	Boundary Cell Eigenvalues Ratio Tolerance	0.06
	Limit GradVar By Beta	true
	Limiter Method	Venkatakrishnan
	Custom Accuracy Level Selector	2.0
	Maximum Reconstruction Coefficient	1.0
	Two Pass Velocity Gradient	false
	Use TVB Gradient Limiting	false
	Acceptable Field Variation (Factor)	0.05
+-7 Ideal Gas	Incompressible	false
	Density Limiting	false
+-8 K-Omega Turbulence		
+-9 Reynolds-Averaged Navier-Stokes		
+-10 Solution Interpolation	Per Part Mapping	false
	Interpolation Method	Nearest neighbor
	Legacy Method	false
	Conservation Correction	Disable
+-11 SST (Menter) K-Omega	Curvature Correction Option	Off
	Realizability Option	Durbin Scale Limiter
	Compressibility Correction	true
	Low Re Damping Modification	false
	Convection	2nd-order
	Normal Stress Term	false
	Tke Minimum	1.0E-10
	Sdr Minimum	1.0E-10
	Secondary Gradients	On
	Kappa	0.41
	BetaStar	0.09
	Beta1	0.075
	Sigma_k1	0.85
	Sigma_w1	0.5
	Beta2	0.0828
	Sigma_k2	1.0
	Sigma_w2	0.856
	Constitutive Option	Linear
	a1	0.31
+-1 Compressibility Parameters	Zeta_Star	1.5
`-2 Realizability Coefficient	Realizability Coefficient	0.6
+-12 Steady	Continuum Iteration	189481
+-13 Three Dimensional		
+-14 Turbulent		
`-15 Wall Distance	Wall Distance Method	Implicit Tree
+-2 Reference Values		
+-1 Reference Pressure	Value	0.0 Pa
+-2 Minimum Allowable Wall Distance	Value	1.0E-6 m
+-3 Maximum Allowable Absolute Pressure	Value	1.0E8 Pa
+-4 Minimum Allowable Temperature	Value	100.0 K
+-5 Minimum Allowable Absolute Pressure	Value	1000.0 Pa
`-6 Maximum Allowable Temperature	Value	5000.0 K
`-3 Initial Conditions		
+-1 Intermittency	Method	Constant
`-1 Constant	Value	1.0
+-2 Pressure	Method	Constant
`-1 Constant	Value	120000.0 Pa

| +-3 Static Temperature	Method	Constant
| | `-1 Constant	Value	288.15 K
| +-4 Turbulence Intensity	Method	Constant
| | `-1 Constant	Value	0.01
| +-5 Turbulence Specification	Method	Intensity + Viscosity Ratio
| +-6 Turbulent Velocity Scale	Method	Constant
| | `-1 Constant	Value	1.0 m/s
| +-7 Turbulent Viscosity Ratio	Method	Constant
| | `-1 Constant	Value	10.0
| `-8 Velocity	Method	Constant
| |	Coordinate System	Laboratory
| `-1 Constant	Value	[0.0, 0.0, 10.0] m/s
+-2 Interfaces	Debug Obj Files	false
| |	Multithreading	Automatic
| |	Verbosity	false
| |	Contact Selection Priority	[Interface 1]
| |	Overset Hierarchy	[]
| |	Interfaces	1
| |	Direct Intersector	Geometry-Based (Legacy)
| `-1 **Interface 1**	Close on Fixed Side	false
| |	Geometry	Boundaries
| |	Boundary-0	R37_SI: R37.Per2
| |	Boundary-1	R37_SI: R37.Per1
| |	Contacts	[]
| |	Type	Internal Interface
| |	Topology	Periodic
| |	Connectivity	Imprinted
| |	Allow Per-Contact Values	false
| |	Close Adjacent Cells	false
| |	Reset on Relative Motion	false
| |	Tags	[]
| +-1 Periodic Transformation	Periodicity	Rotational+Translational
| |	Axis of Rotation Specification	Use region's reference axis
| |	Rotation Angle (deg)	10.000006132595436
| |	Translation (m)	[0.0, 0.0, 0.0]
| |	Locked	false
| `-2 Physics Values		
| `-1 Intersection	Specify by Part Subgroup	false
| `-1 Intersection tolerance	Match Outer Boundary	false
|	Projection Tolerance	0.2
|	Angle Threshold	45.0
|	Conformal Tolerance	0.01
|	Nonconformal Tolerance	0.01
|	Geometric Tolerance	0.05
+-3 Regions	Part Selection Priority	[R37_SI]
| |	Regions	1
| `-1 **R37_SI**	Index	8
| |	Allow Per-Part Values	false
| |	Physics Continuum	[Physics 1]
| |	Parts	[R37]
| |	Type	Fluid Region
| |	Topology	VOLUME
| |	Tags	[]
| +-1 Boundaries	Part Surface Selection Priority	[R37_SI: R37.Per2, R37_SI: R37.Per1, R37_SI: R37.Outlet, R37_SI: R37.Shroud, R37_SI: R37.Inlet, R37_SI: R37.Hub, R37_SI: R37.Blade_Intrados, R37_SI: R37.Blade_Extrados, R37_SI: R37.Per2 [Interface 1], R37_SI: R37.Per1 [Interface 1]]
| | |	Boundaries	10
| | +-1 **R37.Blade_Extrados**	Index	73
| | | |	Interfaces	
| | | |	Part Surfaces	[R37.Blade_Extrados]
| | | |	Type	Wall
| | | |	Allow Per-Surface Values	false
| | | |	Topology	SURFACE
| | | |	Tags	[]
| | | +-1 Physics Conditions		
| | | | +-1 Reference Frame Specification	Option	Region Reference Frame
| | | | +-2 Shear Stress Specification	Method	No-Slip
| | | | +-3 Tangential Velocity Specification	Method	Fixed
| | | | +-4 Thermal Specification	Condition	Adiabatic
| | | | +-5 User Wall Heat Flux Coefficient Specification	Method	None
| | | | `-6 Wall Surface Specification	Method	Smooth
| | | `-2 Physics Values		

`-1 Blended Wall Function	E	9.0
	Kappa	0.42
+-2 **R37.Blade_Intrados**	Index	72
	Interfaces	
	Part Surfaces	[R37.Blade_Intrados]
	Type	Wall
	Allow Per-Surface Values	false
	Topology	SURFACE
	Tags	[]
+-1 Physics Conditions		
+-1 Reference Frame Specification	Option	Region Reference Frame
+-2 Shear Stress Specification	Method	No-Slip
+-3 Tangential Velocity Specification	Method	Fixed
+-4 Thermal Specification	Condition	Adiabatic
+-5 User Wall Heat Flux Coefficient Specification	Method	None
`-6 Wall Surface Specification	Method	Smooth
`-2 Physics Values		
`-1 Blended Wall Function	E	9.0
	Kappa	0.42
+-3 **R37.Hub**	Index	71
	Interfaces	
	Part Surfaces	[R37.Hub]
	Type	Wall
	Allow Per-Surface Values	false
	Topology	SURFACE
	Tags	[]
+-1 Physics Conditions		
+-1 Reference Frame Specification	Option	Region Reference Frame
+-2 Shear Stress Specification	Method	No-Slip
+-3 Tangential Velocity Specification	Method	Fixed
+-4 Thermal Specification	Condition	Adiabatic
+-5 User Wall Heat Flux Coefficient Specification	Method	None
`-6 Wall Surface Specification	Method	Smooth
`-2 Physics Values		
`-1 Blended Wall Function	E	9.0
	Kappa	0.42
+-4 **R37.Inlet**	Index	70
	Interfaces	
	Part Surfaces	[R37.Inlet]
	Type	Mass Flow Inlet
	Allow Per-Surface Values	false
	Topology	SURFACE
	Tags	[]
+-1 Physics Conditions		
+-1 Flow Direction Specification	Method	Boundary-Normal
+-2 Mass Flow Option	Specification Option	Mass Flow Rate
+-3 Reference Frame Specification	Option	Lab Frame
`-4 Turbulence Specification	Method	Intensity + Viscosity Ratio
`-2 Physics Values		
+-1 Mass Flow Rate	Method	Constant
`-1 Constant	Value	0.546311 kg/s
+-2 Supersonic Static Pressure	Method	Constant
`-1 Constant	Value	0.0 Pa
+-3 Total Temperature	Method	Constant
`-1 Constant	Value	${Inlet_temp}
+-4 Turbulence Intensity	Method	Constant
`-1 Constant	Value	0.01
`-5 Turbulent Viscosity Ratio	Method	Constant
`-1 Constant	Value	10.0
+-5 **R37.Outlet**	Index	68
	Interfaces	
	Part Surfaces	[R37.Outlet]
	Type	Pressure Outlet
	Allow Per-Surface Values	false
	Topology	SURFACE
	Tags	[]
+-1 Physics Conditions		
+-1 Backflow Specification	Direction	Extrapolated
	Pressure	Environmental
	Scalars	Specified
+-2 Pressure Outlet Option	Option	None

`-3 Turbulence Specification	Method	Intensity + Viscosity Ratio
`-2 Physics Values		
+-1 Pressure	Method	Constant
`-1 Constant	Value	126680.0 Pa
+-2 Static Temperature	Method	Constant
`-1 Constant	Value	300.0 K
+-3 Turbulence Intensity	Method	Constant
`-1 Constant	Value	0.01
`-4 Turbulent Viscosity Ratio	Method	Constant
`-1 Constant	Value	10.0
+-6 **R37.Per1**	Index	67
	Interfaces	Interface 1
	Part Surfaces	[R37.Per1]
	Type	Wall
	Allow Per-Surface Values	false
	Topology	SURFACE
	Tags	[]
+-1 Physics Conditions		
+-1 Reference Frame Specification	Option	Lab Frame
+-2 Shear Stress Specification	Method	No-Slip
+-3 Tangential Velocity Specification	Method	Fixed
+-4 Thermal Specification	Condition	Adiabatic
+-5 User Wall Heat Flux Coefficient Specification	Method	None
+-6 Wall Energy Averaging Option	Circumferential Averaging of Energy	false
`-7 Wall Surface Specification	Method	Smooth
`-2 Physics Values		
`-1 Blended Wall Function	E	9.0
	Kappa	0.42
+-7 **R37.Per1 [Interface 1]**	Index	75
	Interfaces	
	Part Surfaces	[]
	Type	Internal Interface Boundary
	Allow Per-Contact Values	false
	Topology	SURFACE
	Parent Interface	Interface 1
	Tags	[]
+-8 **R37.Per2**	Index	66
	Interfaces	Interface 1
	Part Surfaces	[R37.Per2]
	Type	Wall
	Allow Per-Surface Values	false
	Topology	SURFACE
	Tags	[]
+-1 Physics Conditions		
+-1 Reference Frame Specification	Option	Lab Frame
+-2 Shear Stress Specification	Method	No-Slip
+-3 Tangential Velocity Specification	Method	Fixed
+-4 Thermal Specification	Condition	Adiabatic
+-5 User Wall Heat Flux Coefficient Specification	Method	None
+-6 Wall Energy Averaging Option	Circumferential Averaging of Energy	false
`-7 Wall Surface Specification	Method	Smooth
`-2 Physics Values		
`-1 Blended Wall Function	E	9.0
	Kappa	0.42
+-9 **R37.Per2 [Interface 1]**	Index	74
	Interfaces	
	Part Surfaces	[]
	Type	Internal Interface Boundary
	Allow Per-Contact Values	false
	Topology	SURFACE
	Parent Interface	Interface 1
	Tags	[]
`-10 **R37.Shroud**	Index	69
	Interfaces	
	Part Surfaces	[R37.Shroud]
	Type	Wall
	Allow Per-Surface Values	false
	Topology	SURFACE
	Tags	[]
+-1 Physics Conditions		
+-1 Reference Frame Specification	Option	Local Reference Frame
+-2 Shear Stress Specification	Method	No-Slip

+-3 Tangential Velocity Specification	Method	Fixed
+-4 Thermal Specification	Condition	Adiabatic
+-5 User Wall Heat Flux Coefficient Specification	Method	None
+-6 Wall Energy Averaging Option	Circumferential Averaging of Energy	false
`-7 Wall Surface Specification	Method	Smooth
`-2 Physics Values		
+-1 Blended Wall Function	E	9.0
	Kappa	0.42
`-2 Boundary Reference Frame Specification	Reference Frame	Lab Reference Frame
+-2 Physics Conditions		
+-1 Energy Source Option	Energy Source Option	None
+-2 Initial Condition Option	Option	Use Continuum Values
+-3 Mass Source Option	Mass Source Option	false
+-4 Momentum Source Option	Momentum Source Option	None
+-5 Motion Specification Option	Option	Motion Specification
`-6 Turbulence Source Option	Turbulence Source Option	None
`-3 Physics Values		
`-1 Motion Specification	Motion	Stationary
	Reference Frame	Rotating
+-4 Representations		
+-1 **Latest Surface/Volume**	Representation	Volume Mesh
	Tags	[]
+-2 **Geometry**	Tags	[]
+-1 **Rotor Mesh copy.Remesh**	Tags	[]
`-2 **Latest Surface**	Tags	[]
`-3 **Volume Mesh**	Cells	1534517
	Interior Faces	8289147
	Vertices	6263553
	Tags	[]
+-1 Finite Volume Regions		
`-1 R37_SI	Cells	1534517
	Interior Faces	8289147
	Vertices	6263553
	Edges	0
`-1 Finite Volume Boundaries		
+-1 R37.Blade_Extrados	Faces	19869
+-2 R37.Blade_Intrados	Faces	19826
+-3 R37.Hub	Faces	6690
+-4 R37.Inlet	Faces	4067
+-5 R37.Outlet	Faces	2864
+-6 R37.Per1	Faces	0
+-7 R37.Per1 [Interface 1]	Faces	97320
+-8 R37.Per2	Faces	0
+-9 R37.Per2 [Interface 1]	Faces	97320
`-10 R37.Shroud	Faces	11997
`-2 Cell Sets		
+-5 Contacts		
+-6 Parts		
+-1 **Extrados**	Metadata	{}
	Index	5
	Color	java.awt.Color[r=112,g=128,b=144]
	Is Shell	false
	Region	[]
	Contacts	[]
	Descriptions	[Root]
	Face Count	6966
	Tags	[]
+-1 Surfaces		
`-1 **Blade_Extrados**	Index	29
	Metadata	{}
	Boundary	[]
	Color	java.awt.Color[r=112,g=128,b=144]
	Tags	[]
`-2 Curves		
+-1 **Default**	Index	11
	Tags	[]
+-2 **Leading_edge**	Index	13
	Tags	[]
`-3 **Trailing_edge**	Index	12
	Tags	[]
+-2 **Intrados**	Metadata	{}
	Index	6
	Color	java.awt.Color[r=112,g=128,b=144]
	Is Shell	false
	Region	[]
	Contacts	[]
	Descriptions	[Root]
	Face Count	9648
	Tags	[]
+-1 Surfaces		
`-1 **Blade_Intrados**	Index	30

	Metadata	{}
	Boundary	[]
	Color	java.awt.Color[r=112,g=128,b=144]
	Tags	[]
`-2 Curves		
+-1 **Default**	Index	16
	Tags	[]
+-2 **Leading_edge**	Index	15
	Tags	[]
`-3 **Trailing_edge**	Index	14
	Tags	[]
`-3 **R37**	Metadata	{}
	Index	4
	Color	java.awt.Color[r=112,g=128,b=144]
	Is Shell	false
	Region	[R37_SI]
	Contacts	[]
	Descriptions	[Root, Rotor Mesh copy.Remesh]
	Face Count	29504
	Tags	[]
+-1 Surfaces		
+-1 **Blade_Extrados**	Index	28
	Metadata	{}
	Boundary	[R37_SI: R37.Blade_Extrados]
	Color	java.awt.Color[r=135,g=206,b=250]
	Tags	[]
+-2 **Blade_Intrados**	Index	27
	Metadata	{}
	Boundary	[R37_SI: R37.Blade_Intrados]
	Color	java.awt.Color[r=135,g=206,b=250]
	Tags	[]
+-3 **Hub**	Index	25
	Metadata	{}
	Boundary	[R37_SI: R37.Hub]
	Color	java.awt.Color[r=135,g=206,b=250]
	Tags	[]
+-4 **Inlet**	Index	24
	Metadata	{}
	Boundary	[R37_SI: R37.Inlet]
	Color	java.awt.Color[r=135,g=206,b=250]
	Tags	[]
+-5 **Outlet**	Index	22
	Metadata	{}
	Boundary	[R37_SI: R37.Outlet]
	Color	java.awt.Color[r=135,g=206,b=250]
	Tags	[]
+-6 **Per1**	Index	21
	Metadata	{}
	Boundary	[R37_SI: R37.Per1]
	Color	java.awt.Color[r=135,g=206,b=250]
	Tags	[]
+-7 **Per2**	Index	20
	Metadata	{}
	Boundary	[R37_SI: R37.Per2]
	Color	java.awt.Color[r=135,g=206,b=250]
	Tags	[]
`-8 **Shroud**	Index	23
	Metadata	{}
	Boundary	[R37_SI: R37.Shroud]
	Color	java.awt.Color[r=135,g=206,b=250]
	Tags	[]
`-2 Curves		
+-1 **Default**	Index	4
	Tags	[]
+-2 **Leading_edge**	Index	10
	Tags	[]
+-3 **Per1_Hub**	Index	7
	Tags	[]
+-4 **Per1_Shroud**	Index	8
	Tags	[]
+-5 **Per2_Hub**	Index	5
	Tags	[]
+-6 **Per2_Shroud**	Index	6
	Tags	[]
`-7 **Trailing_edge**	Index	9
	Tags	[]
+-7 3D-CAD Models		
`-1 **3D-CAD Model 1**	Distinguish Bodies Color Palette	High Contrast Color Palette
	Part Update Method	UPDATE_GEOMETRY
	Tags	[]
+-1 Body Groups		
+-1 **Blade**	Name	Blade
	Color	java.awt.Color[r=128,g=128,b=128]
	Opacity	1.0
	Display Resolution	VERY_COARSE
	Tags	[]
`-2 **R37**	Name	R37
	Color	java.awt.Color[r=128,g=128,b=128]
	Opacity	1.0
	Display Resolution	VERY_COARSE
	Tags	[]
+-2 Features		

+-1 **XY**	Error Message	
	Origin	[0.0, 0.0, 0.0] m
	X-Axis	[1.0, 0.0, 0.0]
	Y-Axis	[0.0, 1.0, 0.0]
	Tags	[]
+-2 **YZ**	Error Message	
	Origin	[0.0, 0.0, 0.0] m
	X-Axis	[0.0, 1.0, 0.0]
	Y-Axis	[0.0, 0.0, 1.0]
	Tags	[]
+-3 **ZX**	Error Message	
	Origin	[0.0, 0.0, 0.0] m
	X-Axis	[0.0, 0.0, 1.0]
	Y-Axis	[1.0, 0.0, 0.0]
	Tags	[]
+-4 **Global Origin**	Error Message	
	Position	[0.0, 0.0, 0.0]
	Tags	[]
+-5 **Lab Coordinate System**	Error Message	
	Origin	[0.0, 0.0, 0.0]
	X-axis Direction	[1.0, 0.0, 0.0]
	Y-axis Direction	[0.0, 1.0, 0.0]
	Tags	[]
+-6 **Importa alabe**	Tags	[]
+-1 **Sketch3D 1**	Error Message	
	Coordinate System	Laboratory
	Tags	[]
+-2 **Sketch3D 2**	Error Message	
	Coordinate System	Laboratory
	Tags	[]
+-3 **Sketch3D 3**	Error Message	
	Coordinate System	Laboratory
	Tags	[]
+-4 **Sketch3D 4**	Error Message	
	Coordinate System	Laboratory
	Tags	[]
+-5 **Sketch3D 5**	Error Message	
	Coordinate System	Laboratory
	Tags	[]
+-6 **Sketch3D 6**	Error Message	
	Coordinate System	Laboratory
	Tags	[]
+-7 **Sketch3D 7**	Error Message	
	Coordinate System	Laboratory
	Tags	[]
+-8 **Sketch3D 8**	Error Message	
	Coordinate System	Laboratory
	Tags	[]
+-9 **Sketch3D 9**	Error Message	
	Coordinate System	Laboratory
	Tags	[]
+-10 **Sketch3D 10**	Error Message	
	Coordinate System	Laboratory
	Tags	[]
+-11 **Sketch3D 11**	Error Message	
	Coordinate System	Laboratory
	Tags	[]
+-12 **Sketch3D 12**	Error Message	
	Coordinate System	Laboratory
	Tags	[]
+-13 **Sketch3D 13**	Error Message	
	Coordinate System	Laboratory
	Tags	[]
+-14 **Sketch3D 14**	Error Message	
	Coordinate System	Laboratory
	Tags	[]
+-15 **Sketch3D 15**	Error Message	
	Coordinate System	Laboratory
	Tags	[]
+-16 **Sketch3D 16**	Error Message	
	Coordinate System	Laboratory
	Tags	[]
+-17 **Sketch3D 17**	Error Message	
	Coordinate System	Laboratory
	Tags	[]
+-18 **Sketch3D 18**	Error Message	
	Coordinate System	Laboratory
	Tags	[]
+-19 **Sketch3D 19**	Error Message	

	Coordinate System	Laboratory
	Tags	[]
+-20 **Sketch3D 20**	Error Message	
	Coordinate System	Laboratory
	Tags	[]
+-21 **Sketch3D 21**	Error Message	
	Coordinate System	Laboratory
	Tags	[]
+-22 **Sketch3D 22**	Error Message	
	Coordinate System	Laboratory
	Tags	[]
+-23 **Sketch3D 23**	Error Message	
	Coordinate System	Laboratory
	Tags	[]
+-24 **Sketch3D 24**	Error Message	
	Coordinate System	Laboratory
	Tags	[]
+-25 **Sketch3D 25**	Error Message	
	Coordinate System	Laboratory
	Tags	[]
+-26 **Sketch3D 26**	Error Message	
	Coordinate System	Laboratory
	Tags	[]
+-27 **Sketch3D 27**	Error Message	
	Coordinate System	Laboratory
	Tags	[]
+-28 **Sketch3D 28**	Error Message	
	Coordinate System	Laboratory
	Tags	[]
+-29 **Sketch3D 29**	Error Message	
	Coordinate System	Laboratory
	Tags	[]
+-30 **Sketch3D 30**	Error Message	
	Coordinate System	Laboratory
	Tags	[]
+-31 **Sketch3D 31**	Error Message	
	Coordinate System	Laboratory
	Tags	[]
+-32 **Sketch3D 32**	Error Message	
	Coordinate System	Laboratory
	Tags	[]
+-33 **Sketch3D 33**	Error Message	
	Coordinate System	Laboratory
	Tags	[]
+-34 **Sketch3D 34**	Error Message	
	Coordinate System	Laboratory
	Tags	[]
+-35 **Sketch3D 35**	Error Message	
	Coordinate System	Laboratory
	Tags	[]
+-36 **Sketch3D 36**	Error Message	
	Coordinate System	Laboratory
	Tags	[]
+-37 **Sketch3D 37**	Error Message	
	Coordinate System	Laboratory
	Tags	[]
+-38 **Sketch3D 38**	Error Message	
	Coordinate System	Laboratory
	Tags	[]
+-39 **Sketch3D 39**	Error Message	
	Coordinate System	Laboratory
	Tags	[]
+-40 **Sketch3D 40**	Error Message	
	Coordinate System	Laboratory
	Tags	[]
+-41 **Sketch3D 41**	Error Message	
	Coordinate System	Laboratory
	Tags	[]
+-42 **Sketch3D 42**	Error Message	
	Coordinate System	Laboratory
	Tags	[]
+-43 **Sketch3D 43**	Error Message	
	Coordinate System	Laboratory
	Tags	[]

+-44 **Sketch3D 44**	Error Message	
	Coordinate System	Laboratory
	Tags	[]
+-45 **Sketch3D 45**	Error Message	
	Coordinate System	Laboratory
	Tags	[]
+-46 **Sketch3D 46**	Error Message	
	Coordinate System	Laboratory
	Tags	[]
+-47 **Sketch3D 47**	Error Message	
	Coordinate System	Laboratory
	Tags	[]
+-48 **Sketch3D 48**	Error Message	
	Coordinate System	Laboratory
	Tags	[]
+-49 **Sketch3D 49**	Error Message	
	Coordinate System	Laboratory
	Tags	[]
+-50 **Sketch3D 50**	Error Message	
	Coordinate System	Laboratory
	Tags	[]
+-51 **Sketch3D 51**	Error Message	
	Coordinate System	Laboratory
	Tags	[]
+-52 **Sketch3D 52**	Error Message	
	Coordinate System	Laboratory
	Tags	[]
+-53 **Sketch3D 53**	Error Message	
	Coordinate System	Laboratory
	Tags	[]
+-54 **Sketch3D 54**	Error Message	
	Coordinate System	Laboratory
	Tags	[]
+-55 **Loft 1**	Error Message	
	Trim Guide Curves	true
	Closed	false
	Alignment Type	KeepParameterization
	Start Contact Type	None
	End Contact Type	None
	Remove Redundancies	DeleteEdges
	Body Type	Sheet
	Body Interaction	Merge
	Interacting Bodies	All
	Tags	[]
+-56 **Loft 2**	Error Message	
	Trim Guide Curves	true
	Closed	false
	Alignment Type	KeepParameterization
	Start Contact Type	None
	End Contact Type	None
	Remove Redundancies	DeleteEdges
	Body Type	Sheet
	Body Interaction	Merge
	Interacting Bodies	All
	Tags	[]
+-57 **Fill Surface 1**	Error Message	
	Set Tangency at all Edges	false
	Tolerance	1.0E-6 m
	Tags	[]
+-58 **Fill Surface 2**	Error Message	
	Set Tangency at all Edges	false
	Tolerance	1.0E-6 m
	Tags	[]
`-59 **SewSheetBodies 1**	Error Message	
	Sewing Tolerance	1.0E-6 m
	Attempt to Form Solid	true
	Sew Bodies Independently	false
	Tags	[]
+-7 **Sketch 1**	Error Message	
	Tags	[]
+-8 **Revolve 1**	Error Message	
	Input Type	Sketch
	Sketch	Sketch 1

	DirectionAxis	[0.0, 0.0, 1.0] m,m,m
	DirectionAxis	[0.0, 0.0, 0.0] m,m,m
	Direction	Normal
	Revolve Options	TwoWaySymmetric
	Angle	50.0 deg
	Asymmetric Angle	90.0 deg
	Axis Type	Specified
	Body Type	Sheet
	Body Interaction	Merge
	Bodies to Interact	All
	Tags	[]
+-9 **Sketch3D 55**	Error Message	
	Coordinate System	Laboratory
	Tags	[]
+-10 **Sketch3D 56**	Error Message	
	Coordinate System	Laboratory
	Tags	[]
+-11 **DeleteBody 1**	Error Message	
	Delete Mode	Manual
	Solids	None
	Minimum Volume	0.001 m^3
	Maximum Volume	0.002 m^3
	Sheets	None
	Minimum Area	0.001 m^2
	Maximum Area	0.002 m^2
	Tags	[]
+-12 **Loft 3**	Error Message	
	Trim Guide Curves	true
	Closed	false
	Alignment Type	KeepParameterization
	Start Contact Type	None
	End Contact Type	None
	Remove Redundancies	DeleteEdges
	Body Type	Sheet
	Body Interaction	Merge
	Interacting Bodies	All
	Tags	[]
+-13 **RotateBody 1**	Error Message	
	Axis Type	Specified
	Axis Direction	[0.0, 0.0, 1.0] m,m,m
	Axis Position	[0.0, 0.0, 0.0] m,m,m
	Angle	5.0 deg
	Action	Copy
	Body Group	false
	Tags	[]
+-14 **RotateBody 2**	Error Message	
	Axis Type	Specified
	Axis Direction	[0.0, 0.0, 1.0] m,m,m
	Axis Position	[0.0, 0.0, 0.0] m,m,m
	Angle	-5.0 deg
	Action	Rotate
	Body Group	false
	Tags	[]
+-15 **Revolve 2**	Error Message	
	Input Type	Edges
	Sketch	
	DirectionAxis	[0.0, 0.0, 1.0] m,m,m
	DirectionAxis	[0.0, 0.0, 0.0] m,m,m
	Direction	Normal
	Revolve Options	OneWay
	Angle	-10.0 deg
	Asymmetric Angle	90.0 deg
	Axis Type	Specified
	Body Type	Sheet
	Body Interaction	Merge
	Bodies to Interact	All
	Tags	[]
+-16 **SewSheetBodies 2**	Error Message	
	Sewing Tolerance	1.0E-6 m
	Attempt to Form Solid	true
	Sew Bodies Independently	false
	Tags	[]
+-17 **ScaleBody 1**	Error Message	
	Scale all Dimensions Uniformly	true
	X	0.001
	Y	0.001
	Z	0.001
	Action	Scale
	Body Group	false
	Tags	[]

| | +-18 **SubtractBodies 1**	Error Message	
| | |	Keep Tool Bodies	true
| | |	Imprint	false
| | |	Precision Type	Precise
| | |	Tolerance	1.0E-5 m
| | |	Use Auto-Matching	true
| | |	Transfer Face Names	true
| | |	Transfer Body Names	false
| | |	Body Group	false
| | |	Tags	[]
| | +-19 **ThickenBodies 1**	Error Message	
| | |	Direction	FrontSide
| | |	Thickness	0.035 m
| | |	Tolerance	1.0E-7 m
| | |	Tags	[]
| | +-20 **ThickenBodies 2**	Error Message	
| | |	Direction	FrontSide
| | |	Thickness	0.03 m
| | |	Tolerance	1.0E-7 m
| | |	Tags	[]
| | `-21 **ScaleBody 2**	Error Message	
| |	Scale all Dimensions Uniformly	true
| |	X	10.0
| |	Y	10.0
| |	Z	10.0
| |	Action	Scale
| |	Body Group	false
| |	Tags	[]
| +-3 Design Filters		
| `-4 Design Parameters		
+-8 Operations		
| `-1 **Rotor Mesh copy**	Per-Part Meshing	false
| |	Mesher Execution Mode	Parallel
| |	Input Parts	[R37]
| |	Perform Local Meshing	false
| |	Preserve Surface Perimeters	None
| |	Verbose Output	false
| |	Tags	[]
| +-1 Meshers		
| | +-1 Surface Remesher	Meshing Method	Triangle
| | |	Perform Curvature Refinement	true
| | |	Perform Proximity Refinement	true
| | |	Perform Compatibility Refinement	false
| | |	Create Aligned Meshes	true
| | |	Minimum Face Quality	0.05
| | |	Field Function based Refinement	[]
| | +-2 Automatic Surface Repair	Connected Surface Count Limit	None
| | |	Connected Surface Size Limit(s)	None
| | |	Minimum Face Quality	0.05
| | +-3 Polyhedral Mesher	Field Function based Refinement	[Field Function Mesh Refinement]
| | |	Run Post Mesh Optimizer	true
| | `-4 Prism Layer Mesher	Stretching Function	Geometric Progression
| |	Distribution Mode	Stretch Factor
| +-2 Default Controls		
| | +-1 Base Size	Base Size	${Mesh_basesize}
| | |	Base Size	${Mesh_basesize}
| | +-2 CAD Projection	Project to CAD	true
| | +-3 Target Surface Size	Size Type	Absolute
| | |	Percentage of Base	66.66666666666667
| | |	Absolute Size	${Mesh_targetsurface}
| | +-4 Minimum Surface Size	Size Type	Relative to base
| | |	Percentage of Base	10.0
| | |	Absolute Size	1.7999999999999998E-4 m
| | +-5 Surface Curvature	Enable Curvature	true

	Deviation Distance	
| | |	# Pts/circle	10.0
| | |	Max # Pts/circle	35.0
| | |	Curvature Deviation Distance	${Mesh_basesize}
| | +-6 Surface Proximity	Search Floor	0.0 m
| | |	# Points in gap	2.0
| | |	Enable Search Ceiling	false
| | |	Search Ceiling	1.0E10 m
| | |	Search Direction	INSIDE
| | +-7 Surface Growth Rate	Surface Growth Rate	DEFAULT
| | |	User Specified Value	1.3
| | +-8 Auto-Repair Minimum Proximity	Minimum Proximity	0.01
| | +-9 Volume Growth Rate	Volume Growth Rate	1.15
| | +-10 Maximum Tet Size	Size Type	Relative to base
| | |	Percentage of Base	10000.0
| | |	Absolute Size	0.18 m
| | +-11 Core Mesh Optimization	Optimization Cycles	1
| | |	Quality Threshold	0.4
| | `-12 Post Mesh Optimization	Optimize Boundary Vertices	false
| |	Optimize Cell Topology	false
| `-3 Custom Controls		
| +-1 **Blade Surface Control**	Enable Control	true
| | |	Controls Display Mode	All
| | |	Part Surfaces	[R37.Blade_Extrados, R37.Blade_Intrados]
| | |	Apply Only to Contacting Area	false
| | |	Tags	[]
| | +-1 Controls		
| | | +-1 Target Surface Size	Target Surface Size	Custom
| | | +-2 Minimum Surface Size	Minimum Surface Size	Parent
| | | +-3 Surface Curvature	Curvature	Custom
| | | +-4 Surface Proximity	Proximity	Parent
| | | +-5 Edge Proximity	Proximity	Parent
| | | +-6 Surface Growth Rate	Surface Growth Rate	Parent
| | | +-7 Surface Remeshing	Surface Remeshing	Parent
| | | +-8 Meshing Method	Meshing Method	Parent
| | | +-9 Prism Layers	Prism Layers	Custom
| | | | `-1 Customize	Customize Number of Layers	true
| | | |	Customize Total Thickness	true
| | | |	Customize Distribution	true
| | | |	Override Boundary Defaults	false
| | | |	Customize Minimum Thickness Percentage	false
| | | |	Customize Boundary March Angle	false
| | | |	Customize Concave Angle Limit	false
| | | |	Customize Convex Angle Limit	false
| | | `-10 Wake Refinement	Specify wake refinement options	false
| | `-2 Values		
| | +-1 Target Surface Size	Size Type	Relative to base
| | |	Percentage of Base	50.0
| | |	Absolute Size	9.0E-4 m
| | +-2 Custom Prism Values		
| | | +-1 Number of Prism Layers	Number of Prism Layers	${Mesh_numprismlayer}
| | | +-2 Prism Layer Stretching	Prism Layer Stretching	1.25
| | | `-3 Prism Layer Total Thickness	Size Type	Relative to base
| | |	Percentage of Base	20.0
| | |	Absolute Size	3.5999999999999997E-4 m
| | `-3 Surface Curvature	Enable Curvature	true

	Deviation Distance	
	# Pts/circle	20.0
	Max # Pts/circle	30.0
	Curvature Deviation Distance	${Mesh_basesize}/10000
+-2 **Blade tip**	Enable Control	true
	Controls Display Mode	All
	Part Surfaces	[]
	Apply Only to Contacting Area	false
	Tags	[]
+-1 Controls		
+-1 Target Surface Size	Target Surface Size	Custom
+-2 Minimum Surface Size	Minimum Surface Size	Parent
+-3 Surface Curvature	Curvature	Parent
+-4 Surface Proximity	Proximity	Parent
+-5 Edge Proximity	Proximity	Parent
+-6 Surface Growth Rate	Surface Growth Rate	Parent
+-7 Surface Remeshing	Surface Remeshing	Parent
+-8 Meshing Method	Meshing Method	Parent
+-9 Prism Layers	Prism Layers	Parent
`-10 Wake Refinement	Specify wake refinement options	false
`-2 Values		
`-1 Target Surface Size	Size Type	Relative to base
	Percentage of Base	25.0
	Absolute Size	4.5E-4 m
+-3 **Carcasa-Hub**	Enable Control	true
	Controls Display Mode	All
	Part Surfaces	[R37.Hub]
	Apply Only to Contacting Area	false
	Tags	[]
+-1 Controls		
+-1 Target Surface Size	Target Surface Size	Custom
+-2 Minimum Surface Size	Minimum Surface Size	Parent
+-3 Surface Curvature	Curvature	Parent
+-4 Surface Proximity	Proximity	Parent
+-5 Edge Proximity	Proximity	Parent
+-6 Surface Growth Rate	Surface Growth Rate	Parent
+-7 Surface Remeshing	Surface Remeshing	Parent
+-8 Meshing Method	Meshing Method	Parent
+-9 Prism Layers	Prism Layers	Parent
`-10 Wake Refinement	Specify wake refinement options	false
`-2 Values		
`-1 Target Surface Size	Size Type	Relative to base
	Percentage of Base	200.0
	Absolute Size	0.0036 m
+-4 **Carcasa-Shroud**	Enable Control	true
	Controls Display Mode	All
	Part Surfaces	[R37.Shroud]
	Apply Only to Contacting Area	false
	Tags	[]
+-1 Controls		
+-1 Target Surface Size	Target Surface Size	Custom
+-2 Minimum Surface Size	Minimum Surface Size	Parent
+-3 Surface Curvature	Curvature	Parent
+-4 Surface Proximity	Proximity	Parent
+-5 Edge Proximity	Proximity	Parent
+-6 Surface Growth Rate	Surface Growth Rate	Parent
+-7 Surface Remeshing	Surface Remeshing	Parent
+-8 Meshing Method	Meshing Method	Parent
+-9 Prism Layers	Prism Layers	Parent
`-10 Wake Refinement	Specify wake refinement options	false
`-2 Values		
`-1 Target Surface Size	Size Type	Relative to base
	Percentage of Base	75.0
	Absolute Size	0.00135 m
+-5 **Curve Leading Edge**	Enable Control	true
	Controls Display Mode	All
	Part Curves	[R37.Leading_edge]
	Tags	[]

+-1 Controls		
+-1 Target Surface Size	Target Surface Size	Custom
+-2 Minimum Surface Size	Minimum Surface Size	Parent
+-3 Anisotropic Surface Size	Specify anisotropic surface size settings	false
	Specify anisotropic mesh distribution between close Part Curves	false
`-4 Wake Refinement	Specify wake refinement options	false
`-2 Values		
`-1 Target Surface Size	Size Type	Relative to base
	Percentage of Base	3.0
	Absolute Size	5.4000000000000005E-5 m
+-6 **Curve Trailing Edge**	Enable Control	true
	Controls Display Mode	All
	Part Curves	[R37.Trailing_edge]
	Tags	[]
+-1 Controls		
+-1 Target Surface Size	Target Surface Size	Custom
+-2 Minimum Surface Size	Minimum Surface Size	Parent
+-3 Anisotropic Surface Size	Specify anisotropic surface size settings	false
	Specify anisotropic mesh distribution between close Part Curves	false
`-4 Wake Refinement	Specify wake refinement options	false
`-2 Values		
`-1 Target Surface Size	Size Type	Relative to base
	Percentage of Base	3.0
	Absolute Size	5.4000000000000005E-5 m
`-7 **Periodic Control**	Enable Control	true
	Controls Display Mode	All
	Part Surfaces	[R37.Per1, R37.Per2]
	Apply Only to Contacting Area	false
	Tags	[]
+-1 Controls		
+-1 Target Surface Size	Target Surface Size	Custom
+-2 Minimum Surface Size	Minimum Surface Size	Parent
+-3 Surface Curvature	Curvature	Parent
+-4 Surface Proximity	Proximity	Parent
+-5 Edge Proximity	Proximity	Parent
+-6 Surface Growth Rate	Surface Growth Rate	Parent
+-7 Surface Remeshing	Surface Remeshing	Parent
+-8 Meshing Method	Meshing Method	Parent
+-9 Prism Layers	Prism Layers	Disable
`-10 Wake Refinement	Specify wake refinement options	false
`-2 Values		
`-1 Target Surface Size	Size Type	Relative to base
	Percentage of Base	35.0
	Absolute Size	6.3E-4 m
+-9 Descriptions	Number of Children	4
+-1 Root	Described Parts	[R37, Extrados, Intrados]
+-2 Rotor Mesh copy.Remesh	Described Parts	[R37]
	Faces	354952
	Vertices	177476
+-3 Latest Surface	Described Parts	[R37, Extrados, Intrados]
	Faces	371566
	Vertices	186521
	Preview Mesh Operation Parts	false
`-4 Latest Surface/Volume	Described Parts	[R37, Extrados, Intrados]
+-10 Coordinate Systems		
`-1 **Laboratory**	Tags	[]
`-1 Local Coordinate Systems		
+-1 **Cylindrical-Parametrization**	Radial Axis Input	[1.0, 0.0, 0.0]
	Vector on R-Theta Plane Input	[0.0, 1.0, 0.0]
	Radial Axis Direction	[1.0, 0.0, 0.0]

| | |	Tangential Axis Direction	[0.0, 1.0, 0.0]
| | |	Axial Axis Direction	[0.0, 0.0, 1.0]
| | |	Origin	[0.0, 0.0, 0.0] m,m,m
| | |	Reference System	Laboratory
| | |	Tags	[]
| | `-1 Local Coordinate Systems		
| +-2 **Isospan 10%**	X Axis Input	[1.0, 0.0, 0.0]
| | |	Vector on X-Y Plane Input	[0.0, 0.0132, 0.010971]
| | |	X Axis Direction	[1.0, 0.0, 0.0]
| | |	Y Axis Direction	[0.0, 0.7690515749340064, 0.6391867294394685]
| | |	Z Axis Direction	[0.0, -0.6391867294394685, 0.7690515749340064]
| | |	Origin	[0.18429, -0.021395, 4.6703E-4] m,m,m
| | |	Reference System	Laboratory
| | |	Tags	[]
| | `-1 Local Coordinate Systems		
| +-3 **Isospan 50%**	X Axis Input	[1.0, 0.0, 0.0]
| | |	Vector on X-Y Plane Input	[0.0, 0.019162, 0.013261]
| | |	X Axis Direction	[1.0, 0.0, 0.0]
| | |	Y Axis Direction	[0.0, 0.8222925944991922, 0.5690649251463202]
| | |	Z Axis Direction	[0.0, -0.5690649251463202, 0.8222925944991922]
| | |	Origin	[0.21459, -0.023181, 0.0028962] m,m,m
| | |	Reference System	Laboratory
| | |	Tags	[]
| | `-1 Local Coordinate Systems		
| `-4 **Isospan 90%**	X Axis Input	[1.0, 0.0, 0.0]
| |	Vector on X-Y Plane Input	[0.0, 0.017118, 0.0097611]
| |	X Axis Direction	[1.0, 0.0, 0.0]
| |	Y Axis Direction	[0.0, 0.8686934205953355, 0.49535011962689146]
| |	Z Axis Direction	[0.0, -0.49535011962689146, 0.8686934205953355]
| |	Origin	[0.24402, -0.024331, 0.0054204] m,m,m
| |	Reference System	Laboratory
| |	Tags	[]
| `-1 Local Coordinate Systems		
+-11 Parameterizations		
| +-1 **Axisymmetric Complete Domain**	Cylindrical coordinate system	[Laboratory->Cylindrical-Parametrization]
| | |	Geometry	[R37]
| | |	Computation mesh resolution	[512, 512]
| | |	Tags	[]
| | +-1 Meridional	Min	[R37.Inlet]
| | | |	Max	[R37.Outlet]
| | | |	Interfaces	[]
| | | +-1 Parts		
| | | +-2 Parts		
| | | `-3 Parts		
| | +-2 Spanwise	Min	[R37.Hub]
| | | |	Max	[R37.Shroud]
| | | +-1 Parts		
| | | `-2 Parts		
| | `-3 Circumferential	Min	[R37.Per1]
| | |	Max	[R37.Per2]
| | +-1 Parts		
| | `-2 Parts		
| `-2 **Blade 1**	Pressure-side Blade Surfaces	[R37.Blade_Extrados]
|	Suction-side Blade Surfaces	[R37.Blade_Intrados]
|	Axisymmetric Parameterization	[Axisymmetric Complete Domain]
|	Leading Edge	[R37.Leading_edge]
|	Trailing Edge	[R37.Trailing_edge]
|	Tags	[]
+-12 Tables	Tables	5
| +-1 Relative Mach Import		
| | +-1 **Relative_Mach_4**	Extracted	[Relative Mach Number, X, Y, Z]
| | |	Path	C:\Users\inigo\OneDrive\Escritorio\TFG\CFD Cases\Case 1\Relative Mach Tables\Relative_Mach_4.csv
| | |	Keep Internal Units on Reload	false
| | |	Tags	[]
| | +-2 **Relative_Mach_10**	Extracted	[Relative Mach Number, X, Y, Z]
| | |	Path	C:\Users\inigo\OneDrive\Escritorio\TFG\CFD Cases\Case 1\Relative Mach Tables\Relative_Mach_10.csv
| | |	Keep Internal Units on Reload	false
| | |	Tags	[]
| | `-3 **Relative_Mach_40**	Extracted	[Relative Mach Number, X, Y, Z]
| |	Path	C:\Users\inigo\OneDrive\Escritorio\TFG\CFD Cases\Case 1\Relative Mach Tables\Relative_Mach_40.csv
| |	Keep Internal Units on Reload	false
| |	Tags	[]
| +-2 **Pressure**	Extracted	[Pressure, X, Y, Z]
| | |	Scalars	[Pressure]
| | |	Parts	[R37_SI]
| | |	Coordinate System	Laboratory

				Data on Vertices	false
				Representation	Volume Mesh
				Tags	[]
		`-1 Update	Enabled	true
			Auto Extract	false
			Trigger	None
			Save To File	false
			Output Directory	
			Base Filename Append Tag	table
	`-3 **Pressure_10**	Extracted	[Pressure_10, X, Y, Z]
			Scalars	[Pressure_10]
			Parts	[R37_SI]
			Coordinate System	Laboratory
			Data on Vertices	false
			Representation	Volume Mesh
			Tags	[]
	`-1 Update	Enabled	true
		Auto Extract	false
		Trigger	None
		Save To File	false
		Output Directory	
		Base Filename Append Tag	table
+-13 Units	Preferred System	Systeme International
+-14 Custom Trees	Initial Tree View	[]
+-15 Volume Shapes		
+-16 Idealizations	Region selection priority	[Interface 1 Periodic Interface Idealization 1]
			Idealizations	1
	`-1 **Interface 1 Periodic Interface Idealization 1**	Regions	[R37_SI]
		Periodic Interface	[Interface 1]
		Tags	[]
+-17 Color Palettes		
	+-1 **High Contrast Color Palette**	Number of Colors	28
			Swatches	[java.awt.Color[r=255,g=0,b=0], java.awt.Color[r=0,g=255,b=0], java.awt.Color[r=0,g=0,b=255], java.awt.Color[r=255,g=255,b=0], java.awt.Color[r=255,g=128,b=0], java.awt.Color[r=160,g=32,b=240], java.awt.Color[r=255,g=255,b=255], java.awt.Color[r=255,g=192,b=203], java.awt.Color[r=189,g=252,b=201], java.awt.Color[r=175,g=238,b=238], java.awt.Color[r=240,g=230,b=140], java.awt.Color[r=255,g=228,b=181], java.awt.Color[r=221,g=160,b=221], java.awt.Color[r=192,g=192,b=192], java.awt.Color[r=219,g=112,b=147], java.awt.Color[r=0,g=201,b=87], java.awt.Color[r=0,g=255,b=255], java.awt.Color[r=255,g=227,b=3], java.awt.Color[r=255,g=176,b=15], java.awt.Color[r=186,g=85,b=211], java.awt.Color[r=128,g=128,b=105], java.awt.Color[r=176,g=48,b=96], java.awt.Color[r=34,g=139,b=34], java.awt.Color[r=95,g=158,b=160], java.awt.Color[r=255,g=215,b=0], java.awt.Color[r=255,g=97,b=3], java.awt.Color[r=143,g=94,b=153], java.awt.Color[r=115,g=74,b=18]]
			Tags	[]
	+-2 **Legacy Plot Color Palette**	Number of Colors	13
			Swatches	[java.awt.Color[r=255,g=0,b=0], java.awt.Color[r=0,g=255,b=0], java.awt.Color[r=0,g=0,b=255], java.awt.Color[r=255,g=200,b=0], java.awt.Color[r=0,g=255,b=255], java.awt.Color[r=0,g=0,b=0], java.awt.Color[r=178,g=0,b=0], java.awt.Color[r=0,g=178,b=0], java.awt.Color[r=0,g=0,b=178], java.awt.Color[r=8,g=46,b=84], java.awt.Color[r=178,g=140,b=0], java.awt.Color[r=160,g=32,b=240], java.awt.Color[r=92,g=36,b=110]]
			Tags	[]
	`-3 **Siemens Color Palette**	Number of Colors	30
		Swatches	[java.awt.Color[r=15,g=120,b=155], java.awt.Color[r=229,g=192,b=76], java.awt.Color[r=219,g=83,b=90], java.awt.Color[r=96,g=106,b=117], java.awt.Color[r=226,g=137,b=77], java.awt.Color[r=127,g=70,b=100], java.awt.Color[r=104,g=153,b=98], java.awt.Color[r=232,g=170,b=184], java.awt.Color[r=165,g=143,b=111], java.awt.Color[r=127,g=178,b=172], java.awt.Color[r=0,g=85,b=125], java.awt.Color[r=168,g=133,b=45], java.awt.Color[r=153,g=49,b=64], java.awt.Color[r=50,g=57,b=63], java.awt.Color[r=170,g=97,b=48], java.awt.Color[r=81,g=45,b=67], java.awt.Color[r=71,g=102,b=66], java.awt.Color[r=173,g=104,b=127], java.awt.Color[r=112,g=94,b=75], java.awt.Color[r=77,g=124,b=115], java.awt.Color[r=70,g=170,b=193], java.awt.Color[r=234,g=208,b=150], java.awt.Color[r=234,g=172,b=185], java.awt.Color[r=170,g=180,b=188], java.awt.Color[r=239,g=194,b=163], java.awt.Color[r=186,g=131,b=165], java.awt.Color[r=165,g=198,b=158], java.awt.Color[r=239,g=203,b=217], java.awt.Color[r=204,g=188,b=168], java.awt.Color[r=180,g=214,b=208]]
		Tags	[]
+-18 Data Set Functions	Data Directory	function_data
		In-core surface FFTs	false
+-19 User Code		
+-20 Data Focus		
+-21 Layouts		
	`-1 default		
	`-1 Mode 1	Mode Name	Mode 1
			System Mode Name	anonymousMode_1
			Split Constraints	[0.0, 1.0, 0.5, 1.0, 0.0, 0.3357329842931937, 0.0, 0.0, 0.98005698005698, 0.0, 1.0, 0.09057971014492754, 1.0, 0.0, 0.3370418848167539, 1.0, 1.0, 0.7238219895287958, 0.0, 0.0, 0.9172714078374455]
			Bounds	[0.0, 0.0, 0.0, 0.0]
			State	0
	+-1 **Tab 1**	Scene or Plot	Diff 40-10 RM Meridional
			Tags	[]
	+-2 **Tab 2**	Scene or Plot	Diff 40-4 RM Meridional
			Tags	[]
	+-3 **Tab 3**	Scene or Plot	Diff 100-10 RM Meridional
			Tags	[]
	+-4 **Tab 4**	Scene or Plot	Diff 10-4 RM Meridional
			Tags	[]
	+-5 **Tab 5**	Scene or Plot	Diff 100-40 RM Meridional
			Tags	[]
	`-6 **Tab 6**	Scene or Plot	Diff 100-4 RM Meridional
		Tags	[]

+-22 Data Mappers	Use Legacy Volume Mapper	false
| +-1 **Tabular Data Mapper p4**	Mapped Names	{'Surface 1': {'Relative Mach Number': 'MappedVertexRelative Mach Number p4'}, 'Volume 1': {'Relative Mach Number': 'MappedVertexRelative Mach Number p4'}}
| | |	Source Table	Relative_Mach_4
| | |	Source: X-Coordinate	X
| | |	Source: Y-Coordinate	Y
| | |	Source: Z-Coordinate	Z
| | |	Source: Data	[Relative Mach Number]
| | |	Verbosity	true
| | |	Tags	[]
| | +-1 Target Specifications		
| | | +-1 **Surface 1**	Compute Nodal Forces Target	false
| | | | |	HTC Target	false
| | | | |	Representation	Volume Mesh
| | | | |	Target Source Transform	Identity Transform
| | | | |	Interpolation Method	Least Squares
| | | | |	Limiter	STENCIL
| | | | |	Target Entities	[R37_SI: R37.Blade_Extrados, R37_SI: R37.Blade_Intrados, R37_SI: R37.Hub, R37_SI: R37.Inlet, R37_SI: R37.Outlet, R37_SI: R37.Per1, R37_SI: R37.Per1 [Interface 1], R37_SI: R37.Per2, R37_SI: R37.Per2 [Interface 1], R37_SI: R37.Shroud]
| | | | |	Use Original Mesh	false
| | | | |	Target Stencil	VERTEX
| | | | |	Target Grouping Threshold	500000
| | | | |	Tags	[]
| | | | `-1 Proximity Constraint	Enable	false
| | | |	Use Absolute Tolerance	false
| | | |	Relative Proximity Tolerance	1.0
| | | |	Absolute Proximity Tolerance	0.0 m
| | | `-2 **Volume 1**	Representation	Volume Mesh
| | | |	Target Source Transform	Identity Transform
| | | |	Interpolation Method	Least Squares
| | | |	Limiter	STENCIL
| | | |	Target Entities	[R37_SI]
| | | |	Use Original Mesh	false
| | | |	Target Stencil	VERTEX
| | | |	Boundary Map Option	Do Not Map To Boundaries
| | | |	Tags	[]
| | | `-1 Proximity Constraint	Enable	false
| | |	Use Absolute Tolerance	false
| | |	Relative Proximity Tolerance	1.0
| | |	Absolute Proximity Tolerance	0.0 m
| | `-2 Update	Enabled	false
| | |	Trigger	Iteration
| | `-1 Iteration Frequency	Iteration Frequency	1
| |	Start Iteration	0
| |	Enable Stop	false
| |	Stop Iteration	0
| +-2 **Tabular Data Mapper p10**	Mapped Names	{'Surface 1': {'Relative Mach Number': 'MappedVertexRelative Mach Number p10'}, 'Volume 1': {'Relative Mach Number': 'MappedVertexRelative Mach Number p10'}}
| | |	Source Table	Relative_Mach_10
| | |	Source: X-Coordinate	X
| | |	Source: Y-Coordinate	Y
| | |	Source: Z-Coordinate	Z
| | |	Source: Data	[Relative Mach Number]
| | |	Verbosity	true
| | |	Tags	[]
| | +-1 Target Specifications		
| | | +-1 **Surface 1**	Compute Nodal Forces Target	false
| | | | |	HTC Target	false
| | | | |	Representation	Volume Mesh
| | | | |	Target Source Transform	Identity Transform
| | | | |	Interpolation Method	Least Squares
| | | | |	Limiter	STENCIL
| | | | |	Target Entities	[R37_SI: R37.Blade_Extrados, R37_SI: R37.Blade_Intrados, R37_SI: R37.Hub, R37_SI: R37.Inlet, R37_SI: R37.Outlet, R37_SI: R37.Per1, R37_SI: R37.Per1 [Interface 1], R37_SI: R37.Per2, R37_SI: R37.Per2 [Interface 1], R37_SI: R37.Shroud]
| | | | |	Use Original Mesh	false
| | | | |	Target Stencil	VERTEX

	Target Grouping Threshold	500000
	Tags	[]
`-1 Proximity Constraint	Enable	false
	Use Absolute Tolerance	false
	Relative Proximity Tolerance	1.0
	Absolute Proximity Tolerance	0.0 m
`-2 **Volume 1**	Representation	Volume Mesh
	Target Source Transform	Identity Transform
	Interpolation Method	Least Squares
	Limiter	STENCIL
	Target Entities	[R37_SI]
	Use Original Mesh	false
	Target Stencil	VERTEX
	Boundary Map Option	Do Not Map To Boundaries
	Tags	[]
`-1 Proximity Constraint	Enable	false
	Use Absolute Tolerance	false
	Relative Proximity Tolerance	1.0
	Absolute Proximity Tolerance	0.0 m
`-2 Update	Enabled	false
	Trigger	Iteration
`-1 Iteration Frequency	Iteration Frequency	1
	Start Iteration	0
	Enable Stop	false
	Stop Iteration	0
`-3 **Tabular Data Mapper p40**	Mapped Names	{'Surface 1': {'Relative Mach Number': 'MappedVertexRelative Mach Number p40'}, 'Volume 1': {'Relative Mach Number': 'MappedVertexRelative Mach Number p40'}}
	Source Table	Relative_Mach_40
	Source: X-Coordinate	X
	Source: Y-Coordinate	Y
	Source: Z-Coordinate	Z
	Source: Data	[Relative Mach Number]
	Verbosity	true
	Tags	[]
+-1 Target Specifications		
+-1 **Surface 1**	Compute Nodal Forces Target	false
	HTC Target	false
	Representation	Volume Mesh
	Target Source Transform	Identity Transform
	Interpolation Method	Least Squares
	Limiter	STENCIL
	Target Entities	[R37_SI: R37.Blade_Extrados, R37_SI: R37.Blade_Intrados, R37_SI: R37.Hub, R37_SI: R37.Inlet, R37_SI: R37.Outlet, R37_SI: R37.Per1, R37_SI: R37.Per2, R37_SI: R37.Shroud, R37_SI: R37.Per1 [Interface 1], R37_SI: R37.Per2 [Interface 1]]
	Use Original Mesh	false
	Target Stencil	VERTEX
	Target Grouping Threshold	500000
	Tags	[]
`-1 Proximity Constraint	Enable	false
	Use Absolute Tolerance	false
	Relative Proximity Tolerance	1.0
	Absolute Proximity Tolerance	0.0 m
`-2 **Volume 1**	Representation	Volume Mesh
	Target Source Transform	Identity Transform
	Interpolation Method	Least Squares
	Limiter	STENCIL
	Target Entities	[R37_SI]
	Use Original Mesh	false
	Target Stencil	VERTEX
	Boundary Map Option	Do Not Map To Boundaries
	Tags	[]
`-1 Proximity Constraint	Enable	false
	Use Absolute Tolerance	false
	Relative Proximity Tolerance	1.0

	Absolute Proximity Tolerance	0.0 m
`-2 Update	Enabled	false
	Trigger	Iteration
`-1 Iteration Frequency	Iteration Frequency	1
	Start Iteration	0
	Enable Stop	false
	Stop Iteration	0
+-23 Motions	Motion Preview Time	0.0 s
	Visual Motion Transforms	[]
	Motion Preview Parts	[]
`-1 **Stationary**	Tags	[]
+-24 Reference Frames		
+-1 **Lab Reference Frame**	Tags	[]
`-2 **Rotating**	Axis Direction	[0.0, 0.0, 1.0]
	Axis Origin	[0.0, 0.0, 0.0] m
	Rotation Rate	${w (rad/s)}
	Coordinate System	Laboratory
	Tags	[]
`-1 Relative Reference Frames		
+-25 Screenplays		
+-26 Derived Parts	Derived Parts	30
+-1 **10% Span**	Parts	[R37_SI]
	Scalar Field	Axisymmetric Complete Domain S Normalized
	Mode	ISOVALUE_SINGLE
	Tags	[]
`-1 Value	Isovalue	0.1
+-2 **10% Span - extrados**	Parts	[R37_SI: R37.Blade_Extrados]
	Scalar Field	Axisymmetric Complete Domain S Normalized
	Mode	ISOVALUE_SINGLE
	Tags	[]
`-1 Value	Isovalue	0.1
+-3 **10% Span - intrados**	Parts	[R37_SI: R37.Blade_Intrados]
	Scalar Field	Axisymmetric Complete Domain S Normalized
	Mode	ISOVALUE_SINGLE
	Tags	[]
`-1 Value	Isovalue	0.1
+-4 **10% Span projection**	Parts	[10% Span]
	Coordinate System	Laboratory
	Rotation Origin	[0.0, 0.0, 0.0] m,m,m
	Rotation Axis	[1.0, 0.0, 0.0] m,m,m
	Tangential Axis	[0.0, 1.0, 0.0] m,m,m
	Tags	[]
+-5 **50% Span**	Parts	[R37_SI]
	Scalar Field	Axisymmetric Complete Domain S Normalized
	Mode	ISOVALUE_SINGLE
	Tags	[]
`-1 Value	Isovalue	0.5
+-6 **50% Span - extrados**	Parts	[R37_SI: R37.Blade_Extrados]
	Scalar Field	Axisymmetric Complete Domain S Normalized
	Mode	ISOVALUE_SINGLE
	Tags	[]
`-1 Value	Isovalue	0.5
+-7 **50% Span - intrados**	Parts	[R37_SI: R37.Blade_Intrados]
	Scalar Field	Axisymmetric Complete Domain S Normalized
	Mode	ISOVALUE_SINGLE
	Tags	[]
`-1 Value	Isovalue	0.5
+-8 **50% Span projection**	Parts	[]
	Coordinate System	Laboratory
	Rotation Origin	[0.0, 0.0, 0.0] m,m,m
	Rotation Axis	[1.0, 0.0, 0.0] m,m,m
	Tangential Axis	[0.0, 1.0, 0.0] m,m,m
	Tags	[]
+-9 **70% Span**	Parts	[R37_SI]
	Scalar Field	Axisymmetric Complete Domain S Normalized
	Mode	ISOVALUE_SINGLE
	Tags	[]
`-1 Value	Isovalue	0.7
+-10 **90% Span**	Parts	[R37_SI]
	Scalar Field	Axisymmetric Complete Domain S Normalized
	Mode	ISOVALUE_SINGLE
	Tags	[]
`-1 Value	Isovalue	0.9
+-11 **90% Span - extrados**	Parts	[R37_SI: R37.Blade_Extrados]
	Scalar Field	Axisymmetric Complete Domain S Normalized
	Mode	ISOVALUE_SINGLE
	Tags	[]
`-1 Value	Isovalue	0.9
+-12 **90% Span - intrados**	Parts	[R37_SI: R37.Blade_Intrados]
	Scalar Field	Axisymmetric Complete Domain S Normalized
	Mode	ISOVALUE_SINGLE
	Tags	[]
`-1 Value	Isovalue	0.9
+-13 **90% Span projection**	Parts	[90% Span]
	Coordinate System	Laboratory
	Rotation Origin	[0.0, 0.0, 0.0] m,m,m
	Rotation Axis	[1.0, 0.0, 0.0] m,m,m
	Tangential Axis	[0.0, 1.0, 0.0] m,m,m

	Tags	[]
+-14 **Adimensional plane**	Parts	[R37_SI]
	Scalar Field	Axisymmetric Complete Domain M
	Mode	ISOVALUE_SINGLE
	Tags	[]
`-1 Value	Isovalue	0.070477 m
+-15 **Aux Asimensional plane**	Parts	[R37_SI]
	Scalar Field	Distance2Inlet
	Mode	ISOVALUE_SINGLE
	Tags	[]
`-1 Value	Isovalue	0.070477 m
+-16 **Line at Chord Distance 50%**	Parts	[R37_SI]
	Point 1	[0.2156987775950527, 5.85, -0.057774259852175956] m,radian,m
	Point 2	[0.2156987775950527, 6.08, -0.056523001213900435] m,radian,m
	Coordinate System	Laboratory->Cylindrical-Parametrization
	Resolution	20
	Tags	[]
+-17 **Longitudinal Isosurface 1**	Parts	[R37_SI]
	Scalar Field	Axisymmetric Complete Domain M Normalized
	Mode	ISOVALUE_SINGLE
	Tags	[]
`-1 Value	Isovalue	0.58
+-18 **Longitudinal Isosurface 2**	Parts	[R37_SI]
	Scalar Field	Axisymmetric Complete Domain M Normalized
	Mode	ISOVALUE_SINGLE
	Tags	[]
`-1 Value	Isovalue	0.65
+-19 **Longitudinal Isosurface Stat. 1**	Parts	[R37_SI]
	Scalar Field	Axisymmetric Complete Domain M Normalized
	Mode	ISOVALUE_SINGLE
	Tags	[]
`-1 Value	Isovalue	0.5
+-20 **Longitudinal Isosurface Stat. 1a**	Origin	[0.178, -0.02, -0.002] m,m,m
	Coordinate System	Laboratory
	Normal	[-0.08, 0.009, 1.0] m,m,m
	Parts	[R37_SI]
	Section Mode	SINGLE
	Displayed Index	-1
	Tags	[]
`-1 Single section	Offset	0.0 m
+-21 **Longitudinal Isosurface Stat. 3**	Parts	[R37_SI]
	Scalar Field	Axisymmetric Complete Domain M Normalized
	Mode	ISOVALUE_SINGLE
	Tags	[]
`-1 Value	Isovalue	0.678
+-22 **Meriodional Extrados**	Parts	[R37_SI]
	Scalar Field	Meridional Extrados
	Mode	ISOVALUE_SINGLE
	Tags	[]
`-1 Value	Isovalue	0.0 m
+-23 **Meriodional Intrados**	Parts	[R37_SI]
	Scalar Field	Meridional Intrados
	Mode	ISOVALUE_SINGLE
	Tags	[]
`-1 Value	Isovalue	0.0 m
+-24 **Point 50%**	Parts	[R37.Blade_Intrados]
	Point	[0.2156987775950527, 6.175960346552706, 0.0016971] m,radian,m
	Coordinate System	Laboratory->Cylindrical-Parametrization
	Follow Motion	false
	Highlight Input Coordinates	false
	Tags	[]
+-25 **Point at Chord Distance**	Parts	[R37_SI]
	Point	[0.2156987775950527, 6.0, -0.056523001213900435] m,radian,m
	Coordinate System	Laboratory->Cylindrical-Parametrization
	Follow Motion	false
	Highlight Input Coordinates	false
	Tags	[]
+-26 **Point at Intrados**	Parts	[R37_SI]
	Point	[0.2143279296017166, 1.551017056539166E-4, 0.014196519923516147] m,m,m
	Coordinate System	Laboratory
	Follow Motion	false
	Highlight Input Coordinates	false
	Tags	[]
+-27 **Point Inlet**	Parts	[R37_SI]
	Point	[0.2, -0.09, -0.127] m,m,m
	Coordinate System	Laboratory
	Follow Motion	false
	Highlight Input Coordinates	false
	Tags	[]
+-28 **Streamline 10%**	Parts	[R37_SI]
	Seed Type	PART
	Rotation Scale	1.0
	Vector Field	Relative Velocity
	Integration Solver	RK2

	Wall Treatment	ON
	Tags	[]
+-1 Source Seed	Seed Parts	[10% Span]
	On Ratio	5
	Randomize	false
	N Grid Points	[20, 20]
`-2 2nd Order Integrator	Initial Integration Step	0.5
	Maximum Propagation	0.5069332000000006
	Max Steps	2000
	Integration Direction	FORWARD
+-29 **Streamline 50%**	Parts	[R37_SI]
	Seed Type	PART
	Rotation Scale	1.0
	Vector Field	Relative Velocity
	Integration Solver	RK2
	Wall Treatment	ON
	Tags	[]
+-1 Source Seed	Seed Parts	[50% Span]
	On Ratio	5
	Randomize	false
	N Grid Points	[20, 20]
`-2 2nd Order Integrator	Initial Integration Step	0.5
	Maximum Propagation	0.5069332000000006
	Max Steps	2000
	Integration Direction	FORWARD
`-30 **Streamline 90%**	Parts	[R37_SI]
	Seed Type	PART
	Rotation Scale	1.0
	Vector Field	Relative Velocity
	Integration Solver	RK2
	Wall Treatment	ON
	Tags	[]
+-1 Source Seed	Seed Parts	[90% Span]
	On Ratio	5
	Randomize	false
	N Grid Points	[20, 20]
`-2 2nd Order Integrator	Initial Integration Step	0.5
	Maximum Propagation	0.5069332000000006
	Max Steps	2000
	Integration Direction	FORWARD
+-27 Summaries		
+-28 Monitors	Monitors	26
	Monitors To Print	[Continuity, X-momentum, Y-momentum, Z-momentum, Energy, Tke, Sdr, Intermittency, ReTheta_t, Mass Flow Outlet Monitor, Mass Flow Inlet Monitor, Pressure Outlet Monitor, Pressure Inlet Monitor, Torque Monitor, Pressure Inlet Monitor 2, Pressure Outlet Monitor 2, Corrected Mass Flow Inlet Monitor, Temp Inlet Rotating Monitor, Temp Outlet Rotating Monitor, Temp Outlet Monitor, Temp Inlet Monitor, Pressure Ratio Rotor Monitor, Efficiency Rotor Monitor, Probe Convergence Monitor]
	Output Direction	Horizontal
	Heading Print Frequency	10
+-1 **Corrected Mass Flow Inlet Monitor**	Report	[Corrected Mass Flow Inlet]
	Enabled	true
	Value Type	Total Value
	Trigger	Iteration
	Normalization Option	Off
	Maximum Plot Samples	5000
	Tags	[]
`-1 Iteration Frequency	Iteration Frequency	1
	Start Iteration	0
	Enable Stop	false
	Stop Iteration	0
+-2 **Efficiency Rotor Monitor**	Report	[Efficiency Rotor]
	Enabled	true
	Value Type	Total Value
	Trigger	Iteration
	Normalization Option	Off
	Maximum Plot Samples	5000
	Tags	[]
`-1 Iteration Frequency	Iteration Frequency	1
	Start Iteration	0
	Enable Stop	false
	Stop Iteration	0
+-3 **Iteration**	Maximum Plot Samples	5000
	Tags	[]
+-4 **Mass Flow Inlet Monitor**	Report	[Mass Flow Inlet]
	Enabled	true
	Value Type	Total Value
	Trigger	Iteration
	Normalization Option	Off

	Maximum Plot Samples	5000
	Tags	[]
`-1 Iteration Frequency	Iteration Frequency	1
	Start Iteration	0
	Enable Stop	false
	Stop Iteration	0
+-5 **Mass Flow Outlet Monitor**	Report	[Mass Flow Outlet]
	Enabled	true
	Value Type	Total Value
	Trigger	Iteration
	Normalization Option	Off
	Maximum Plot Samples	5000
	Tags	[]
`-1 Iteration Frequency	Iteration Frequency	1
	Start Iteration	0
	Enable Stop	false
	Stop Iteration	0
+-6 **Physical Time**	Maximum Plot Samples	5000
	Tags	[]
+-7 **Pressure Inlet Monitor**	Report	[Pressure Inlet]
	Enabled	true
	Value Type	Total Value
	Trigger	Iteration
	Normalization Option	Off
	Maximum Plot Samples	5000
	Tags	[]
`-1 Iteration Frequency	Iteration Frequency	1
	Start Iteration	0
	Enable Stop	false
	Stop Iteration	0
+-8 **Pressure Inlet Monitor 2**	Report	[Pressure Inlet]
	Enabled	true
	Value Type	Total Value
	Trigger	Iteration
	Normalization Option	Off
	Maximum Plot Samples	5000
	Tags	[]
`-1 Iteration Frequency	Iteration Frequency	1
	Start Iteration	0
	Enable Stop	false
	Stop Iteration	0
+-9 **Pressure Outlet Monitor**	Report	[Pressure Outlet]
	Enabled	true
	Value Type	Total Value
	Trigger	Iteration
	Normalization Option	Off
	Maximum Plot Samples	5000
	Tags	[]
`-1 Iteration Frequency	Iteration Frequency	1
	Start Iteration	0
	Enable Stop	false
	Stop Iteration	0
+-10 **Pressure Outlet Monitor 2**	Report	[Pressure Outlet]
	Enabled	true
	Value Type	Total Value
	Trigger	Iteration
	Normalization Option	Off
	Maximum Plot Samples	5000
	Tags	[]
`-1 Iteration Frequency	Iteration Frequency	1
	Start Iteration	0
	Enable Stop	false
	Stop Iteration	0
+-11 **Pressure Ratio Rotor Monitor**	Report	[Pressure Ratio Rotor]
	Enabled	true
	Value Type	Total Value
	Trigger	Iteration
	Normalization Option	Off
	Maximum Plot Samples	5000
	Tags	[]
`-1 Iteration Frequency	Iteration Frequency	1
	Start Iteration	0
	Enable Stop	false
	Stop Iteration	0
+-12 **Probe Convergence Monitor**	Report	[Probe Convergence]
	Enabled	true

	Value Type	Total Value
	Trigger	Iteration
	Normalization Option	Off
	Maximum Plot Samples	5000
	Tags	[]
`-1 Iteration Frequency	Iteration Frequency	1
	Start Iteration	0
	Enable Stop	false
	Stop Iteration	0
+-13 **Temp Inlet Monitor**	Report	[Temp Inlet]
	Enabled	true
	Value Type	Total Value
	Trigger	Iteration
	Normalization Option	Off
	Maximum Plot Samples	5000
	Tags	[]
`-1 Iteration Frequency	Iteration Frequency	1
	Start Iteration	0
	Enable Stop	false
	Stop Iteration	0
+-14 **Temp Inlet Rotating Monitor**	Report	[Temp Inlet Rotating]
	Enabled	true
	Value Type	Total Value
	Trigger	Iteration
	Normalization Option	Off
	Maximum Plot Samples	5000
	Tags	[]
`-1 Iteration Frequency	Iteration Frequency	1
	Start Iteration	0
	Enable Stop	false
	Stop Iteration	0
+-15 **Temp Outlet Monitor**	Report	[Temp Outlet]
	Enabled	true
	Value Type	Total Value
	Trigger	Iteration
	Normalization Option	Off
	Maximum Plot Samples	5000
	Tags	[]
`-1 Iteration Frequency	Iteration Frequency	1
	Start Iteration	0
	Enable Stop	false
	Stop Iteration	0
+-16 **Temp Outlet Rotating Monitor**	Report	[Temp Outlet Rotating]
	Enabled	true
	Value Type	Total Value
	Trigger	Iteration
	Normalization Option	Off
	Maximum Plot Samples	5000
	Tags	[]
`-1 Iteration Frequency	Iteration Frequency	1
	Start Iteration	0
	Enable Stop	false
	Stop Iteration	0
+-17 **Torque Monitor**	Report	[Torque]
	Enabled	true
	Value Type	Total Value
	Trigger	Iteration
	Normalization Option	Off
	Maximum Plot Samples	5000
	Tags	[]
`-1 Iteration Frequency	Iteration Frequency	1
	Start Iteration	0
	Enable Stop	false
	Stop Iteration	0
+-29 Reports	Reports	28
+-1 Pressure Loss Coefficient		
+-1 **Pressure Loss Coefficient Report**	Units	
	Definition	${Pressure Loss Coefficient}
	Periodicity	Non-periodic
	Delta Value	false
	Tags	[]
+-2 **Relative Pressure Inlet**	Units	Pa
	Field Function	Total Pressure in Rotating
	Parts	[R37_SI: R37.Inlet]
	Representation	Volume Mesh
	Smooth Values	false
	Weighting Function	<Select Function>

	Tags	[]
`-3 **Relative Pressure Outlet**	Units	Pa
	Field Function	Total Pressure in Rotating
	Parts	[R37_SI: R37.Outlet]
	Representation	Volume Mesh
	Smooth Values	false
	Weighting Function	<Select Function>
	Tags	[]
+-2 Probe		
+-1 **Density Point**	Units	kg/m^3
	Field Function	Density
	Collocated Field Functions	[]
	Parts	[Point at Chord Distance]
	Representation	Volume Mesh
	Smooth Values	false
	Tags	[]
+-2 **Dynamic Viscosity Point**	Units	Pa-s
	Field Function	Dynamic Viscosity
	Collocated Field Functions	[]
	Parts	[Point at Chord Distance]
	Representation	Volume Mesh
	Smooth Values	false
	Tags	[]
`-3 **Velocity Point**	Units	m/s
	Field Function	Relative Velocity: Magnitude
	Collocated Field Functions	[]
	Parts	[Point at Chord Distance]
	Representation	Volume Mesh
	Smooth Values	false
	Tags	[]
+-3 **Check Area Inlet-Outlet**	Units	m^2
	Field Function	Area: Magnitude
	Parts	[]
	Representation	Volume Mesh
	Smooth Values	false
	Tags	[]
+-4 **Corrected Mass Flow Inlet**	Units	
	Field Function	Corrected Mass Flow Inlet
	Parts	[R37_SI: R37.Inlet]
	Representation	Volume Mesh
	Smooth Values	false
	Weighting Function	<Select Function>
	Tags	[]
+-5 **Density Adimensional**	Units	kg/m^3
	Field Function	Density
	Parts	[Adimensional plane]
	Representation	Volume Mesh
	Smooth Values	false
	Weighting Function	<Select Function>
	Tags	[]
+-6 **Efficiency Rotor**	Units	
	Definition	${Eta_rotor}
	Periodicity	Non-periodic
	Delta Value	false
	Tags	[]
+-7 **Flow Angle Plane**	Units	
	Field Function	Rotational Flow Angle
	Parts	[Adimensional plane]
	Representation	Volume Mesh
	Smooth Values	false
	Weighting Function	<Select Function>
	Tags	[]
+-8 **Flow Angle Point**	Units	
	Field Function	Rotational Flow Angle
	Collocated Field Functions	[]
	Parts	[Point at Chord Distance]
	Representation	Volume Mesh
	Smooth Values	false
	Tags	[]
+-9 **Mass Flow Inlet**	Units	kg/s
	Parts	[R37_SI: R37.Inlet]
	Representation	Volume Mesh
	Smooth Values	false
	Account for Idealization	false
	Tags	[]
+-10 **Mass Flow Inlet (360)**	Units	
	Definition	${Mass Flow inlet per 360}
	Periodicity	Non-periodic
	Delta Value	false
	Tags	[]
+-11 **Mass Flow Outlet**	Units	kg/s
	Parts	[R37_SI: R37.Outlet]
	Representation	Volume Mesh
	Smooth Values	false
	Account for Idealization	false
	Tags	[]
+-12 **Maximum 1**	Units	m
	Field Function	Position[Z]

	Collocated Field Functions	[]
	Parts	[R37_SI: R37.Blade_Extrados, R37_SI: R37.Blade_Intrados]
	Representation	Volume Mesh
	Smooth Values	false
	Tags	[]
+-13 **Minimum 1**	Units	m
	Field Function	Position[Z]
	Collocated Field Functions	[]
	Parts	[R37_SI: R37.Blade_Extrados, R37_SI: R37.Blade_Intrados]
	Representation	Volume Mesh
	Smooth Values	false
	Tags	[]
+-14 **Pressure Inlet**	Units	Pa
	Field Function	Absolute Total Pressure
	Parts	[R37_SI: R37.Inlet]
	Representation	Volume Mesh
	Smooth Values	false
	Weighting Function	<Select Function>
	Tags	[]
+-15 **Pressure Outlet**	Units	Pa
	Field Function	Absolute Total Pressure
	Parts	[R37_SI: R37.Outlet]
	Representation	Volume Mesh
	Smooth Values	false
	Weighting Function	<Select Function>
	Tags	[]
+-16 **Pressure Ratio Rotor**	Units	
	Definition	${Pressure Outlet}/${Pressure Inlet}
	Periodicity	Non-periodic
	Delta Value	false
	Tags	[]
+-17 **Probe Convergence**	Units	
	Field Function	Pressure Coefficient
	Collocated Field Functions	[]
	Parts	[Point at Intrados]
	Representation	Volume Mesh
	Smooth Values	false
	Tags	[]
+-18 **Reynolds Number**	Units	
	Field Function	Reynolds Number
	Parts	[Adimensional plane]
	Representation	Volume Mesh
	Smooth Values	false
	Weighting Function	<Select Function>
	Tags	[]
+-19 **Temp Inlet**	Units	K
	Field Function	Total Temperature
	Parts	[R37_SI: R37.Inlet]
	Representation	Volume Mesh
	Smooth Values	false
	Weighting Function	<Select Function>
	Tags	[]
+-20 **Temp Inlet Rotating**	Units	K
	Field Function	Total Temperature in Rotating
	Parts	[R37_SI: R37.Inlet]
	Representation	Volume Mesh
	Smooth Values	false
	Weighting Function	<Select Function>
	Tags	[]
+-21 **Temp Outlet**	Units	K
	Field Function	Total Temperature
	Parts	[R37_SI: R37.Outlet]
	Representation	Volume Mesh
	Smooth Values	false
	Weighting Function	<Select Function>
	Tags	[]
+-22 **Temp Outlet Rotating**	Units	K
	Field Function	Total Temperature in Rotating
	Parts	[R37_SI: R37.Outlet]
	Representation	Volume Mesh
	Smooth Values	false
	Weighting Function	<Select Function>
	Tags	[]
+-23 **Torque**	Units	N-m
	Coordinate System	Laboratory
	Force Option	Pressure + Shear
	Reference Pressure	0.0 Pa
	Axis	[0.0, 0.0, 1.0]
	Number of Bands	0
	Axis Origin	[0.0, 0.0, 0.0] m
	Parts	[R37_SI: R37.Blade_Extrados, R37_SI: R37.Blade_Intrados]
	Representation	Volume Mesh
	Smooth Values	false
	Account for Idealization	false

| |	Tags	[]
| `-24 **Velocity Adimensional**	Units	m/s
|	Field Function	Velocity in Rotating: Magnitude
|	Parts	[Adimensional plane]
|	Representation	Volume Mesh
|	Smooth Values	false
|	Weighting Function	<Select Function>
|	Tags	[]
+-30 Solvers	Cache Solver Settings	true
| +-1 Steady		
| | `-1 Stopping Criteria	Verbose	false
| +-2 Partitioning	Solver Frozen	false
| |	Partitioning Method	Per-Continuum
| +-3 Wall Distance	Solver Frozen	false
| |	Verbosity	0
| |	Minimum Tree Size Threshold	500000
| +-4 Coupled Implicit	Freeze Flow	false
| | |	Pressure Reference Location	Automatic Selection
| | |	Reconstruction Frozen	false
| | |	Reconstruction Zeroed	false
| | |	Temporary Storage Retained	false
| | |	CFL Control Method	Linear Ramp
| | |	Explicit Relaxation Method	Constant
| | |	Enhanced Dissipation	false
| | |	Enhanced Dissipation Start Transition	1
| | |	Enhanced Dissipation End Transition	100
| | |	Unsteady Optimization Tolerance	1.0
| | |	Velocity Correction Limiting	On
| | +-1 Linear Ramp CFL	Current CFL	5.0
| | |	Target CFL	5.0
| | |	Start Iteration	1
| | |	End Iteration	50
| | |	Initial CFL	0.1
| | +-2 Constant Relaxation	Explicit Relaxation	0.3
| | +-3 AMG Linear Solver	Max Cycles	30
| | | |	Verbosity	NONE
| | | |	Enable Direct Solver	false
| | | |	Maximum Direct Solver Equations	32
| | | |	Convergence Tolerance	0.1
| | | |	Epsilon	0.0
| | | |	Cycle Type	V Cycle
| | | |	Group Size Control	Auto
| | | |	Group Size	4
| | | |	Relaxation Scheme	Gauss-Seidel
| | | |	Acceleration Method	Bi Conjugate Gradient Stabilized
| | | |	Scaling	Disabled
| | | `-1 V Cycle	Pre-Sweeps	1
| | |	Post-Sweeps	2
| | |	Max Levels	50
| | +-4 Expert Initialization	Method	None
| | `-5 Convergence Accelerators	Convergence Accelerators	None
| +-5 K-Omega Turbulence	Solver Frozen	false
| | |	Reconstruction Frozen	false
| | |	Reconstruction Zeroed	false
| | |	Temporary Storage Retained	false
| | |	Under-Relaxation Factor	0.8
| | |	Boundary Layer Initialization	false
| | +-1 Under-Relaxation Factor Ramp	Ramp Method	Linear Ramp
| | | `-1 Linear Ramp	Start Iteration	1
| | |	End Iteration	50
| | |	Initial Value	0.08
| | `-2 AMG Linear Solver	Max Cycles	30

	Verbosity	NONE
	Enable Direct Solver	false
	Maximum Direct Solver Equations	32
	Convergence Tolerance	0.1
	Epsilon	0.0
	Cycle Type	Flex Cycle
	Group Size Control	Auto
	Group Size	4
	Relaxation Scheme	Gauss-Seidel
	Acceleration Method	None
	Scaling	Disabled
`-1 Flex Cycle	Restriction Tolerance	0.9
	Prolongation Tolerance	0.5
	Sweeps	1
+-6 K-Omega Turbulent Viscosity	Solver Frozen	false
	Under-Relaxation Factor	1.0
	Maximum Ratio	100000.0
`-7 GammaReTheta Transition	Solver Frozen	false
	Reconstruction Frozen	false
	Reconstruction Zeroed	false
	Temporary Storage Retained	false
	Under-Relaxation Factor	0.8
+-1 Under-Relaxation Factor Ramp	Ramp Method	No Ramp
`-2 AMG Linear Solver	Max Cycles	30
	Verbosity	NONE
	Enable Direct Solver	false
	Maximum Direct Solver Equations	32
	Convergence Tolerance	0.1
	Epsilon	0.0
	Cycle Type	Flex Cycle
	Group Size Control	Auto
	Group Size	4
	Relaxation Scheme	Gauss-Seidel
	Acceleration Method	None
	Scaling	Disabled
`-1 Flex Cycle	Restriction Tolerance	0.9
	Prolongation Tolerance	0.5
	Sweeps	1
+-31 Stopping Criteria	Verbose	false
+-1 **Maximum Inner Iterations**	Enabled	true
	Maximum Inner Iterations	5
	Logical Rule	Or
	Criterion Satisfied	false
	Tags	[]
+-2 **Maximum Physical Time**	Enabled	true
	Maximum Physical Time	1.0 s
	Logical Rule	Or
	Criterion Satisfied	false
	Tags	[]
+-3 **Maximum Steps**	Enabled	true
	Maximum Steps	280000
	Logical Rule	Or
	Criterion Satisfied	false
	Tags	[]
`-4 **Stop File**	Enabled	true
	Stop Inner Iterations	true
	Path	ABORT
	Logical Rule	Or
	Criterion Satisfied	false
	Tags	[]
+-32 Solution Histories		
+-33 Solution Views		
`-1 **Current Solution**	Iteration	189500
	Time Step	0
	Solution Time	0.0
	Tags	[]
+-34 Layout Views		

+-35 Automation

+-1 Parameters

+-1 **Chord**	Type	SCALAR
	Value	0.055485 m
	Tags	[]
+-2 **Inlet_massflow**	Type	SCALAR
	Value	0.84
	Tags	[]
+-3 **Inlet_temp**	Type	SCALAR
	Value	288.15 K
	Tags	[]
+-4 **Mesh_basesize**	Type	SCALAR
	Value	0.0018 m
	Tags	[]
+-5 **Mesh_minsurface**	Type	SCALAR
	Value	6.0E-5
	Tags	[]
+-6 **Mesh_numprismlayer**	Type	SCALAR
	Value	13.0
	Tags	[]
+-7 **Mesh_prismlaystreching**	Type	SCALAR
	Value	1.15
	Tags	[]
+-8 **Mesh_prismlaythick**	Type	SCALAR
	Value	7.2E-4 m
	Tags	[]
+-9 **Mesh_surfGrowRate**	Type	SCALAR
	Value	1.35
	Tags	[]
+-10 **Mesh_targetsurface**	Type	SCALAR
	Value	0.0012
	Tags	[]
+-11 **Mesh_volGrowRate**	Type	SCALAR
	Value	1.15
	Tags	[]
+-12 **Outlet_press**	Type	SCALAR
	Value	210600.0 Pa
	Tags	[]
+-13 **Outlet_temp**	Type	SCALAR
	Value	300.0 K
	Tags	[]
`-14 **w (rad/s)**	Type	SCALAR
	Value	-1800.0
	Tags	[]

+-2 Field Functions

+-1 Differences

+-1 **Diff in RM 10-4**	Function Name	Diff in RM 100-4_2
	Inverse Distance Weight	false
	Value Type	Scalar
	Assembly Code	(- ${MappedVertexRelative Mach Number p10} ${MappedVertexRelative Mach Number p4})
	Definition	${MappedVertexRelative Mach Number p10}-${MappedVertexRelative Mach Number p4}
	Ignore Boundary Values	false
	Tags	[]
+-2 **Diff in RM 40-4**	Function Name	Diff in RM 100-4_4
	Inverse Distance Weight	false
	Value Type	Scalar
	Assembly Code	(- ${MappedVertexRelative Mach Number p40} ${MappedVertexRelative Mach Number p4})
	Definition	${MappedVertexRelative Mach Number p40}-${MappedVertexRelative Mach Number p4}
	Ignore Boundary Values	false
	Tags	[]
+-3 **Diff in RM 40-10**	Function Name	Diff in RM 100-4_5
	Inverse Distance Weight	false
	Value Type	Scalar
	Assembly Code	(- ${MappedVertexRelative Mach Number p40} ${MappedVertexRelative Mach Number p10})
	Definition	${MappedVertexRelative Mach Number p40}-${MappedVertexRelative Mach Number p10}
	Ignore Boundary Values	false
	Tags	[]
+-4 **Diff in RM 100-4**	Function Name	Diff in RM 100-4
	Inverse Distance Weight	false
	Value Type	Scalar
	Assembly Code	(- ${RelativeMachNumber} ${MappedVertexRelative Mach Number p4})
	Definition	${RelativeMachNumber}-${MappedVertexRelative Mach Number p4}
	Ignore Boundary Values	false
	Tags	[]
+-5 **Diff in RM 100-10**	Function Name	Diff in RM 100-10
	Inverse Distance Weight	false
	Value Type	Scalar
	Assembly Code	(- ${RelativeMachNumber} ${MappedVertexRelative Mach Number p10})
	Definition	${RelativeMachNumber}-${MappedVertexRelative Mach Number p10}
	Ignore Boundary Values	false
	Tags	[]
`-6 **Diff in RM 100-40**	Function Name	Diff in RM 100-4_3
	Inverse Distance Weight	false
	Value Type	Scalar
	Assembly Code	(- ${RelativeMachNumber} ${MappedVertexRelative Mach Number p40})
	Definition	${RelativeMachNumber}-${MappedVertexRelative Mach Number p40}

- Ignore Boundary Values: false
- Tags: []

+-2 Friction Coefficients

+-1 **Friction Coefficient 10%**

- Function Name: Friction Coefficient 10%
- Inverse Distance Weight: false
- Value Type: Scalar
- Assembly Code: (/ $${WallShearStress}("Laboratory.Isospan 10%")[1] (* (* 0.5 ${DensityAdimensionalReport}) ${VelocityAdimensionalReport}))
- Definition: $$WallShearStress(@CoordinateSystem("Laboratory.Isospan 10%"))[1]/(0.5*${DensityAdimensionalReport}*${VelocityAdimensionalReport})
- Ignore Boundary Values: false
- Tags: []

+-2 **Friction Coefficient 50%**

- Function Name: Friction Coefficient 50%
- Inverse Distance Weight: false
- Value Type: Scalar
- Assembly Code: (/ $${WallShearStress}("Laboratory.Isospan 50%")[1] (* (* 0.5 ${DensityAdimensionalReport}) ${VelocityAdimensionalReport}))
- Definition: $$WallShearStress(@CoordinateSystem("Laboratory.Isospan 50%"))[1]/(0.5*${DensityAdimensionalReport}*${VelocityAdimensionalReport})
- Ignore Boundary Values: false
- Tags: []

`-3 **Friction Coefficient 90%**

- Function Name: Friction Coefficient 90%
- Inverse Distance Weight: false
- Value Type: Scalar
- Assembly Code: (/ $${WallShearStress}("Laboratory.Isospan 90%")[1] (* (* 0.5 ${DensityAdimensionalReport}) ${VelocityAdimensionalReport}))
- Definition: $$WallShearStress(@CoordinateSystem("Laboratory.Isospan 90%"))[1]/(0.5*${DensityAdimensionalReport}*${VelocityAdimensionalReport})
- Ignore Boundary Values: false
- Tags: []

+-3 Surface Distance

+-1 **Distance2AuxExtrados**

- Function Name: Distance2AuxExtrados
- Inverse Distance Weight: false
- Value Type: Scalar
- Assembly Code: distanceToSurface(@PartSurface("Extrados|Blade_Extrados"))
- Definition: distanceToSurface(@PartSurface("Extrados|Blade_Extrados"))
- Ignore Boundary Values: false
- Tags: []

+-2 **Distance2AuxIntrados**

- Function Name: Distance2AuxIntrados
- Inverse Distance Weight: false
- Value Type: Scalar
- Assembly Code: distanceToSurface(@PartSurface("Intrados|Blade_Intrados"))
- Definition: distanceToSurface(@PartSurface("Intrados|Blade_Intrados"))
- Ignore Boundary Values: false
- Tags: []

+-3 **Distance2Extrados**

- Function Name: Distance2Extrados
- Inverse Distance Weight: false
- Value Type: Scalar
- Assembly Code: distanceToSurface(@PartSurface("R37|Blade_Extrados"))
- Definition: distanceToSurface(@PartSurface("R37|Blade_Extrados"))
- Ignore Boundary Values: false
- Tags: []

+-4 **Distance2Inlet**

- Function Name: Distance2Extrados_2
- Inverse Distance Weight: false
- Value Type: Scalar
- Assembly Code: distanceToSurface(@PartSurface("R37|Inlet"))
- Definition: distanceToSurface(@PartSurface("R37|Inlet"))
- Ignore Boundary Values: false
- Tags: []

+-5 **Distance2Intrados**

- Function Name: Distance2Intrados
- Inverse Distance Weight: false
- Value Type: Scalar
- Assembly Code: distanceToSurface(@PartSurface("R37|Blade_Intrados"))
- Definition: distanceToSurface(@PartSurface("R37|Blade_Intrados"))
- Ignore Boundary Values: false
- Tags: []

+-6 **Meridional Extrados**

- Function Name: Meridional Extrados
- Inverse Distance Weight: false
- Value Type: Scalar
- Assembly Code: (- ${Distance2Extrados} ${Distance2AuxIntrados})
- Definition: ${Distance2Extrados}-${Distance2AuxIntrados}
- Ignore Boundary Values: false
- Tags: []

`-7 **Meridional Intrados**

- Function Name: Meridional Intrados
- Inverse Distance Weight: false
- Value Type: Scalar
- Assembly Code: (- ${Distance2Intrados} ${Distance2AuxExtrados})
- Definition: ${Distance2Intrados}-${Distance2AuxExtrados}

- Ignore Boundary Values: false
- Tags: []

+-4 **Corrected Mass Flow Inlet**

- Function Name: Corrected Mass Flow Inlet
- Inverse Distance Weight: false
- Value Type: Scalar
- Assembly Code: (* (* (/ (- ${Mass Flow Inlet}) (/ ${Pressure Inlet} 101325)) (/ 1 (pow (/ 273.15 ${TempInletReport}) 0.5))) 36)
- Definition: -${Mass Flow Inlet}/(${Pressure Inlet}/101325)*(1/pow((273.15/${TempInletReport}),0.5))*36
- Ignore Boundary Values: false
- Tags: []

+-5 **Cylindrical Axial Velocity**

- Function Name: Cylindrical Axial Velocity
- Inverse Distance Weight: false
- Value Type: Scalar
- Assembly Code: $${Velocity}("Cylindrical-Parametrization")[2]
- Definition: $$Velocity(@CoordinateSystem("Cylindrical-Parametrization"))[2]
- Ignore Boundary Values: false
- Tags: []

+-6 **Cylindrical Tangential Velocity**

- Function Name: Cylindrical Tangential Velocity
- Inverse Distance Weight: false
- Value Type: Scalar
- Assembly Code: $${RelativeVelocity}("Cylindrical-Parametrization")[1]
- Definition: $$RelativeVelocity(@CoordinateSystem("Cylindrical-Parametrization"))[1]
- Ignore Boundary Values: false
- Tags: []

+-7 **Distance2Hub**

- Function Name: Distance2Hub
- Inverse Distance Weight: false
- Value Type: Scalar
- Assembly Code: distanceToSurface(@PartSurface("R37|Hub"))
- Definition: distanceToSurface(@PartSurface("R37|Hub"))
- Ignore Boundary Values: false
- Tags: []

+-8 **Distance2Shroud**

- Function Name: Distance2Shroud
- Inverse Distance Weight: false
- Value Type: Scalar
- Assembly Code: distanceToSurface(@PartSurface("R37|Shroud"))
- Definition: distanceToSurface(@PartSurface("R37|Shroud"))
- Ignore Boundary Values: false
- Tags: []

+-9 **Eta_rotor**

- Function Name: Eta_rotor
- Inverse Distance Weight: false
- Value Type: Scalar
- Assembly Code: (/ (+ -1 (pow (/ ${Pressure Outlet} ${Pressure Inlet}) 0.285714)) (+ -1 (/ ${Temp Outlet} ${Temp Inlet})))
- Definition: (-1 + pow((${Pressure Outlet}/${Pressure Inlet}),0.2857143))/(-1 + (${Temp Outlet}/${Temp Inlet}))
- Ignore Boundary Values: false
- Tags: []

+-10 **Field Function Mesh Refinement**

- Function Name: Field Function Mesh Refinement
- Inverse Distance Weight: false
- Value Type: Scalar
- Assembly Code: (if (<= ${RelativeMachNumber} 0.7) (/ ${Mesh_basesize} 4) ${Mesh_basesize})
- Definition: ${RelativeMachNumber} <= 0.7 ? ${Mesh_basesize}/4 : ${Mesh_basesize}
- Ignore Boundary Values: false
- Tags: []

+-11 **Field Function Mesh Refinement Complete**

- Function Name: Field Function Mesh Refinement Complete
- Inverse Distance Weight: false
- Value Type: Scalar
- Assembly Code: (if (> (* (mag grad ${MachNumber}) ${AdaptationCellSize}) 0.25) (/ ${Mesh_basesize} 4) (if (<= ${RelativeMachNumber} 0.7) (/ ${Mesh_basesize} 4) ${Mesh_basesize}))
- Definition: mag(grad(${MachNumber}))*(${AdaptationCellSize}) > 0.25 ? ${Mesh_basesize}/4 : ${RelativeMachNumber} <= 0.7 ? ${Mesh_basesize}/4 : ${Mesh_basesize}
- Ignore Boundary Values: false
- Tags: []

+-12 **Mass Flow inlet per 360**

- Function Name: Mass Flow inlet per 360
- Inverse Distance Weight: false
- Value Type: Scalar
- Assembly Code: (* -36 ${MassFlowInletReport})
- Definition: -36*${MassFlowInletReport}
- Ignore Boundary Values: false
- Tags: []

+-13 **Pressure_10**

- Function Name: Pressure_10
- Inverse Distance Weight: false
- Value Type: Scalar
- Assembly Code: (/ ${StaticPressure} 10)
- Definition: ${StaticPressure}/10
- Ignore Boundary Values: false
- Tags: []

| | +-14 **Pressure Loss Coefficient**	Function Name	Pressure Loss Coefficient
| | |	Inverse Distance Weight	false
| | |	Value Type	Scalar
| | |	Assembly Code	(/ (- ${RelativePressureInletReport} ${RelativePressureOutletReport}) (- ${RelativePressureInletReport} ${PressureInletReport}))
| | |	Definition	(${RelativePressureInletReport}-${RelativePressureOutletReport})/(${RelativePressureInletReport}-${PressureInletReport})
| | |	Ignore Boundary Values	false
| | |	Tags	[]
| | +-15 **Reynolds Number**	Function Name	Reynolds Number
| | |	Inverse Distance Weight	false
| | |	Value Type	Scalar
| | |	Assembly Code	(/ (* (* ${Density} ${Velocity Adimensional}) ${Chord}) ${DynamicViscosity})
| | |	Definition	${Density}*${Velocity Adimensional}*${Chord}/${DynamicViscosity}
| | |	Ignore Boundary Values	false
| | |	Tags	[]
| | +-16 **Rotational Flow Angle**	Function Name	Rotational Flow Angle
| | |	Inverse Distance Weight	false
| | |	Value Type	Scalar
| | |	Assembly Code	(/ (* (atan (/ ${Cylindrical Tangential Velocity} ${Cylindrical Axial Velocity})) 180) 3.14159)
| | |	Definition	atan(${Cylindrical Tangential Velocity}/${Cylindrical Axial Velocity})*180/3.14159265359
| | |	Ignore Boundary Values	false
| | |	Tags	[]
| | +-17 **Span Percentage**	Function Name	Span Percentage
| | |	Inverse Distance Weight	false
| | |	Value Type	Scalar
| | |	Assembly Code	(/ (* 100 ${Distance2Hub}) (+ ${Distance2Hub} ${Distance2Shroud}))
| | |	Definition	100*${Distance2Hub}/(${Distance2Hub}+${Distance2Shroud})
| | |	Ignore Boundary Values	false
| | |	Tags	[]
| | +-18 **TargetMassFlow**	Function Name	TargetMassFlow
| | |	Inverse Distance Weight	false
| | |	Value Type	Scalar
| | |	Assembly Code	(/ (* 13 (/ ${Pressure Inlet} 101325)) (/ 1 (pow (/ 273.15 ${TempInletRotatingReport}) 0.5)))
| | |	Definition	13*(${Pressure Inlet}/101325)/(1/pow((273.15/${TempInletRotatingReport}),0.5))
| | |	Ignore Boundary Values	false
| | |	Tags	[]
| +-3 Simulation Operations	Selected	[]
| +-4 Filters		
| +-5 Tags		
| +-6 Stages	Active Stage	[]
| +-7 Update Events	Event Count	0
| |	Event Names	
| `-8 Time Scales		

Solution

Accumulated CPU Time over all processes (s)	7355467.583000539
Elapsed Time (s)	573800.0872746183
Iterations	189500